POLITECNICO DI TORINO

Master of Science in
Mathematical Engineering

Master's Thesis

Probing Transport via Modulated Electron Cyclotron Deposition in Gyrokinetic Turbulence Simulations

Academic Supervisor
Prof. Fabio Subba
External Supervisor
Dr. M.J. Pueschel

Candidate
Luca Biscu

Academic Year 2024-2025

Alla mia famiglia

This research has been carried out at the Dutch Institute for Fundamental Energy Research (DIFFER) under the supervision of Dr. M. J. Pueschel, head of the Plasma Microturbulence Group, and in collaboration with the Energy Systems and Control Group, led by Dr. Matthijs van Berkel.
The project has been supported by the Fusenet Association and the EUROfusion Consortium under the Euratom research and training programme. The views and opinions expressed do not necessarily reflect those of the European Union or the European Commission.

Abstract

As magnetic-confinement nuclear fusion research advances toward reactor-stage operation, dynamic control of plasma behaviour has become an urgent topic. In this context, heat transport models that are both accurate and computationally efficient will be essential for designing control strategies in future fusion devices. In magnetically confined plasmas, several mechanisms contribute to radial heat transport, but turbulence driven by microinstabilities — such as trapped-electron modes (TEM), ion-temperature-gradient (ITG) modes, and electron-temperature-gradient (ETG) modes — plays the dominant role. Because the underlying physics is highly complex, reduced advection–diffusion (AD) models with effective transport coefficients are widely employed, often calibrated against experiments. However, these closures rely on strong assumptions (e.g., linearity, quasi-stationarity, and locality) that may, under certain conditions, be significantly violated by the intrinsically nonlinear and nonlocal nature of turbulent transport. This work investigates heat transport in a temperature-gradient–driven TEM regime and examines under which conditions an AD closure ceases to be valid. We perform high-fidelity gyrokinetic simulations using a new Electron Cyclotron Resonance Heating (ECRH) deposition module for the Gyrokinetic Electromagnetic Numerical Experiment (GENE) code. The power deposition is modulated over time scales comparable to or longer than characteristic turbulence time scales, and the resulting radial temperature response is analysed in the frequency domain to better understand its interaction with turbulence. We then employ a linear heat transport model to estimate effective diffusion and advection coefficients, and to assess the limits of their validity. The results show that decreasing the modulation frequency increases the response amplitude and broadens the spatial window of high coherence between the temperature signal and the ECRH drive, which is conducive to the applicability of AD models. Yet the spatial asymmetry of the frequency response function reveals limitations of advection–diffusion closures at these scales, and the inferred transport coefficients remain sensitive to the deposition frequency. Moreover, reducing the ECRH modulation amplitude to mitigate nonlinear effects is constrained by lower signal-to-noise ratios, requiring a balance between weak perturbation and measurable response. Overall, this study combines perturbative transport estimation with gyrokinetic turbulence modelling, establishing a methodological framework for more precise inference of heat-transport coefficients and paving the way for improved modelling and control strategies in fusion plasmas.

Acknowledgements

I would like to express my deepest gratitude to all those who supported me throughout this work. I owe a special thanks to my supervisors, MJ and Prof. Subba, whose guidance, thoughtful insights, and steady encouragement have shaped every stage of this project. I am particularly thankful to MJ, whose expertise, patience, and exceptional dedication have guided me far beyond what I could have hoped for; his support has been truly invaluable. Their generosity with their time and their willingness to discuss even the smallest technical detail have made this journey both inspiring and deeply formative.

My gratitude also goes to Dr. Matthijs van Berkel for his support, constructive feedback, and many helpful discussions throughout this project.

I am especially thankful to Petch, Max, Martijn, Leon, Sjoerd, Miko and Jaime for their scientific support and many insightful discussions. My sincere thanks also go to all members of the Plasma Microturbulence Group and the Energy Systems and Control Group, whose availability, friendly atmosphere, and everyday help have made this work genuinely enjoyable.

A special thanks goes to Tim, Ben, Niel, Daan, Jazine, Jakob, Alexander, Loek, Sammie, and all the wonderful people from the Gezellig Flex Office™, whose company, coffee breaks, borrels, and everyday conversations made life at DIFFER much lighter and more enjoyable (and I am also grateful to the many fantastic people in the other flex office).

Ringrazio di cuore anche il Dr. Casu, Uto, Andrea, Nicola e Lorenzo per le fantastiche serate trascorse insieme e per avermi fatto sentire a casa fin dal primo momento in cui sono arrivato qui. Un grazie sincero va anche a tutti gli amici di Torino, per la vicinanza, il sostegno e i momenti condivisi che hanno reso questi anni indimenticabili. E grazie, con particolare affetto, agli amici di sempre, quelli con cui sono cresciuto e che continuano a far parte della mia vita nonostante la distanza.

Contents

List of Figures

Quod natura munimento inviderat,
industria adiecit.

["Ciò che la natura aveva negato, l'ingegno lo aggiunse" – epigrafe del Pozzo di San Patrizio, Orvieto, 1537]

Chapter 1

Introduction: Magnetic Confinement Nuclear Fusion

The continuous growth of the global population, together with the rapid expansion of industrial and digital infrastructures, is driving an unprecedented increase in the world's energy demand. As global electrification deepens and new sectors—such as large-scale data processing — become increasingly energy-demanding, the need for clean, stable, and high-density power sources will only intensify. At the same time, the climate crisis, evidenced by the rising frequency and severity of extreme weather events, has made it clear that the current energy system—still heavily dependent on fossil fuels — is not viable in the long term. A transition toward an energy mix based on net-zero emission technologies is therefore essential to mitigate global warming and ensure environmental sustainability [1]. Within this context, nuclear fusion occupies a distinctive position: it promises an abundant, dispatchable, and intrinsically low–carbon energy source, with fuel reserves that are effectively inexhaustible on human time scales.

Although fusion energy may not arrive in time to meet the near-term decarbonization targets, which can in principle be already achieved through a combination of current nuclear fission technology and renewable energy sources [2], it is expected to play a central role in the long-term energy landscape. By providing a virtually limitless source of baseload power, fusion stands as a cornerstone technology for sustaining future generations in an increasingly energy-demanding world.

Nuclear fusion is the process that powers the stars. In its simplest form, it occurs when two light nuclei collide with sufficient kinetic energy to overcome their mutual Coulomb repulsion and approach to within a range where the strong nuclear force becomes attractive and binding. The resulting fusion product is a heavier nucleus and, in general, one or more energetic particles that carry away the released energy. The energy density associated with these reactions is extremely large when compared to chemical processes: the specific energy available from typical fusion reactions exceeds that of fossil fuels by several orders of magnitude. Combined with negligible direct greenhouse gas emissions, these properties make fusion an attractive long–term option in the portfolio of future energy technologies.

On astrophysical scales, gravitational confinement leads to extremely high density

values allowing stars to sustain fusion over billions of years. On Earth, by contrast, one must engineer alternative mechanisms to keep a plasma at fusion–relevant temperatures and densities for sufficiently long times. Two broad classes of confinement concepts have emerged: inertial confinement fusion, in which a target is compressed and heated on very short time scales, and magnetic confinement fusion (MCF), in which strong magnetic fields are used to confine a dilute plasma over much longer times. The present work is situated within the MCF approach.

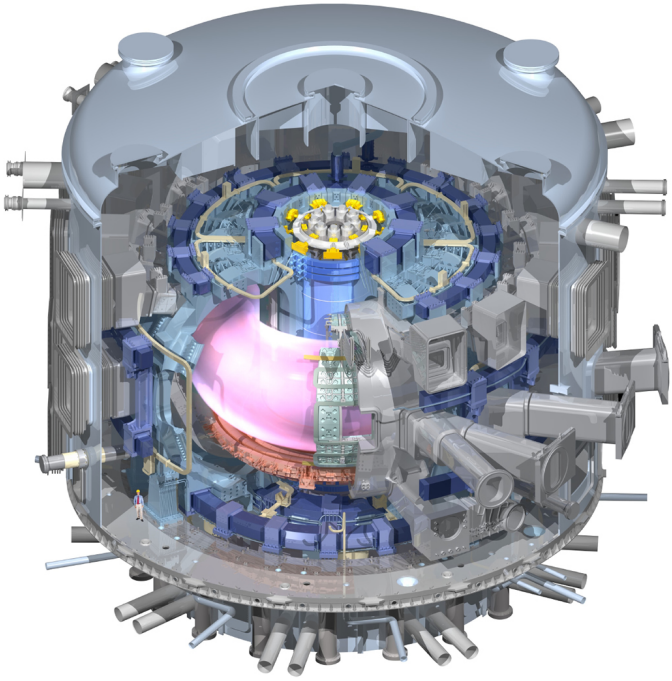

Figure 1.1: Sectional view of ITER [3].

The deuterium–tritium reaction and fusion conditions

From the many possible fusion reactions, the deuterium–tritium (D–T) reaction,

$$\mathrm{D} + \mathrm{T} \rightarrow \alpha(3.5\ \mathrm{MeV}) + n(14.1\ \mathrm{MeV})\,,$$

is considered the most favourable for energy production applications [4]. It features a relatively large reaction cross–section and yields a total energy release of 17.6 MeV, carried by an α particle and a neutron. The α particles can, in principle, transfer part of their energy back to the plasma and thus contribute to self–heating, while the neutrons escape and may be used to breed tritium and generate thermal power in an external blanket.

To achieve a net energy gain, not only must the plasma be heated to high temperatures, it must also be confined at sufficient density for a sufficiently long energy confinement time. These requirements are commonly summarized in the Lawson criterion [5]. In its simplest

form for a homogeneous plasma, this criterion can be expressed in terms of the so–called triple product $nT\tau_E$, where n is the particle density, T the temperature, and τ_E the energy confinement time. For a D–T plasma, ignition requires that

$$nT\tau_E \geq \frac{12\,T^2}{E_f\langle\sigma v\rangle} \simeq 3 \times 10^{21}\ \mathrm{keV\,s\,m^{-3}}, \tag{1.1}$$

where n is the plasma number density, T is the temperature (expressed in kiloelectronvolts), and τ_E is the energy confinement time, i.e. the characteristic time over which the plasma loses its internal energy to the surroundings. The term E_f denotes the energy released per fusion reaction, while $\langle\sigma v\rangle$ is the reaction rate. This expression defines the minimum value of the triple product required to achieve a self–sustained fusion burn. For the deuterium–tritium reaction, the right–hand side of Eq. (1.1) reaches its minimum at temperatures around 10–20 keV. The choice of the D–T fuel is precisely motivated by the relatively low value of this threshold compared to other candidate reactions. In practice, the Lawson criterion emphasizes that improvements in confinement time, and thus in the control of energy and particle transport, are at least as important as the attainment of high plasma temperatures.

Magnetic confinement and heat transport in fusion plasmas

Magnetic confinement fusion seeks to satisfy the Lawson criterion by placing a high temperature, quasi–neutral plasma in a carefully designed magnetic field configuration. The two main magnetic confinement concepts are tokamaks and stellarators. In tokamaks, a toroidal magnetic field generated by external toroidal-field coils is supplemented by a large plasma current that produces a poloidal field, thereby forming nested magnetic flux surfaces. In stellarators, the required poloidal component is generated almost entirely by external, three–dimensionally shaped coils, so that large plasma currents are not needed.

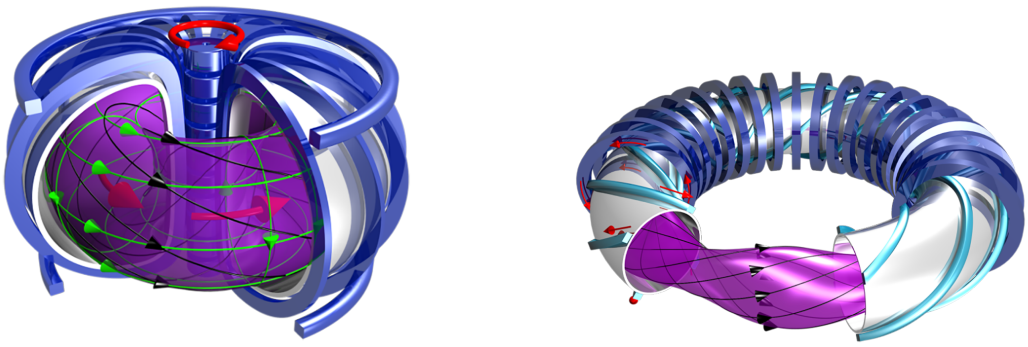

(a) Tokamak concept. (b) Stellarator concept.

Figure 1.2: On the left, the tokamak concept; on the right, the stellarator concept. The black curves represent the magnetic field lines. In the tokamak case, the plasma current is indicated by red arrows, while the green curves show the toroidal and poloidal fields [6].

In both cases, charged particles spiral around magnetic field lines while drifting slowly across them under the influence of field curvature, gradients, and collisions. Ideally, if particles were perfectly tied to field lines and the field lines were perfectly nested, radial transport would be extremely small. In reality, several mechanisms contribute to cross–field transport and thus degrade confinement. These mechanisms are conventionally grouped into classical, neoclassical, and turbulent transport.

Classical transport arises from binary Coulomb collisions in a homogeneous magnetic field and can be derived from kinetic theory under the assumption of a straight, uniform field. In toroidal devices, however, the magnetic geometry introduces additional drifts and trapped–particle orbits that strongly modify collisional transport. This enhanced transport, which still stems from collisional processes but depends sensitively on toroidal geometry, is referred to as neoclassical transport. Neoclassical theory predicts, for example, the existence of trapped orbits and bootstrap currents, and provides an important baseline for understanding confinement in magnetized plasmas.

Despite its sophistication, neoclassical theory alone fails to explain experimentally observed heat and particle fluxes in fusion plasmas, particularly in regimes relevant to reactor operation. Measured transport levels consistently exceed neoclassical predictions, and the discrepancy is attributed to turbulence driven by microinstabilities such as ion-temperature-gradient (ITG), trapped-electron (TEM), and electron-temperature-gradient (ETG) modes. These instabilities extract free energy from background density and temperature gradients, interact nonlinearly, and redistribute energy across spatial scales, ultimately reaching saturation through nonlinear energy transfer into stable modes. Their cumulative effect manifests macroscopically as a substantial enhancement of radial transport. Accurately capturing this multiscale interplay in a computationally tractable way remains one of the central challenges of fusion plasma physics. Gyrokinetic simulations provide detailed insight into this highly complex behaviour and are essential for understanding the physics of turbulent heat transport. However, their computational cost severely limits their direct use in integrated modelling or real-time control. This motivates the development of simplified descriptions that preserve the essential macroscopic effects of turbulence while remaining efficient enough to be implemented in transport solvers and control-oriented models. A widely adopted approach is to represent radial heat transport through effective advection–diffusion (AD) equations, which describe the evolution of macroscopic quantities such as the ion and electron temperatures.

From a modelling perspective, AD equations offer several attractive features. They are conceptually simple and provide an intuitive picture in which turbulence is represented as an effective diffusion (and possibly advection) that transports heat down its gradient, analogously to molecular diffusion but with greatly enhanced coefficients. They are computationally inexpensive, allowing for fast time evolution of profiles on transport time scales, and can be readily incorporated into integrated modelling frameworks that couple equilibrium, transport, and sources. Moreover, their parameters—the effective transport coefficients—can, in principle, be inferred from experiments or from more detailed simulations.

However, these advantages come at the price of strong assumptions. The notion of an effective diffusion coefficient presupposes that the turbulent flux at a given location can be expressed as a local and instantaneous functional of the local gradients. In other words, it

assumes linearity of the flux with respect to small perturbations, quasi–stationarity of the response on the time scales of interest, and spatial locality of transport. In real turbulent plasmas, these assumptions often do not hold. Nonlinear effects can induce cross–scale couplings that are not captured by linear closures, and nonlocal interactions may give rise to fluxes that depend on gradients over extended radial regions rather than strictly locally.

Furthermore, the effective transport coefficients are scale–dependent quantities whose inferred values can vary with the method used: different diagnostics or perturbative approaches may yield different results for the same nominal plasma state if the underlying assumptions of advection–diffusion closures are not satisfied. This raises fundamental questions about the range of validity of such models and about how to interpret the inferred coefficients in relation to the turbulence itself.

Motivation and scope of this thesis

The research presented in this thesis is motivated by the need to better understand turbulent heat transport in magnetised plasmas by analysing how externally injected signals are spread and modulated by the turbulence, and to clarify the limits of applicability of AD models in describing such processes.

We perform high-fidelity gyrokinetic simulations of a temperature–gradient–driven TEM turbulence regime, in which a modulated Electron Cyclotron Resonance Heating (ECRH) source is imposed as a controlled perturbation. The resulting temperature response is analysed in the frequency domain, allowing us to examine how turbulence affects the coherence between the imposed heat-modulation and the plasma response signals, and to extract both amplitude and phase information as a function of radial position. This information is then interpreted through a linear advection–diffusion model to infer effective diffusion and advection coefficients, and to assess the limits of validity of such a closure in the presence of fully developed turbulence. All simulations are carried out with the Gyrokinetic Electromagnetic Numerical Experiment (GENE) code, employing a new Electron Cyclotron Current Drive (ECCD) deposition module developed by the Plasma Micro-Turbulence Group at the Dutch Institute for Fundamental Energy Research (DIFFER). By combining gyrokinetic modelling with perturbative transport analysis, this work aims to bridge both ends of the modelling spectrum: the detailed, high-dimensional dynamics of plasma microturbulence and the simplified, reduced macroscopic picture of AD models. The goal is to establish a methodology for identifying nonlocal or nonlinear signatures that mark the breakdown of simple AD closures. In the longer term, such an approach may support the development of more accurate and predictive transport models for use in integrated modelling and control strategies in future fusion devices.

Chapter 2

Plasma Turbulence and Gyrokinetics

Plasma turbulence governs cross-field transport in magnetically confined fusion plasmas and ultimately sets the performance of devices such as tokamaks and stellarators. Its dynamics emerge from the interplay between background gradients and microinstabilities, and nonlinear interactions that redistribute energy across spatial and temporal scales. Understanding these processes requires a framework capable of capturing the essential kinetic physics while remaining numerically tractable. Gyrokinetic theory provides this framework[7]: by averaging over the fast gyromotion, it exploits the natural scale separation of magnetised plasmas, and yields a set of equations that describe turbulence with high fidelity. This chapter gives an overview of the physical concepts underlying plasma turbulence and outlines the gyrokinetic formulation used throughout this work.

2.1 Microinstabilities

A variety of instabilities can be excited on spatial scales comparable to the ion and electron gyroradii, and can be classified according to both their spatial scale and the type of equilibrium gradient that provides their free energy [8]. Among the most relevant microinstabilities are the ion–temperature–gradient (ITG) and electron–temperature–gradient (ETG) modes, which are primarily driven by the ion and electron temperature gradients, respectively, and the trapped–electron mode (TEM), associated with the dynamics of magnetically trapped electrons and often further distinguished into temperature–gradient–driven (∇T-TEM) and density–gradient–driven (∇n-TEM) branches.

The present work focuses on the TEM turbulence, that, together with ITG modes, is widely regarded as one of the main drivers of heat transport in fusion devices [9].

In the low–β plasma approximation,[1] where the total energy content is dominated by

[1]The plasma β, also called normalised pressure, is defined as $\beta = p/(B^2/2\mu_0)$ and measures the ratio between plasma pressure and magnetic energy density.

the background magnetic field [10], fluctuations of the magnetic field are neglected. Within this framework, the TEM instabilities can, to a very good approximation, be described solely in terms of perturbations of the electric field, with the perturbed field entirely determined by the electrostatic potential via $\mathbf{E} = -\nabla\phi$. This condition is known as electrostatic limit. Within this limit, a unifying feature of many relevant microinstabilities is that they can be interpreted as different ways of destabilising an underlying so-called drift wave.

2.1.1 Drift Waves

Drift waves describe the coupling between equilibrium gradients and electric–field perturbations in magnetised plasmas. To understand the basics, let us consider a simple model in slab geometry [8, 11] with a uniform magnetic field $\mathbf{B} = B\,\mathbf{e}_z$, so that the field lines are straight. The essential ingredient for the drift wave is a background density gradient, that is taken as

$$\frac{\partial n_0}{\partial x} < 0.$$

Let $x_1(y,t)$ denote a small displacement of the guiding–center positions. A fluid element that is located at position x at time t originates from $x - x_1(y,t)$, so that the density at (x,y) can be written as

$$n(x,y,t) = n_0\big(x - x_1(y,t)\big) \approx\ n_0(x) - \frac{\partial n_0}{\partial x}\, x_1(y,t). \tag{2.1}$$

The density perturbation is therefore

$$n_1(x,y,t) = n(x,y,t) - n_0(x)\ \approx\ -\frac{\partial n_0}{\partial x}\, x_1(y,t). \tag{2.2}$$

Because $\partial n_0/\partial x < 0$, n_1 is in phase with x_1.

Since electrons rapidly move along magnetic field lines (the z–direction in this slab picture), they establish an adiabatic response, thus [8]:

$$\frac{n_1(x,y,t)}{n_0(x)}\ =\ \frac{e\,\phi_1(x,y,t)}{T_e}, \tag{2.3}$$

where $e > 0$ denotes the elementary charge. From here, it follows that the electrostatic potential generated by the density perturbation ϕ_1 is in phase with n_1 and, through Eq. (2.2), also in phase with x_1. Consider now a single sinusoidal perturbation evaluated at a fixed position x_0:

$$x_1(y,t) = A\sin\big(k_y y - \omega t\big), \tag{2.4}$$

with amplitude A, wavenumber k_y and frequency ω. Equation (2.2) implies that the density and potential perturbations have the same form

$$n_1(y,t) = \hat{n}\sin\big(k_y y - \omega t\big), \qquad \phi_1(y,t) = \hat{\phi}\sin\big(k_y y - \omega t\big), \tag{2.5}$$

with constants $\hat{n}, \hat{\phi} > 0$. In the electrostatic limit, the perturbed electric field is

$$\mathbf{E}_1 = -\nabla\phi_1 \;=\; -\frac{\partial\phi_1}{\partial y}\,\mathbf{e}_y, \tag{2.6}$$

so that, for the sinusoidal perturbation,

$$E_{1y}(y,t) = -\frac{\partial\phi_1}{\partial y} = -\hat{\phi}\,k_y\cos(k_y y - \omega t). \tag{2.7}$$

The electric field is thus shifted by $\pi/2$ in phase along y with respect to ϕ_1 (and to x_1 and n_1). In the presence of the background magnetic field $\mathbf{B}_0 = B_0\mathbf{e}_z$, the $E \times B$ drift is

$$\mathbf{v}_{E\times B} = \frac{\mathbf{E}_1 \times \mathbf{B}_0}{B_0^2} = \frac{E_{1y}}{B_0}\,\mathbf{e}_x, \tag{2.8}$$

so that

$$v_{E\times B,x}(y,t) = \frac{E_{1y}(y,t)}{B_0} = -\frac{\hat{\phi}\,k_y}{B_0}\cos(k_y y - \omega t). \tag{2.9}$$

From Eqs. (2.4)–(2.9) it follows that the displacement and density perturbations vary as $x_1, n_1 \propto \sin(k_y y - \omega t)$, whereas the $E \times B$ drift satisfies $v_{E\times B,x} \propto -\cos(k_y y - \omega t)$. The radial velocity is therefore phase–shifted by $\pi/2$ with respect to the displacement, and this phase relation implies that the $E \times B$ drift simply advects the perturbation along the y–direction without doing net work against the background gradient: the sequence "radial displacement $\rightarrow$ density perturbation $\rightarrow$ potential perturbation $\rightarrow$ $E \times B$ drift $\rightarrow$ new displacement" closes without net amplification, resulting in a marginally stable drift wave.

2.1.2 Trapped-Electron Modes

In a toroidal configuration, the magnetic field strength varies along a field line, so that a finite fraction of particles becomes magnetically trapped. These trapped particles bounce between mirror points and experience average curvature and ∇B drifts, in contrast to passing particles, for which these drifts tend to average out over a full poloidal transit. As a result, the response of passing particles to a drift–wave–like perturbation is essentially the same as in the basic drift–wave picture discussed above, whereas the nonzero average drift of trapped particles can introduce an instability mechanism.

A simplified description of this mechanism can be obtained by modifying the drift–wave model in two ways [12]. First, the electron response is no longer assumed to be purely adiabatic. Second, the effect of trapped particles is mimicked by adding a constant drift velocity v_d in the y direction, taken to be opposite for ions and electrons. This drift moves trapped particles originally located at (x, y_0) to $(x, y_0 \pm \Delta y)$, with the plus sign for ions. In the absence of a density perturbation, the background density depends only on x, so this drift does not lead to any net charge accumulation. However, in the presence of a drift–wave–like radial excursion of guiding centers $x_1(y)$, the local density becomes $n(x,y) = n_0(x) + n_1(y)$, and the oppositely directed drifts of ions and electrons

now transport slightly different densities in and out of a given y–location. This imbalance between the incoming and outgoing fluxes of electrons and ions produces a net charge density $\rho_1(y_0)$, which can be shown to be proportional to the y–derivative of the density perturbation [12],

$$\rho_1(y) \;\propto\; \frac{\partial n_1(y)}{\partial y} \;\propto\; \frac{\partial x_1(y)}{\partial y}, \tag{2.10}$$

and is therefore shifted by $\pi/2$ with respect to the original density perturbation.

In the electrostatic limit, this charge density gives rise to an electrostatic potential ϕ_1 that is $\pi/2$ out of phase with n_1. The corresponding electric field $E_{1y} = -\partial\phi_1/\partial y$ and the associated $E \times B$ drift in the radial direction, $v_{E\times B,x} \propto E_{1y}$, are then in phase with the original guiding–center excursion $x_1(y)$. In contrast to the drift–wave case, where the $E \times B$ velocity is shifted by $\pi/2$ and merely advects the perturbation, the $E \times B$ drift of trapped particles now adds to the existing radial excursion, thereby enhancing its amplitude. Since the density perturbation $n_1 \propto -x_1\,\partial_x n_0$ is directly proportional to both the guiding–center displacement and the background density gradient, this feedback loop causes the amplitude of the perturbation to grow. The following chain summarises the mechanism [13]: $\phi_1 \longrightarrow \mathbf{v}_{E\times B} \longrightarrow n_1 \longrightarrow \mathbf{v}_{\nabla B}^{e,i} \longrightarrow \phi_1$. The previous mechanism relies primarily on a background density gradient and is therefore referred to as a ∇n-TEM. However, the magnetic drifts of trapped particles scale with the particle energy and thus depend on temperature, so that electron temperature gradients can introduce an additional drive: when the temperature gradient is sufficiently steep, this drive can destabilise trapped electrons, giving rise to a temperature–gradient–driven trapped–electron mode (∇T–TEM). The previous chain is modified by incorporating the temperature perturbation.

2.2 Gyrokinetic Theory

At mesoscopic scales, a magnetised plasma can be described through a distribution function $f_j(\mathbf{x}, \mathbf{v}, t)$, defined on a six-dimensional phase space constructed from the 3-dimensional position vector $\mathbf{x}$ and a three-dimensional velocity vector $\mathbf{v}$, where j labels the ion and electron species (with the possibility of including more than two species). The evolution of the distribution functions is governed by the Fokker–Planck equations [14]:

$$\frac{\partial f_j}{\partial t} + \mathbf{v}\cdot\nabla_{\mathbf{x}} f_j + \frac{q_j}{m_j}(\mathbf{E} + \mathbf{v}\times\mathbf{B})\cdot\nabla_{\mathbf{v}} f_j = \sum_{j'} C[f_j, f_{j'}], \quad j \in \{i, e\} \tag{2.11}$$

The interactions among particles are represented by the collision operator C, which enters as a sum over all species present in the plasma.[2] The previous equations must then be coupled to Maxwell's equations, which determine the evolution of the electromagnetic fields.

[2] If the collision operator is set to zero, equation 2.11 reduces to the collisionless Vlasov equation. The terms Vlasov and Fokker–Planck are sometimes used interchangeably.

Direct numerical solution of the full kinetic system in fusion-relevant regimes is computationally prohibitive. Gyrokinetic theory addresses this challenge through a systematic reduction of the full system appropriate for strongly magnetised plasmas. Exploiting the separation between the fast gyromotion around magnetic field lines and the slower motion of guiding centres, gyrokinetics averages over the gyrophase and reduces the dimensionality of velocity space. Under appropriate ordering assumptions, the resulting gyrokinetic equations govern the evolution of a reduced distribution function in a five–dimensional phase space, coupled to electromagnetic fields. This reduction eliminates the need to resolve the gyromotion while retaining the dynamics of low–frequency microinstabilities and the associated turbulent transport [15, 16, 17, 18].

The transition from the full kinetic framework to gyrokinetics is achieved by removing the degree of freedom associated with the fast gyromotion. This reduction is justified provided an appropriate ordering scheme is adopted. Introducing an ordering parameter ϵ_t, with respect to which all the relevant quantities are expanded, a possible gyrokinetic ordering is [7]:

$$\frac{k_\parallel}{k_\perp} \sim \frac{n_1}{n} \sim \frac{T_1}{T} \sim \frac{q\,\phi_1}{T} \sim \frac{B_1}{B} \sim \frac{\omega}{\Omega_c} \sim \epsilon_t \ll 1, \tag{2.12}$$

where q is the charge, and $k_\parallel$, $k_\perp$ are the parallel and perpendicular wavenumbers, respectively.[3] Ω_c is the characteristic frequencies of the gyration (i.e, Larmor frequency) and ω is the characteristic frequency of the perturbation. The symbols n, ϕ and T denote the density, electrostatic potential and temperature, which are split into equilibrium and perturbed parts; the subscript 1 labels the perturbations [19].

The anisotropy of the turbulent fluctuations implied by the wavenumber ordering, is complemented by an additional ordering between perpendicular length scales

$$\frac{\rho}{L_G} \sim \epsilon_t \ll 1, \tag{2.13}$$

where ρ denotes the gyroradius and L_G the characteristic gradient scale length of density, temperature and magnetic field.

In order to eliminate the fast gyromotion from the description of single-particle dynamics, one introduces guiding-center coordinates. In a field-aligned system $\mathbf{x} = (x, y, z)$, the instantaneous particle position is decomposed as $\mathbf{x} = \mathbf{X} + \boldsymbol{\rho}_j(\xi)$, where $\mathbf{X}$ denotes the gyrocenter and $\boldsymbol{\rho}_j(\xi)$ is the Larmor-radius vector of species j, which rotates around $\mathbf{X}$ with gyroangle ξ and fixed modulus ρ_j (Fig. 2.1). Formally, this corresponds to a change of phase-space variables from $(\mathbf{x}, \mathbf{v})$ to $(\mathbf{X}, \mu, E, \xi)$, where μ is the magnetic moment and E the particle energy. The transformation is constructed as a near-identity Lie transform, expanded in the small parameter ϵ_t introduced by the gyrokinetic ordering [7]. The full derivation is outside the scope of the present work.

From a computational point of view, it is convenient to separate the macroscopic evolution of the plasma from the effects of microturbulence. To this end, the distribution

[3] Parallel and perpendicular are defined with respect to the magnetic field line.

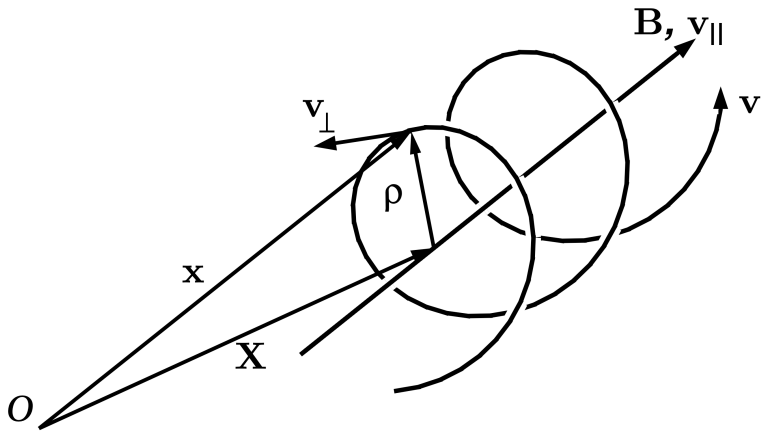

Figure 2.1: Guiding center coordinates. Adapted from [20]

function is decomposed into a static background part $f_{0,j}$ and a perturbation $f_{1,j}$ [21]:

$$f_j = f_{0,j} + f_{1,j}, \tag{2.14}$$

where, the background distribution function $f_{0,j}$ is assumed to be Maxwellian,

$$f_{0,j} = \pi^{-3/2} e^{-\left(v_\parallel^2 + \mu B_0\right)}. \tag{2.15}$$

According to the gyrokinetic ordering, the two contributions to the full distribution function f_j satisfy $f_{1,j}/f_{0,j} \sim \epsilon_t$. Analogously, the electrostatic potential and the magnetic vector potential are expanded as

$$\phi(\mathbf{x}) = \phi_0(\mathbf{x}) + \phi_1(\mathbf{x}), \tag{2.16}$$

$$\mathbf{A}(\mathbf{x}) = \mathbf{A}_0(\mathbf{x}) + \mathbf{A}_1(\mathbf{x}), \tag{2.17}$$

It is preferable, in order to write the gyrokinetic equations in compact form, to introduce the modified distribution function[4]:

$$g_j = f_{1,j} + \frac{2q_j}{m_j v_{Tj}} v_\parallel \langle A_{1\parallel} \rangle_\xi f_{0,j}, \tag{2.18}$$

where, $\langle ... \rangle_\xi$ denotes the gyroaverage, $v_{Tj} = \sqrt{2T_{0,j}/m_j}$ is the thermal velocity, with $T_{0,j}$ and m_j the background temperature and mass of species j, respectively. Furthermore, it is convenient to represent the spatial dependence in Fourier space, using the wave numbers k_x and k_y that combine to the perpendicular wave number $k_\perp$ through: $k_\perp^2 = g^{xx}k_x^2 + 2g^{xy}k_x k_y + g^{yy}k_y^2$, where g^{ij} is the metric tensor.

[4]All quantities are expressed in normalised units; the specific normalisation is introduced later.

The gyrokinetic equations can then be written as [21]

$$\frac{\partial g_j}{\partial t} = \mathcal{Z} + \mathcal{L}[g_j] + \mathcal{N}[g_j], \tag{2.19}$$

where $\mathcal{Z}$ is a constant term, $\mathcal{L}$ is a linear operator, and $\mathcal{N}$ a nonlinear operator:

$$Z = \frac{T_{0,j}}{q_j B_0}(2v_\parallel^2 + \mu B_0) K_x \left[\omega_n + \left(v_\parallel^2 + \mu B_0 - \frac{3}{2}\right)\omega_{Tj}\right] \delta_{k_x,0}\,\delta_{k_y,0}\, f_{0,j}, \tag{2.20}$$

$$\begin{aligned}\mathcal{L}[g_j] = &\underbrace{\left(\omega_n + \left(v_\parallel^2 + \mu B_0 - \frac{3}{2}\right)\omega_{Tj}\right) f_{0,j}\, ik_y\chi_j}_{\text{gradient drive}} + \underbrace{\beta\,\frac{T_{0j}}{q_j B_0^2}\, v_\parallel^2\,\omega_p\,\Gamma_{jy}}_{\text{pressure}} - \underbrace{\frac{v_{Tj}}{JB_0}\, v_\parallel\,\Gamma_{jz}}_{\text{parallel}} \\ &\underbrace{- \frac{T_{0j}}{q_j B_0}\left(2v_\parallel^2 + \mu B_0\right)(K_y\Gamma_{jy} + K_x\Gamma_{jx})}_{\text{curvature}} + \underbrace{\frac{v_{Tj}}{2JB_0}\,\mu\,\frac{\partial B_0}{\partial z}\,\frac{\partial f_j}{\partial v_\parallel}}_{\text{trapping}} + \underbrace{\langle C_j(f_1)\rangle}_{\text{collisions}}.\end{aligned} \tag{2.21}$$

with the curvatures $K_{x,y}$ and the auxiliary fields $\Gamma x, y, z$, defined as

$$K_x = -\frac{L_{\text{ref}}}{B_{\text{ref}}}\left(\frac{\partial B_0}{\partial y} + \frac{\gamma^2}{\gamma^1}\frac{\partial B_0}{\partial z}\right), \tag{2.22}$$

$$K_y = \frac{L_{\text{ref}}}{B_{\text{ref}}}\left(\frac{\partial B_0}{\partial x} - \frac{\gamma^3}{\gamma^1}\frac{\partial B_0}{\partial z}\right), \tag{2.23}$$

$$\Gamma_{j,\{x,y\}} = ik_{x,y}\, g_j + \frac{q_j}{T_{0j}}\, f_{0,j}\, ik_{x,y}\,\chi_j, \tag{2.24}$$

$$\Gamma_{jz} = \frac{\partial g_j}{\partial z} + \frac{q_j}{T_{0,j}}\, f_{0,j}\,\frac{\partial \chi_j}{\partial z} + \frac{v_{Tj} q_j}{T_{0,j}}\, v_\parallel \mu f_{0,j}\, A_k\,\frac{\partial B_0}{\partial z}, \tag{2.25}$$

and the field χ_j, that collects the scalar and vector potentials according to

$$\chi_j = \langle\phi\rangle_\xi - v_{Tj} v_\parallel \langle A_{1\parallel}\rangle_\xi, \tag{2.26}$$

and $\gamma^{1,2,3}$ are combinations of the metric elements

$$\gamma^1 = g^{xx}g^{yy} - g^{yx}g^{xy}, \qquad \gamma^2 = g^{xx}g_{yz} - g^{yx}g^{xz}, \qquad \gamma^3 = g^{xy}g^{yz} - g^{yy}g^{xz}. \tag{2.27}$$

The constant term $\mathcal{Z}$ contributes only when $k_x = k_y = 0$ which accounts for the fact that in presence of magnetic curvature and background density or temperature gradients, a purely equilibrium distribution ($f_1 = 0$) cannot be a solution. These gradients are given by

$$\omega_n = -\frac{L_{\text{ref}}}{n_{0,j}}\frac{\partial n_{0,j}}{\partial x}, \qquad \omega_{Tj} = -\frac{L_{\text{ref}}}{T_{0,j}}\frac{\partial T_{0,j}}{\partial x}. \tag{2.28}$$

The first contribution in Eq. (2.21) is the gradient–drive term, which represents the energy injection due to equilibrium density and temperature gradients. The second term accounts for the effect of plasma pressure, which enters through the normalised pressure

$$\beta = \frac{n_{\text{ref}} T_{\text{ref}}}{B_{\text{ref}}^2/(2\mu_0)}, \tag{2.29}$$

and through the pressure gradient

$$\omega_p = -\frac{L_{\text{ref}}}{n_{\text{ref}} T_{\text{ref}}} \frac{\partial p}{\partial x}. \tag{2.30}$$

The third and fourth terms describe, respectively, the parallel dynamics and the effects of magnetic curvature. The fifth term represents the mirror force responsible for the presence of trapped particles, while the last term is the collision operator.

Finally, the nonlinear term $\mathcal{N}[g_j]$ is [21]:

$$\mathcal{N}[g_j] = \sum_{\mathbf{k}'_\perp} (k'_x k_y - k_x k'_y)\, \chi(\mathbf{k}'_\perp)\, g_j(\mathbf{k}_\perp - \mathbf{k}'_\perp), \tag{2.31}$$

which express the so-called $\mathbf{E} \times \mathbf{B}$ nonlinearity. This term couples different wavenumbers and thus represents the nonlinear interaction between modes. The coupling involves triads of wavevectors and is commonly referred to as a triplet interaction. Through this process, energy is redistributed among the eigenmodes of the linear operator. When energy is nonlinearly transferred from unstable to stable modes, it provides a saturation mechanism that limits the otherwise exponential growth of unstable modes.

Numerically, the evaluation of $\mathcal{N}[g_j]$ is computationally expensive, as it corresponds to a discrete convolution. During numerical integration, g_j and χ_j are transformed from Fourier space to real space, the nonlinear term is computed, and the result is transformed back to Fourier space. The number and cost of these operations make the nonlinear term the dominant contribution to the overall computational expense of gyrokinetic simulations.

These equations are typically solved either in linear form, to determine microinstability spectra and growth rates, or in fully nonlinear form, to compute developed turbulence and the associated transport fluxes.

In the present work, the perturbative analysis is based on simulations of the full nonlinear gyrokinetic system.

2.2.1 Flux-Tube Domain

To solve the gyrokinetic equation numerically, the magnetic equilibrium geometry must be specified. This equilibrium is not evolved consistently with the turbulent fluctuations, but is instead provided as an input [21]. Although simulating the entire tokamak volume is possible in principle, the computational cost can be prohibitive. Therefore, often simulations are performed in a so-called flux-tube domain [22], which reduces the computational cost while retaining the essential physics.

In the flux-tube geometry (Fig. 2.2), the full plasma volume is reduced to a narrow spatial region surrounding a single magnetic field line, highly elongated along the parallel direction and comparatively narrow in the binormal direction. This construction exploits the strong anisotropy of turbulence, $k_\parallel \ll k_\perp$, implying that the parallel correlation length $L_\parallel$ is much larger than the perpendicular one $L_\perp$. To capture all turbulence-relevant dynamics (apart from global effects), the flux-tube must remain small compared with equilibrium scale lengths, yet large enough to accommodate the turbulent structures and avoid unphysical effects [21, 22].

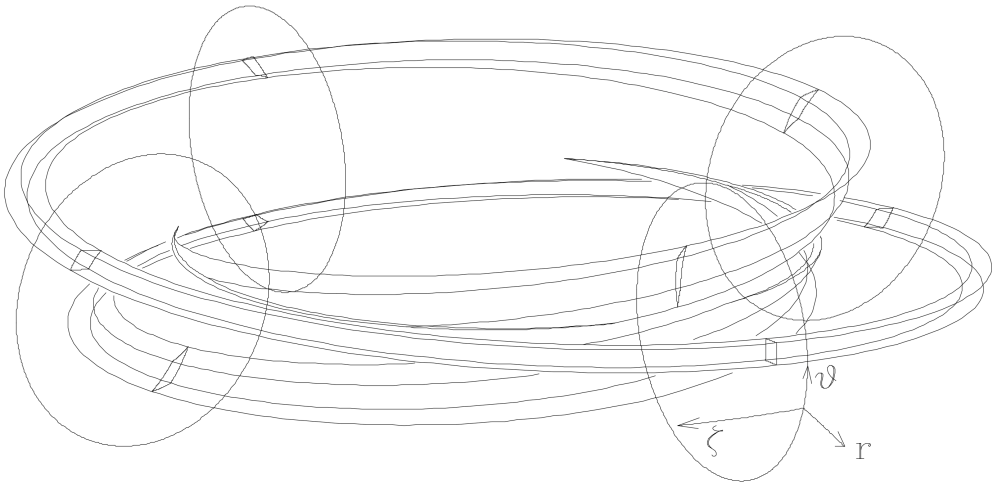

Figure 2.2: Rectangular computational domain mapped onto a flux-tube in a torus. Adapted from [22].

The flux-tube coordinate formalism is based on the Clebsch representation of the magnetic field:

$$\mathbf{B} = \nabla\alpha \times \nabla\psi, \tag{2.32}$$

where ψ is the poloidal magnetic flux, (θ, ζ) are the poloidal and toroidal angles (as shown in Fig. 2.2), and α is a field–line label: $\alpha = \zeta - q(\psi)\,\theta$. The triplet (ψ, θ, ζ) is known as Boozer coordinates [4]. Because $\mathbf{B}\cdot\nabla\psi = 0$, $\mathbf{B}\cdot\nabla\alpha = 0$, both ψ and α are constant along a given field line and therefore are a natural coordinate choice for the plane perpendicular to $\mathbf{B}$ in the flux-tube. As for the coordinate along the field line, the most convenient choice is the Boozer poloidal angle: $z = \theta \in [-\pi, \pi]$.

It is worth noting that, since the Boozer coordinates (ψ, θ, ζ) are not orthogonal, the flux-tube coordinates (ψ, α, z) will form a non orthogonal coordinate system as well [12].

Thus, a rectangular box in (ψ, α, z) is mapped to a curved, sheared region of the torus, embedded in the fixed laboratory frame. It is advantageous to rescale the perpendicular coordinates to feature a physical dimension of length:

$$x = \frac{q_0}{B_0 r_0}\,(\psi - \psi_0), \qquad y = \frac{r_0}{q_0}\,(\alpha - \alpha_0), \tag{2.33}$$

where (ψ_0, α_0) denote the Clebsch coordinates of the field line that defines the centre of the flux-tube, r_0 is the distance of this field line from the magnetic axis, and B_0 is the magnetic-field strength on the magnetic axis. To clarify the physical meaning of these coordinates, consider first x. Close to the magnetic axis, the poloidal flux scales as $\psi \propto B_{\mathrm{pol}} r^2$, with r the distance from the magnetic axis. Writing $r = r_0 + \delta r$ and expanding $\psi - \psi_0$ to first order in δr, one finds

$$x = \frac{q_0}{B_0 r_0}\,(\psi - \psi_0) \;\approx\; \frac{q_0 B_{\mathrm{pol}}}{B_0}\,\delta r, \tag{2.34}$$

so that, for a flux-tube of small perpendicular extent ($\delta r \ll r_0$), x is proportional to the radial deviation δr from the central field line. Similarly, the coordinate y is obtained by multiplying the angular deviation $\alpha - \alpha_0$ by a length scale r_0/q_0, so that y measures an arc length in the binormal direction. Since the perpendicular extent of the box is small compared with equilibrium scale lengths, equilibrium quantities can be expanded to first order around the central field line. For example, the temperature profile can be written as

$$T(x) \;\approx\; T(x_0) + \frac{\mathrm{d}T}{\mathrm{d}x}(x - x_0), \tag{2.35}$$

where the gradient is assumed to be constant, and similarly for density and other equilibrium profiles. Also the safety factor $q(x)$ can be expanded:

$$q(x) \approx q_0 + \frac{\mathrm{d}q}{\mathrm{d}x}(x - x_0) = q_0 \left(1 + \hat{s}\frac{x - x_0}{x_0}\right) \tag{2.36}$$

leading to the (constant) magnetic shear

$$\hat{s} = \frac{x_0}{q_0}\frac{\mathrm{d}q}{\mathrm{d}x}. \tag{2.37}$$

which is a measure of how the twisting of the magnetic field changes through the torus.

For any fluctuating quantity F in the flux-tube, the boundary conditions in x and y are taken to be periodic

$$F(x + L_x, y, z) = F(x, y, z), \tag{2.38}$$
$$F(x, y + L_y, z) = F(x, y, z), \tag{2.39}$$

so that it can be expanded in Fourier series

$$F(x, y, z, t) = \sum_{k_x}\sum_{k_y} \hat{F}(k_x, k_y, z, t)\, \exp\left(ik_x x + ik_y y\right), \tag{2.40}$$

with perpendicular wavenumbers given by

$$k_{x,y} = \ell\, \frac{2\pi}{L_{x,y}}, \qquad \ell \in \mathbb{Z}. \tag{2.41}$$

We denote the minimum non-zero perpendicular wavenumbers by $k_{x,y}^{\min} = 2\pi/L_{x,y}$.

Along the parallel direction, the so–called twist–and–shift boundary condition is adopted. We consider a flux-tube that spans a single poloidal turn, so that the parallel coordinate is taken as $z \in [-\pi, \pi]$. In Fourier space with respect to the perpendicular coordinates (x, y), the boundary condition reads

$$\hat{F}(k_x, k_y, \pi) = \hat{F}(k_x + N k_x^{\min}, k_y, -\pi)\,(-1)^N, \tag{2.42}$$

where N satisfies

$$N = \frac{2\pi\hat{s}k_y^{\min}}{k_x^{\min}} \tag{2.43}$$

This condition reflects the fact that, in the presence of magnetic shear, a field line on a flux surface does not return to exactly the same perpendicular position after one poloidal turn: when the same physical point is revisited at $z = \pi$, it is shifted in the binormal direction. In Fourier space this shear-induced shift appears as a coupling between modes with radial wavenumbers k_x and $k_x + Nk_x^{\min}$.

Finally, the geometry of the magnetic equilibrium must be specified. Two main options are available: one may either import a numerical MHD equilibrium (e.g. from an equilibrium code) or adopt an analytic model geometry. A widely used analytic model for tokamaks is the $\hat{s}$–α geometry [22], which describes Shafranov–shifted circular flux surfaces and provides a good approximation to a true MHD equilibrium near the magnetic axis. For finite plasma β, the Shafranov shift is characterised by the quantity

$$\alpha_{\mathrm{MHD}} = \frac{q_0^2 \beta}{R_0} \sum_j (\omega_n + \omega_{Tj})\, n_{0,j} T_{0,j}, \tag{2.44}$$

where the normalised density and temperature gradients ω_n and ω_{Tj} appear.

The metric tensor in this case reads:

$$[g^{ij}] = \begin{pmatrix} 1 & \hat{s}\, z - \alpha_{\mathrm{MHD}} \sin z & 0 \\ \hat{s}\, z - \alpha_{\mathrm{MHD}} \sin z & 1 + \left(\hat{s}\, z - \alpha_{\mathrm{MHD}} \sin z\right)^2 & 1/r \\ 0 & 1/r & 1/r^2 \end{pmatrix}, \tag{2.45}$$

The choice of the $\hat{s}$–α geometry in this work is motivated by its simplicity and its widespread use in the literature, despite not being fully self-consistent [23].

Chapter 3

Plasma-Wave Interaction

In tokamaks, one of the most effective techniques for non-inductive current drive, auxiliary heating, and the suppression of MHD instabilities [24, 25] is the injection of electron-cyclotron (EC) waves with millimetre-scale wavelengths under fusion-relevant magnetic fields of several tesla. To understand the underlying mechanism, we recall that wave propagation in a plasma is governed by the medium's electrodynamic response: starting from Maxwell's equations, one derives a wave equation whose solutions are constrained by the appropriate dispersion relations [26, 27, 28, 29].

3.1 General Wave Equation in Linear Description of a Plasma

Our starting point is Ampere and Faraday's equations:

$$\nabla \times \mathbf{E} = -\frac{\partial \mathbf{B}}{\partial t} \quad \text{(Faraday's Law)} \tag{3.1}$$

$$\nabla \times \mathbf{B} = \mu_0 \mathbf{j} + \mu_0 \epsilon_0 \frac{\partial \mathbf{E}}{\partial t} \quad \text{(Ampere-Maxwell Law).} \tag{3.2}$$

To derive a wave equation for the electric field $\mathbf{E}$, we take the curl of Faraday's Law (Eq. (3.1)):

$$\nabla \times (\nabla \times \mathbf{E}) = -\nabla \times \left(\frac{\partial \mathbf{B}}{\partial t} \right) = -\frac{\partial}{\partial t} (\nabla \times \mathbf{B}),$$

substituting the Ampere-Maxwell Law (Eq. (3.2)) into this expression yields:

$$\nabla \times (\nabla \times \mathbf{E}) = -\frac{\partial}{\partial t} \left(\mu_0 \mathbf{j} + \mu_0 \epsilon_0 \frac{\partial \mathbf{E}}{\partial t} \right),$$

from Ohm's law: $\mathbf{j} = \boldsymbol{\sigma} \cdot \mathbf{E}$, where $\boldsymbol{\sigma}$ is the conductivity tensor, thus, substituting this relationship we find a version of the Helmholtz equation for a conductive medium:

$$\nabla \times (\nabla \times \mathbf{E}) + \frac{\partial}{\partial t} \left(\mu_0 \boldsymbol{\sigma} \cdot \mathbf{E} + \mu_0 \epsilon_0 \frac{\partial \mathbf{E}}{\partial t} \right) = 0. \tag{3.3}$$

To solve this differential equation, we assume the electric field behaves as a plane wave, which can be expressed in complex notation as $\mathbf{E} \sim \mathbf{E}_0 e^{i(\mathbf{k}\cdot\mathbf{r}-\omega t)}$. This assumption allows us to replace the differential operators with algebraic terms:

$$\nabla \to i\mathbf{k} \quad \text{and} \quad \frac{\partial}{\partial t} \to -i\omega$$

applying these substitutions to Equation (3.3), we get:

$$i\mathbf{k} \times (i\mathbf{k} \times \mathbf{E}) + (-i\omega)\left(\mu_0 \boldsymbol{\sigma} \cdot \mathbf{E} + \mu_0 \epsilon_0 (-i\omega)\mathbf{E}\right) = 0$$

using the vector identity $\mathbf{A} \times (\mathbf{B} \times \mathbf{C}) = \mathbf{B}(\mathbf{A} \cdot \mathbf{C}) - \mathbf{C}(\mathbf{A} \cdot \mathbf{B})$, the first term becomes $\mathbf{k}(\mathbf{k} \cdot \mathbf{E}) - k^2\mathbf{E}$. Rearranging the equation gives:

$$\mathbf{k}\mathbf{k} \cdot \mathbf{E} - k^2 \mathbf{I} \cdot \mathbf{E} + \frac{\omega^2}{c^2}\left(\mathbf{I} + \frac{i}{\omega\epsilon_0}\boldsymbol{\sigma}\right) \cdot \mathbf{E} = 0$$

where we used $c^2 = 1/(\mu_0\epsilon_0)$ and $\mathbf{I}$ is the identity tensor. We now define the plasma's relative dielectric tensor, $\boldsymbol{\epsilon}$, which combines the vacuum displacement current and the plasma's conductive response:

$$\boldsymbol{\epsilon} = \mathbf{I} + \frac{i}{\omega\epsilon_0}\boldsymbol{\sigma}. \tag{3.4}$$

Substituting this definition yields the general dispersion relation for waves in plasmas:

$$\left(\mathbf{k}\mathbf{k} - k^2\mathbf{I} + \frac{\omega^2}{c^2}\boldsymbol{\epsilon}\right) \cdot \mathbf{E} = 0.$$

We call Dispersion Tensor the quantity:

$$\boldsymbol{\Lambda} = \left(\mathbf{k}\mathbf{k} - k^2\mathbf{I} + \frac{\omega^2}{c^2}\boldsymbol{\epsilon}\right). \tag{3.5}$$

For a non-trivial solution (i.e., $\mathbf{E} \neq 0$), we must have:

$$\det(\boldsymbol{\Lambda}) = \det\left(\mathbf{k}\mathbf{k} - k^2\mathbf{I} + \frac{\omega^2}{c^2}\boldsymbol{\epsilon}\right) = 0 \tag{3.6}$$

This result indicates that the behavior of waves (i.e., the relationship between ω and $\mathbf{k}$) is determined by the dielectric tensor $\boldsymbol{\epsilon}$, and thus by the conductivity tensor $\boldsymbol{\sigma}$. The next step is to find an explicit form for $\boldsymbol{\epsilon}$.

3.2 The Cold Plasma Dispersion Relation

The simplest, yet widely applicable, way for calculating the dielectric tensor is under the **cold plasma approximation**. This model captures the essential physics of wave propagation in the electron cyclotron frequency range. The core assumption is that the thermal motion of the plasma particles is negligible ($T \to 0$). This simplification ignores

pressure gradient effects and assumes all particles of a given species move coherently in response to the wave fields.

The basis for this model is the equation of motion (momentum conservation) for each species s (e.g., ions and electrons), which is governed by the Lorentz force:

$$m_s \left(\frac{\partial \mathbf{v}_s}{\partial t} + (\mathbf{v}_s \cdot \nabla)\mathbf{v}_s \right) = q_s(\mathbf{E} + \mathbf{v}_s \times \mathbf{B}) \tag{3.7}$$

Here, s is the species index, m_s is the mass, $\mathbf{v}_s$ is the fluid velocity, and q_s is the charge.

To analyse wave propagation, we linearise this equation by considering small perturbations around a stationary, uniform equilibrium. We expand the fields as:

$$\begin{aligned} \mathbf{v}_s &= \mathbf{v}_{s0} + \mathbf{v}_{s1} \\ \mathbf{E} &= \mathbf{E}_0 + \mathbf{E}_1 \\ \mathbf{B} &= \mathbf{B}_0 + \mathbf{B}_1 \end{aligned} \tag{3.8}$$

In our equilibrium, the plasma is stationary ($\mathbf{v}_{s0} = 0$) and there is no background electric field ($\mathbf{E}_0 = 0$). The magnetic field is a strong, static, and uniform background field, $\mathbf{B}_0$. The quantities with subscript '1' are the small, first-order perturbations caused by the wave. Substituting these into Equation (3.7) and keeping only first-order terms, we obtain the linearised momentum equation:

$$m_s \frac{\partial \mathbf{v}_{s1}}{\partial t} = q_s(\mathbf{E}_1 + \mathbf{v}_{s1} \times \mathbf{B}_0) \tag{3.9}$$

We again assume that all perturbed quantities vary as $\sim e^{i(\mathbf{k}\cdot\mathbf{r}-\omega t)}$, so $\frac{\partial}{\partial t} \to -i\omega$. Equation (3.9) becomes:

$$-i\omega m_s \mathbf{v}_{s1} = q_s(\mathbf{E}_1 + \mathbf{v}_{s1} \times \mathbf{B}_0)$$

To solve for $\mathbf{v}_{s1}$ in terms of $\mathbf{E}_1$, we align our coordinate system such that the static magnetic field $\mathbf{B}_0$ points along the z-axis, $\mathbf{B}_0 = B_0\hat{\mathbf{z}}$. The cross product is then $\mathbf{v}_{s1} \times \mathbf{B}_0 = (v_{s1,y}B_0, -v_{s1,x}B_0, 0)$. Thus, introducing the cyclotron frequency for species s, $\Omega_{cs} = q_s B_0/m_s$, which is the frequency of gyration for a charged particle around a magnetic field line, and rearranging the equations in matrix form, we obtain the following linear system which provides the relationship between the perturbed velocity and the perturbed electric field in the non-relativistic limit:

$$\begin{pmatrix} -i\omega & -\Omega_{cs} & 0 \\ \Omega_{cs} & -i\omega & 0 \\ 0 & 0 & -i\omega \end{pmatrix} \begin{pmatrix} v_{s1,x} \\ v_{s1,y} \\ v_{s1,z} \end{pmatrix} = \frac{q_s}{m_s} \begin{pmatrix} E_{1x} \\ E_{1y} \\ E_{1z} \end{pmatrix} \tag{3.10}$$

It is worth noting that, when relativistic effects become significant, m_s should be replaced by $\gamma_s m_s$, where $\gamma_s = (1 - v_s^2/c^2)^{-1/2}$ is the Lorentz factor. This modifies the cyclotron frequency to $\Omega_{cs} \to \Omega_{cs}/\gamma_s$. This correction will be explicitly specified when required. Starting from here and following [27], the matrix in (3.10) can be inverted in order to isolate $\mathbf{v}_{s1}$. Then, by using $\mathbf{j}_s = n_s q_s \mathbf{v}_{s1}$ and summing over species, we obtain a

characterisation of the conductivity tensor. Substituting this result into Eq. (3.4) leads directly to the standard cold-plasma dielectric tensor [27]:

$$\boldsymbol{\epsilon} = \begin{pmatrix} S & -iD & 0 \\ iD & S & 0 \\ 0 & 0 & P \end{pmatrix}. \tag{3.11}$$

where

$$\begin{aligned} S &= \frac{1}{2}(R+L), \qquad D = \frac{1}{2}(R-L), \\ R &= 1 - \sum_s \frac{\omega_{ps}^2}{\omega(\omega+\Omega_{cs})}, \\ L &= 1 - \sum_s \frac{\omega_{ps}^2}{\omega(\omega-\Omega_{cs})}, \\ P &= 1 - \sum_s \frac{\omega_{ps}^2}{\omega^2}, \end{aligned} \tag{3.12}$$

are the so-called Stix parameters, and $\omega_{ps}^2 = (n_s q_s^2)/(\epsilon_0 m_s)$ is the plasma frequency for species s. The Stix parameters have a clear physical interpretation: the quantities R and L describe the response of the plasma to right-hand and left-hand circularly polarised waves, respectively. Because the sign of Ω_{cs} differs from species to species through their charge, the wave polarisation controls which species is predominantly affected by a given wave. The parameter P describes the response to an electric field parallel to the background magnetic field $\mathbf{B}_0$; in this direction particle motion is not constrained by the magnetic field, so the response is the same as in an unmagnetised plasma.

Now, let θ denote the angle between the wavevector $\mathbf{k}$ and the background magnetic field $\mathbf{B}_0$, and define the refractive index vector $\mathbf{N} = c\,\mathbf{k}/\omega$, with $N = \|\mathbf{N}\|$ and $k = \|\mathbf{k}\|$, so that $\mathbf{N} = (N_\perp, 0, N_\parallel) = (N\sin\theta,\ 0,\ N\cos\theta)$. Substituting these definitions together with (3.11) into Eq. (3.5) and inserting the result into Eq. (3.6), we obtain:

$$AN^4 - BN^2 + C = 0 \tag{3.13}$$

The coefficients A, B, and C are functions of the plasma parameters and the wave propagation angle θ:

$$A = S\sin^2\theta + P\cos^2\theta \tag{3.14}$$

$$B = RL\sin^2\theta + PS(1+\cos^2\theta) \tag{3.15}$$

$$C = PRL \tag{3.16}$$

where the identity $S^2 - D^2 = RL$ has been used. Equation (3.13) is the cold plasma dispersion relation. Through this relation, it is possible to identify the cut-off frequencies and the resonances, namely those characteristic points where wave propagation fundamentally changes: cut-offs mark the frequencies at which the refractive index becomes zero and the wave is reflected rather, while resonances correspond to frequencies where

the refractive index diverges and the wave energy is strongly absorbed by the plasma. Because electrons are much lighter than ions, their cyclotron frequency is correspondingly much higher, and waves in the electron–cyclotron range evolve on timescales to which the ions cannot respond. It is therefore appropriate to assume that the ions provide a static background while the wave dynamics is entirely governed by the electrons. Subsequently, the dispersion relation, named Appleton-Hartree equation, for the squared refractive index N^2 will be:

$$N^2(\omega,\theta) = 1 - \frac{X}{1 - \frac{1}{2}Y^2\frac{\sin^2\theta}{1-X} \pm \sqrt{\left(\frac{1}{2}Y^2\frac{\sin^2\theta}{1-X}\right)^2 + Y^2\cos^2\theta}}, \tag{3.17}$$

where $X = \omega_{pe}^2/\omega^2$ and $Y = \Omega_e/\omega$. The two signs in Eq. (3.17) correspond to the two propagation modes, commonly referred to as the ordinary (O) and extraordinary (X) modes.

Since toroidal symmetry implies an approximate conservation of the parallel refractive index $N_\parallel$ along a ray trajectory, it is natural to analyse propagation at fixed $N_\parallel$ while allowing the perpendicular refractive index $N_\perp$ to vary with position. Cutoffs and resonances are then identified through the limiting values of $N_\perp$: a cutoff occurs when $N_\perp^2 \to 0$, while a resonance corresponds to $N_\perp^2 \to \infty$.

Specialising the cold–plasma dispersion relation to the ordinary and extraordinary branches, and expressing the result in terms of $N_\parallel$, one finds the following cutoff conditions:

$$\text{O-mode cutoff:} \quad \omega = \omega_{pe}, \tag{3.18}$$

$$\text{X-mode cutoffs:} \quad \omega_\pm = \frac{\Omega_{ce}}{2}\left(\pm 1 + \sqrt{1 + 4\,\frac{\omega_{pe}^2}{\Omega_{ce}^2}\,(1 - N_\parallel^2)}\right). \tag{3.19}$$

The X-mode has two cutoffs, namely the right-hand cutoff (ω_+), and a left hand cut-off (ω_-), and, as shown in Fig. 3.1, is split into two branches by an evanescent region between the right hand cut-off and the Upper-Hybrid resonance, given by [30]:

$$\omega_{\mathrm{UH}} \;=\; \sqrt{\omega_{pe}^2 + \Omega_e^2}, \tag{3.20}$$

The O- and X-modes also differ in their polarization properties. For strictly perpendicular propagation, $\theta = \angle(\mathbf{k}, \mathbf{B}_0) = \pi/2$, the electric field of the O-mode is parallel to $\mathbf{B}_0$, whereas the X-mode has its electric field perpendicular to $\mathbf{B}_0$.

3.2.1 Wave Absorption

Electron–cyclotron waves are absorbed primarily through cyclotron Landau damping in the vicinity of the electron cyclotron resonance and its harmonics. The condition for resonant interaction at the n-th harmonic, including the relativistic Doppler shift, can be written as [31]:

$$\omega = \frac{n\,\Omega_e}{\gamma} + k_\parallel\, v_{\parallel,\mathrm{res}}, \tag{3.21}$$

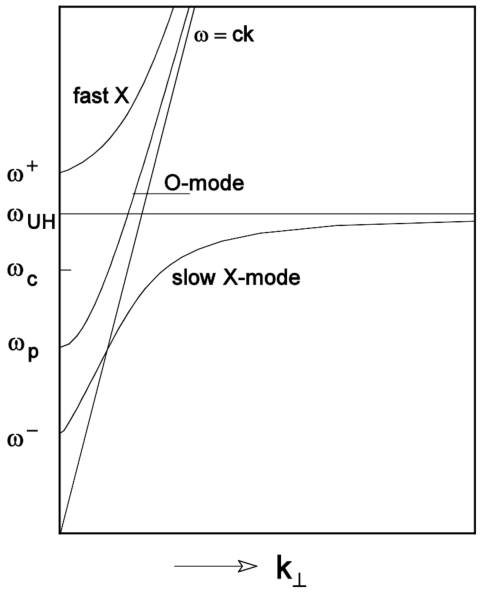

Figure 3.1: Dispersion curves for high frequency waves in dense plasmas. Adapted from [30].

where ω is the wave frequency, n is an integer harmonic number, $k_\parallel$ is the component of the wavevector parallel to $\mathbf{B}_0$, $v_{\parallel,\mathrm{res}}$ is the resonant parallel electron velocity, and $\gamma = (1 - v^2/c^2)^{-1/2}$ is the relativistic Lorentz factor. When this condition is satisfied, the wave can efficiently exchange energy with the electrons, resulting in a strong absorption of energy by the latter. In relativistic conditions, this constraint implies that resonant particles lie on *elliptic* curves in the $(v_\parallel, v_\perp)$ space [31]. Under the weakly relativistic limit, a convenient form for this ellipse is:

$$v_\perp^2 = c^2 \left(1 - \frac{\omega^2}{n^2\Omega_e^2}\right) + 2\,\frac{\omega^2 c N_\parallel}{n^2\Omega_e^2}\,v_\parallel - \left(1 + \frac{\omega^2 N_\parallel^2}{n^2\Omega_e^2}\right) v_\parallel^2, \tag{3.22}$$

where $N_\parallel$ is the refractive index along the magnetic field. The EC power is thus absorbed by electrons located on these resonant ellipses in velocity space. In the non–relativistic limit, $\gamma \to 1$, Eq. (3.21) reduces to the condition of constant $v_\parallel$, so the resonance is represented by a straight vertical line in velocity space.

The interaction between an electron and an EC wave leads to a stochastic sequence of small kicks in momentum space $(\delta p_\perp, \delta p_\parallel)$ which, when averaged over an ensemble of electrons with random gyrophase, can be interpreted as a diffusion process in momentum space. An important question is along which direction this diffusion proceeds predominantly. To address this, one starts from the relativistic energy–momentum relation for an electron,

$$W^2 = p^2c^2 + m_0^2c^4, \tag{3.23}$$

where W is the total energy, p the magnitude of the momentum, c the speed of light, and m_0 the rest mass. Changes in energy and momentum can be related, starting from

Eq. (3.23) and remembering that $W = \gamma m_0 c^2$, $p = \gamma m_0 v$, as

$$\delta W = \mathbf{v} \cdot \delta \mathbf{p} = v_\perp \, \delta p_\perp + v_\parallel \, \delta p_\parallel, \tag{3.24}$$

where $v_\perp$ and $v_\parallel$ are, respectively, the perpendicular and parallel components of the electron velocity, and $\delta p_\perp$, $\delta p_\parallel$ the corresponding momentum variations.

On the other hand, the energy and momentum exchanged between the electron and a single photon of the EC wave are constrained by the quantum mechanical relations

$$\delta W = \hbar \omega, \qquad \delta p_\parallel = \hbar k_\parallel, \tag{3.25}$$

where ω is the wave frequency and $k_\parallel$ the parallel wavenumber. Inserting Eq. (3.25) into Eq. (3.24) yields

$$\hbar \omega = v_\perp \, \delta p_\perp + v_\parallel \, \hbar k_\parallel, \tag{3.26}$$

which can be solved for $\delta p_\perp$ and normalised by $\delta p_\parallel = \hbar k_\parallel$. One obtains:

$$\frac{\delta p_\perp}{\delta p_\parallel} = \left(\frac{\omega}{k_\parallel v_\parallel} - 1 \right) \frac{v_\parallel}{v_\perp}. \tag{3.27}$$

The quantity in parentheses can be expressed in terms of the parallel phase velocity of the wave, $v_{\mathrm{ph},\parallel} = \omega / k_\parallel$, as

$$\frac{\omega}{k_\parallel v_\parallel} = \frac{v_{\mathrm{ph},\parallel}}{v_\parallel}. \tag{3.28}$$

Since for EC waves the parallel phase velocity is typically much larger than the speed of light [31], $v_{\mathrm{ph},\parallel} \gg c$, the factor $\omega / (k_\parallel v_\parallel)$ is large for almost all relevant regions of velocity space (with the exception of points very close to $v_\parallel \approx 0$). Hence

$$\left| \frac{\delta p_\perp}{\delta p_\parallel} \right| \gg 1. \tag{3.29}$$

The EC–induced momentum kicks therefore point predominantly in the perpendicular direction: the diffusion in velocity space is mainly *perpendicular*. This conclusion admits a transparent physical interpretation. The wave's magnetic field interacts with the particle through the Lorentz force $q \, \mathbf{v} \times \mathbf{B}_{\mathrm{wave}}$, which is always perpendicular to the velocity and therefore does not change the total kinetic energy. However, it is effective at rotating the velocity vector, converting parallel into perpendicular motion and vice versa. As a result, for O– and X–mode EC waves the diffusion of electrons in velocity space proceeds primarily in the perpendicular direction [31, 32].

3.2.2 Electron Cyclotron Current Drive Mechanisms

To drive a net current in a toroidal plasma, electron cyclotron waves must deposit their power in an asymmetric way in velocity space. In particular, efficient current drive requires that the EC waves be severely damped on electrons whose parallel velocity has predominantly one sign (either $v_\parallel > 0$ or $v_\parallel < 0$). Under these conditions, the EC interaction modifies the electron distribution function in a way that is not symmetric with respect

to $v_\parallel$, and a net parallel current results. Two distinct physical mechanisms contribute to this process: the Fisch–Boozer effect and the Ohkawa effect.

The first mechanism, originally identified by Fisch and Boozer [33], acts on electrons whose parallel velocity has the same sign as the phase velocity of the EC wave. As discussed in the previous section, the quasilinear EC diffusion for O– and X–modes proceeds predominantly in the perpendicular direction. For electrons with, say, $v_\parallel > 0$, the EC wave therefore tends to increase $v_\perp$ much more strongly than $v_\parallel$. In velocity space, this corresponds to an excursion from a sub-thermal region to supra-thermal perpendicular velocities. Because the collisionality decreases roughly as v^{-3}, electrons that are pushed to higher energies experience significantly lower collision frequencies. As a result, the EC diffusion creates a *hole* at sub-thermal $v_\perp$ and a *bulge* at supra-thermal $v_\perp$ for the selected sign of $v_\parallel$. Collisional relaxation, driven mainly by pitch-angle scattering [31], tends to refill the sub-thermal hole more rapidly than it reduces the supra-thermal bulge, owing to the higher collisionality at low energies. This imbalance in the filling and emptying rates of the distorted distribution produces a net parallel momentum and thus a driven current in the toroidal direction.

The second mechanism, originally proposed by Ohkawa [34], becomes important in regions of the tokamak where the trapped–particle population is largest, notably on the low–field side. In these regions, the velocity–space domain is naturally divided into passing and trapped particles. The EC wave can induce excursions in velocity space that transport electrons from passing to trapped orbits. When a passing electron is pushed into the trapped region, its contribution to the parallel current is effectively removed, i.e. its parallel momentum no longer contributes to the net current.

Collisions, however, can drive the opposite process: trapped electrons can be spontaneously detrapped back into passing orbits. This detrapping is approximately symmetric with respect to $v_\parallel$, in the sense that collisions repopulate passing states with both positive and negative $v_\parallel$ in a nearly symmetric way. The EC wave–particle interaction, in contrast, is sensitive to the sign of $v_\parallel$, since the wave is absorbed predominantly by electrons whose parallel velocity matches the wave phase velocity. As a consequence, the EC interaction preferentially transfers passing electrons of one sign of $v_\parallel$ into the trapped region, while collisions return trapped electrons to passing orbits more symmetrically in $v_\parallel$. The combined effect of these two processes is a net surplus of passing electrons with the *opposite* sign of $v_\parallel$ compared to the direction in which the wave is predominantly absorbed. This surplus produces a current contribution of opposite sign to the Fisch–Boozer current, and localised in the regions where the trapped–particle fraction is highest. In other words, the Ohkawa mechanism tends to drive a current in the opposite toroidal direction to the Fisch–Boozer current.

Chapter 4

The Gyrokinetic Turbulence Code GENE

The Gyrokinetic Electromagnetic Numerical Experiment (GENE) code is a gyrokinetic plasma turbulence code used for nuclear fusion and astrophysical scenarios [35, 21].

GENE is designed to solve the nonlinear gyrokinetic Vlasov–Maxwell system in five-dimensional phase space. It can be operated in linear mode, to compute growth rates and mode structures of the underlying microinstabilities (ITG, TEM, ETG, etc.), or in nonlinear mode, to simulate fully developed turbulence and the associated heat, particle, and momentum fluxes.

GENE is an Eulerian code that evolves the perturbed distribution function δf on a fixed grid in phase space, where the operators are discretised using the method of lines. Perpendicular to the magnetic field, GENE employs a spectral representation in (k_x, k_y), which allows derivatives along x and y directions to be computed as simple multiplications, while along the field line, the coordinate z is discretised on a grid with finite-difference schemes for derivatives and trapezoidal integration for parallel averages. The velocity space integration relies on a modified trapezoid rule in the $v_\parallel$ direction, and Gauss-Legendre for the μ direction [21].

Temporal evolution is typically performed with a fourth-order explicit Runge–Kutta scheme[36].

4.1 Normalisation and Observables in GENE

In order to solve the gyrokinetic equations, GENE formulates all quantities in dimensionless form based on a set of user-defined reference values [21]. This section introduces the framework adopted by GENE and discusses the macroscopic physical observables that can be extracted from its outputs, such as particle, momentum, and heat fluxes.

4.1.1 Normalisation

The code relies on reference values for length L_{ref}[m], temperature T_{ref}[eV], density n_{ref}[m^{-3}], magnetic field B_{ref}[T] and mass m_{ref}[kg]. From these, auxiliary quantities such as the reference thermal speed, gyrofrequency and Larmor radius are respectively defined as

$$c_{\mathrm{ref}} = \sqrt{\frac{T_{\mathrm{ref}}}{m_{\mathrm{ref}}}}, \qquad \Omega_{\mathrm{ref}} = \frac{eB_{\mathrm{ref}}}{m_{\mathrm{ref}}c}, \qquad \rho = \frac{c_{\mathrm{ref}}}{\Omega_{\mathrm{ref}}}, \tag{4.1}$$

and the dimensionless ordering parameter is often written as $\rho^*_{\mathrm{ref}} = \rho_{\mathrm{ref}}/L_{\mathrm{ref}}$. Using these reference quantities, the phase-space coordinates are normalised according to

$$x = \rho_{\mathrm{ref}}\,\hat{x}, \quad y = \rho_{\mathrm{ref}}\,\hat{y}, \quad z = \hat{z}, \tag{4.2}$$

$$t = \frac{L_{\mathrm{ref}}}{c_{\mathrm{ref}}}\,\hat{t}, \qquad v_{\parallel} = c_{\mathrm{ref}}\,\hat{v}_T\hat{v}_{\parallel}, \qquad \mu = \frac{T_{\mathrm{ref}}}{B_{\mathrm{ref}}}\hat{T}_0\hat{\mu},$$

where hats denote the dimensionless variables used internally by GENE. Similarly, background profiles and species (denoted by $j = e, i$) parameters are expressed as

$$n_{j0} = n_{\mathrm{ref}}\,\hat{n}_{j0}, \qquad T_{j0} = T_{\mathrm{ref}}\,\hat{T}_{j0}, \qquad m_j = m_{\mathrm{ref}}\,\hat{m}_j, \tag{4.3}$$

$$q_j = e\,\hat{q}_j, \qquad \hat{v}_{jT} = \sqrt{2\hat{T}_{j0}/\hat{m}_j},$$

and the normalised gradients are

$$\omega_{n,j} = -\frac{L_{\mathrm{ref}}}{n_{\mathrm{ref}}}\frac{\mathrm{d}n_{j0}}{\mathrm{d}x}, \qquad \omega_{T,j} = -\frac{L_{\mathrm{ref}}}{T_{\mathrm{ref}}}\frac{\mathrm{d}T_{j0}}{\mathrm{d}x}, \qquad \nabla\boldsymbol{B} \;=\; \frac{L_{\mathrm{ref}}}{B_{\mathrm{ref}}}\,\nabla\hat{\boldsymbol{B}}. \tag{4.4}$$

The gyrokinetic distribution function is split into an equilibrium part f_{j0} and a perturbed part. GENE evolves the modified perturbation g_j, which is normalised as

$$g_j = \frac{\rho_{\mathrm{ref}}}{L_{\mathrm{ref}}}\,\frac{n_{\mathrm{ref}}}{c^3_{\mathrm{ref}}}\,\frac{\hat{n}_{j0}}{\hat{v}^3_T}\,\hat{g}_j, \tag{4.5}$$

so that perturbed quantities are naturally ordered with $\rho_{\mathrm{ref}}/L_{\mathrm{ref}}$ and remain of order unity in typical simulations. The electrostatic potential and the possible sources are normalised as

$$\phi = \frac{\rho_{\mathrm{ref}}}{L_{\mathrm{ref}}}\,\frac{T_{\mathrm{ref}}}{e}\,\hat{\phi}, \qquad C(f) \;=\; \frac{\rho_{\mathrm{ref}}}{L^2_{\mathrm{ref}}}\,\frac{n_{\mathrm{ref}}}{c^2_{\mathrm{ref}}}\,\frac{\hat{n}_0}{\hat{v}^3_T}\,\hat{C}(f). \tag{4.6}$$

and analogous normalisations are used for the electromagnetic potentials.

The reference values are often taken as $\rho_{\mathrm{ref}} = \rho_s$ and $c_{\mathrm{ref}} = c_s$, with the ion mass chosen as the reference mass ($m_{\mathrm{ref}} = m_i$) and the electron temperature as the reference temperature ($T_{\mathrm{ref}} = T_{e0}$).

4.1.2 Observables

Although GENE advances the full five-dimensional distribution function $g_j(k_x, k_y, z, v_\parallel, \mu)$ in time, most physical conclusions are drawn from quantities obtained by suitable moments and averages. In particular, for nonlinear simulations, the code provides volume-averaged radial particle and heat fluxes for each species. These are defined as

$$\langle \Gamma_j \rangle = \langle n_{1,j}\, \mathbf{v}_{E,j} \cdot \mathbf{x} \rangle\,, \qquad \langle Q_j \rangle = \langle p_{1,j}\, \mathbf{v}_{\chi,j} \cdot \mathbf{x} \rangle\,, \tag{4.7}$$

where $n_{1,j}$ and $p_{1,j}$ denote the perturbed density and pressure, $\mathbf{v}_{\chi_j} = \mathbf{B} \times \nabla \chi_j / B^2$ is the ExB drift velocity associated with the total potential χ_j for species j, and $\langle \cdots \rangle$ denotes an average over the simulation domain. Because the potential includes both electrostatic and electromagnetic contributions, these fluxes can be decomposed into electrostatic and electromagnetic parts

$$\langle \Gamma_j \rangle = \langle \Gamma_j^{\mathrm{es}} \rangle + \langle \Gamma_j^{\mathrm{em}} \rangle, \qquad \langle Q_j \rangle = \langle Q_j^{\mathrm{es}} \rangle + \langle Q_j^{\mathrm{em}} \rangle, \tag{4.8}$$

which is particularly useful when assessing the relative importance of electrostatic and magnetic fluctuations for cross-field transport.

4.2 Gyrokinetic Implementation of the ECCD Model

The effect of electron cyclotron (EC) deposition can be included in a gyrokinetic framework by means of a quasilinear source term added to the gyrokinetic equation. We start from the constant deposition case, closely following the derivations presented in Refs. [37, 19], where the diffusion operator is reduced to a tractable source in the five-dimensional phase space $(x, y, z, v_\parallel, \mu)$, where the interaction between the EC waves and electrons is represented by a quasilinear operator [38]:

$$Q_{\mathrm{EC}}[f_{\mathrm{e}}] = \frac{\partial}{\partial \mathbf{v}} \cdot \mathbf{D}_{\mathrm{EC}} \cdot \frac{\partial f_{\mathrm{e}}}{\partial \mathbf{v}}, \tag{4.9}$$

where f_{e} is the electron distribution function and $\mathbf{D}_{\mathrm{EC}}$ is the velocity-space quasilinear diffusion operator. For O-mode waves in large tokamaks like ITER, $\mathbf{D}_{\mathrm{EC}}$ can be written, under the non-relativistic approximation, as [38, 32, 39]

$$\mathbf{D}_{\mathrm{EC}} \;\approx\; D\, \delta\!\left(v_\parallel - v_{\parallel,\mathrm{res}}\right) \mathbf{v}_\perp \otimes \mathbf{v}_\perp, \tag{4.10}$$

where $v_{\parallel,\mathrm{res}}$ is the parallel velocity of the resonant electrons

$$v_{\parallel,\mathrm{res}} \;=\; \frac{\omega - n\Omega_{\mathrm{e}}}{k_\parallel}, \tag{4.11}$$

with ω the wave frequency, n the harmonic, Ω_{e} the electron cyclotron frequency and $k_\parallel$ the parallel wavenumber.
Now, for numerical reasons and to account for the finite spectral width of the EC beam, the Dirac delta is replaced by a Gaussian of width $\Delta v_\parallel$ in parallel velocity. Thus, assuming further that the background electrons follow a Maxwellian distribution f_{e0}, and

substituting into Eq. (4.9), we find

$$Q_{\mathrm{EC}} \;=\; D\,\frac{1}{\sqrt{2\pi}\,\Delta v_{\parallel}}\,\exp\!\left[-\frac{(v_{\parallel}-v_{\parallel,\mathrm{res}})^2}{2\Delta v_{\parallel}^2}\right]\left(\frac{v_{\perp}^2}{v_T^2}-1\right)\exp\!\left[-\frac{v_{\parallel}^2+v_{\perp}^2}{v_T^2}\right], \tag{4.12}$$

where v_T is the electron thermal speed and D is a quasilinear diffusion coefficient.

The D coefficient can be characterised by requiring that the second velocity moment of the source Q_{EC} is equal to the prescribed deposited power density [37], i.e.

$$\int \mathrm{d}^3v\;\frac{m_{\mathrm{e}}v^2}{2}\,Q_{\mathrm{EC}} \;=\; p_{\mathrm{EC}}. \tag{4.13}$$

Carrying out this integration yields (using $dv_x dv_y dv_z = v_\perp dv_\parallel dv_\perp d\theta$) an expression for Q_{EC} where the p_{EC} dependence is explicit.

Following the procedure illustrated in [37], a Gaussian envelope in (k_y, k_y) space is then introduced to provide a spatial characterisation of the deposition. Subsequently, the expression is normalised in GENE units, yielding:

$$\begin{aligned}\hat{Q}_{\mathrm{EC}}(\hat{k}_x,\hat{k}_y,\hat{z},\hat{v}_\parallel,\hat{\mu}) = \frac{2\hat{p}_{\mathrm{EC}}}{\pi^2\hat{m}_e\hat{\sigma}_\parallel\hat{\sigma}_z}\exp\left[-\frac{\left(\hat{v}_\parallel-\dfrac{\hat{v}_{\parallel,\mathrm{res}}}{2\Delta\hat{v}_\parallel^2+1}\right)^2}{2\hat{\sigma}_\parallel^2}\right]\left(\hat{\mu}\hat{B}-1\right)\\ \cdot\exp\left[-\hat{\mu}\hat{B}\right]\exp\left[-\frac{(\hat{z}-\hat{z}_{\mathrm{EC}})^2}{2\hat{\sigma}_z^2}\right]\\ \cdot\exp\left[-\frac{\sigma_\perp^2(g^{xx}\hat{k}_x^2+2g^{xy}\hat{k}_x\hat{k}_y+g^{yy}\hat{k}_y^2)}{2}\right]\\ \cdot\exp\left[-i\left(g^{xx}\hat{k}_x\hat{x}_{\mathrm{EC}}+g^{yy}\hat{k}_y\hat{y}_{\mathrm{EC}}\right)\right].\end{aligned} \tag{4.14}$$

where we assumed that $\hat{\sigma}_x = \hat{\sigma}_y = \hat{\sigma}_\perp$ (so that the deposition is a circular Gaussian centered at the outer midplane), and g^{ij} are the metric tensor components, that in $\hat{s}$-α geometry with $\alpha = 0$ read: $g^{xx} = 1, g^{yy} = 1 + (\hat{s}\hat{z})^2$, $g^{xy} = \hat{s}\hat{z}$, and $\hat{\sigma}_\parallel = \sqrt{(\Delta\hat{v}_\parallel^2/(1+2\Delta\hat{v}_\parallel^2)}$, where $\Delta\hat{v}_\parallel$ has been normalised with the the electron thermal velocity v_{eT}.

This defines the (time-independent) source term implemented in GENE that accounts for the effect of electron cyclotron deposition on the perturbed distribution function. The time modulation is introduced through

$$f_{\mathrm{mod}}(\hat{t}) = \sin\,(\omega_0(\hat{t}-\hat{t}_0), \tag{4.15}$$

where $\omega_0 = 2\pi/f_0$, and f_0 is the modulation frequency, so that the modulated source term becomes

$$\hat{Q}_{\mathrm{EC,mod}}(\hat{t}) = \hat{Q}_{\mathrm{EC}}\,f_{\mathrm{mod}}(\hat{t}). \tag{4.16}$$

To express the EC source term in GENE units, the following normalisation factors are introduced: heat–flux density Q_{ref} is defined as [37]

$$Q_{\mathrm{ref}} = \frac{\rho_{\mathrm{s}}}{R_0^2}\frac{n_{e0}}{c_s^2}\frac{\hat{n}_{\mathrm{e}}}{\hat{v}_T^3}, \tag{4.17}$$

and the corresponding reference power density is

$$p_{\mathrm{ref}} = \frac{n_{\mathrm{e}0}\rho_s m_i}{R_0^2}\left(\frac{k_B T_{e0}}{m_{\mathrm{i}}}\right)^{3/2}\frac{2\hat{n}_e\hat{T}_e}{\hat{m}_e}. \tag{4.18}$$

Here, ρ_{s}, R_0, $n_{\mathrm{e}0}$, c_{s}, m_{i}, and $T_{\mathrm{e}0}$ are the reference quantities, while hatted variables denote the corresponding dimensionless GENE-normalised quantities.

As we have seen, the effect of electron–cyclotron heating and current drive enters the gyrokinetic equation through the source term $\hat{Q}_{\mathrm{EC}}$ in phase space, which is implemented in GENE in Fourier space. To illustrate its shape in real space, in the following argument we restrict to the outboard midplane, $\hat{z}=0$. For the $\hat{s}$–α geometry used here, the metric components at the outboard midplane are $\hat{g}^{xx}=1$, $\hat{g}^{yy}=1$, and $\hat{g}^{xy}=0$. Evaluating Eq. (4.2) at $\hat{z}=0$ and taking the inverse Fourier transform in $\hat{k}_x, \hat{k}_y$ gives

$$\begin{aligned}
\hat{Q}_{\mathrm{EC}}(\hat{x},\hat{y},\hat{z}=0,\hat{v}_\parallel,\hat{\mu}) &= \frac{1}{(2\pi)^2}\int_{-\infty}^{\infty}d\hat{k}_x\int_{-\infty}^{\infty}d\hat{k}_y\,\hat{Q}_{\mathrm{EC}}(\hat{k}_x,\hat{k}_y,\hat{z}=0,\hat{v}_\parallel,\hat{\mu})e^{i(\hat{k}_x\hat{x}+\hat{k}_y\hat{y})}\\
&= \frac{2\,\hat{p}_{\mathrm{EC}}}{\pi^2\,\hat{m}_e\,\hat{\sigma}_\parallel\,\hat{\sigma}_z}\exp\left[-\frac{\left(\hat{v}_\parallel-\dfrac{\hat{v}_{\parallel,\mathrm{res}}}{2\,\Delta\hat{v}_\parallel^2+1}\right)^2}{2\,\hat{\sigma}_\parallel^2}\right](\hat{\mu}\,\hat{B}-1)\,\exp\Big[-\hat{\mu}\,\hat{B}\Big]\\
&\quad\cdot\exp\left[-\frac{(\hat{z}_{\mathrm{EC}})^2}{2\,\hat{\sigma}_z^2}\right]\\
&\quad\cdot\frac{1}{(2\pi)^2}\int_{-\infty}^{\infty}d\hat{k}_x\int_{-\infty}^{\infty}d\hat{k}_y\,\exp\left[-\frac{\hat{\sigma}_\perp^2}{2}(\hat{k}_x^2+\hat{k}_y^2)\right]e^{\,i(\hat{k}_x\Delta\hat{x}+\hat{k}_y\Delta\hat{y})},
\end{aligned} \tag{4.19}$$

where $\Delta\hat{x}=\hat{x}-\hat{x}_{\mathrm{EC}}$, $\Delta\hat{y}=\hat{y}-\hat{y}_{\mathrm{EC}}$.

Introducing the vectors $\hat{\mathbf{k}}_\perp=(\hat{k}_x,\hat{k}_y)^T$, $(\boldsymbol{\Delta\hat{\mathbf{x}}}=\Delta\hat{x},\Delta\hat{y})^T$, and the perpendicular covariance matrix $\hat{\boldsymbol{\Sigma}}_\perp=\hat{\sigma}_\perp^2\begin{pmatrix}1&0\\0&1\end{pmatrix}$, the exponent in the integral can be written as $\hat{\sigma}_\perp^2(\hat{k}_x^2+\hat{k}_y^2)=\hat{\mathbf{k}}_\perp^{\mathrm{T}}\hat{\boldsymbol{\Sigma}}_\perp\,\hat{\mathbf{k}}_\perp$, so that:

$$\begin{aligned}
&\frac{1}{(2\pi)^2}\int_{-\infty}^{\infty}d\hat{k}_x\int_{-\infty}^{\infty}d\hat{k}_y\,\exp\left[-\frac{\hat{\sigma}_\perp^2}{2}(\hat{k}_x^2+\hat{k}_y^2)\right]e^{\,i(\hat{k}_x\Delta\hat{x}+\hat{k}_y\Delta\hat{y})}\\
&\quad=\frac{1}{(2\pi)^2}\int_{\mathbb{R}^2}d\hat{\mathbf{k}}\,\exp\left[-\frac{1}{2}\hat{\mathbf{k}}_\perp^{\mathrm{T}}\hat{\boldsymbol{\Sigma}}_\perp\,\hat{\mathbf{k}}_\perp+i\,\hat{\mathbf{k}}_\perp^{\mathrm{T}}\boldsymbol{\Delta\hat{\mathbf{x}}}\right]\\
&\quad=\frac{1}{2\pi\sqrt{\det\hat{\boldsymbol{\Sigma}}_\perp}}\exp\left[-\frac{1}{2}\boldsymbol{\Delta\hat{\mathbf{x}}}^{\mathrm{T}}\hat{\boldsymbol{\Sigma}}_\perp^{-1}\boldsymbol{\Delta\hat{\mathbf{x}}}\right]\\
&\quad=\frac{1}{2\pi\hat{\sigma}_\perp^2}\,\exp\left[-\frac{(\hat{x}-\hat{x}_{\mathrm{EC}})^2+(\hat{y}-\hat{y}_{\mathrm{EC}})^2}{2\hat{\sigma}_\perp^2}\right].
\end{aligned}$$

where the transition from the first to the second equality relies on a standard result for multivariate Gaussian integration [40].

Therefore, at the outboard midplane the EC source term can be written as

$$\hat{Q}_{\mathrm{EC}}(\hat{x},\hat{y},\hat{z}{=}0,\hat{v}_\parallel,\hat{\mu}) = \frac{2\hat{p}_{\mathrm{EC}}}{\pi^2\,\hat{m}_e\,\hat{\sigma}_z\,\hat{\sigma}_\parallel} F_v(\hat{v}_\parallel,\hat{\mu})\,\exp\left[-\frac{(\hat{z}_{\mathrm{EC}})^2}{2\,\hat{\sigma}_z^2}\right] \cdot \frac{1}{2\pi\hat{\sigma}_\perp^2}\exp\left[-\frac{(\hat{x}-\hat{x}_{\mathrm{EC}})^2+(\hat{y}-\hat{y}_{\mathrm{EC}})^2}{2\,\hat{\sigma}_\perp^2}\right]. \tag{4.20}$$

where

$$F_v(\hat{v}_\parallel,\hat{\mu}) = \exp\left[-\frac{\left(\hat{v}_\parallel - \dfrac{\hat{v}_{\parallel,\mathrm{res}}}{2\,\Delta\hat{v}_\parallel^2+1}\right)^2}{2\,\hat{\sigma}_\parallel^2}\right](\hat{\mu}\,\hat{B}-1)\,\exp\left[-\hat{\mu}\,\hat{B}\right],$$

If we now evaluate the second velocity moment of the source term $\hat{Q}_{\mathrm{EC}}$ in Eq. (4.20), we obtain the real–space form of the EC deposition profile at $\hat{z}=0$.

$$\hat{S}_{\mathrm{EC}}(\hat{x},\hat{y},\hat{z}=0) = \hat{p}_{\mathrm{EC}}\frac{1}{\sqrt{2\pi}\,\hat{\sigma}_z}\,\exp\left[-\frac{(\hat{z}_{\mathrm{EC}})^2}{2\,\hat{\sigma}_z^2}\right] \cdot \frac{1}{2\pi\hat{\sigma_\perp}^2}\exp\left[-\frac{(\hat{x}-\hat{x}_{\mathrm{EC}})^2+(\hat{y}-\hat{y}_{\mathrm{EC}})^2}{2\,\hat{\sigma}_\perp^2}\right]. \tag{4.21}$$

We can see from this expression that in the outboard midplane, the deposition profile has a circular gaussian shape in the perpendicular plane. The calculations for the general form of the (time-independent) spatial profile of $\hat{S}_{EC}$ are analogous to the previous ones and lead to:

$$\hat{S}_{\mathrm{EC}}(\hat{x},\hat{y},\hat{z}) = \frac{\hat{p}_{\mathrm{EC}}}{(2\pi)^{3/2}\,\hat{\sigma}_z\,\hat{\sigma}_\perp^2}\,\exp\left[-\frac{(\hat{z}-\hat{z}_{\mathrm{EC}})^2}{2\,\hat{\sigma}_z^2}\right]\exp\left[-\frac{1}{2}\,\boldsymbol{\Delta\hat{\mathbf{x}}}^{\mathrm{T}}\boldsymbol{\Sigma}_\perp^{-1}(\hat{z})\,\boldsymbol{\Delta\hat{\mathbf{x}}}\right], \tag{4.22}$$

where

$$\boldsymbol{\Delta\hat{\mathbf{x}}} = \begin{pmatrix}\hat{x}-\hat{x}_{\mathrm{EC}}\\ \hat{y}-\hat{y}_{\mathrm{EC}}\end{pmatrix}, \qquad \boldsymbol{\Sigma}_\perp(\hat{z}) = \hat{\sigma}_\perp^2\begin{pmatrix}g^{xx} & g^{xy}\\ g^{xy} & g^{yy}\end{pmatrix}.$$

In this case, we observe that away from the outboard midplane, the perpendicular Gaussian acquires an elliptic shape because the covariance matrix is not diagonal anymore, since $g^{ij}(\hat{z}) \neq 0$. This reflects the physical properties of magnetic shear.

From the standpoint of Gaussian normalisation, however, this does not affect the result, since in $\hat{s}$–α geometry one has

$$\det\begin{pmatrix}g^{xx} & g^{xy}\\ g^{yx} & g^{yy}\end{pmatrix} = 1,$$

so integration over $\hat{x},\hat{y}$ still yields unity for all $\hat{z}$.

Finally, the profile of the time-dependent power deposition will be given by:

$$\hat{S}_{\mathrm{EC},mod}(\hat{x},\hat{y},\hat{z},t) = \hat{S}_{\mathrm{EC}}(\hat{x},\hat{y},\hat{z}) f_{\mathrm{mod}}(\hat{t}). \tag{4.23}$$

For notational simplicity, the hats on dimensionless quantities will be omitted from this point forward.

Chapter 5

Perturbative Analysis and Heat Transport Modelling

The goal of this chapter is to introduce the perturbative analysis framework that often is employed for modeling heat transport as an advection-diffusion process. The idea is to impose a time-varying modulation of the Electron Cyclotron Resonance Heating (ECRH) power, thereby generating a periodic temperature response throughout the plasma. Each point in space experiences a small, oscillatory perturbation of the background temperature. By measuring the amplitude and phase of this temperature modulation at different radial positions, we can infer the plasma's frequency response and, consequently, estimate the heat transport coefficients.

5.1 System Frequency Response Analysis

We model the plasma response at each spatial location x as a linear time–invariant (LTI) system.[1] Although the numerical implementations are ultimately carried out on discretised quantities, a continuous formalism is adopted in order to present the underlying ideas in a clearer way.

5.1.1 Frequency Response Function

In general, for a single–input single–output system, considering an input signal $u(t)$ and an output signal $y(x,t)$, with x fixed, under the linear time–invariant (LTI) assumption the following convolutional relation holds [41]

$$y(x,t) = (g(x,\cdot) * u)(t), \tag{5.1}$$

where $g(x,\cdot)$ is the impulse response at x. Taking the Fourier transform in time yields

$$Y(x,\omega) = G(x,\omega)\, U(\omega), \tag{5.2}$$

[1] This assumption requires further testing.

where $U(\omega)$ and $Y(x,\omega)$ denote the Fourier transforms of $u(t)$ and $y(x,t)$, and

$$G(x,\omega) = \mathcal{F}\{g(\cdot,x)\}(\omega) \tag{5.3}$$

is the frequency response function (FRF). Whenever $U(\omega) \neq 0$, the FRF can be computed as

$$G(x,\omega) = \frac{Y(x,\omega)}{U(\omega)}, \tag{5.4}$$

Since $G(x,\omega)$ is a complex number, it can be written in polar form as

$$G(x,\omega) = \left|G(x,\omega)\right| \mathrm{e}^{\,i\phi(x,\omega)}, \tag{5.5}$$

with gain $|G(x,\omega)|$ and phase $\phi(x,\omega) = \angle G(x,\omega)$.

In our system, the input is a scalar signal $u(t)$ representing the time-varying ECRH injection in a fixed point x_{EC}, and the output is the temperature $T_\perp(x,t)$ for each x. In particular, $T_\perp(x,t)$ is defined as follows. First, the perturbed temperature profile $T_{1\perp}$ is taken from the GENE simulation [42]:

$$T_{1\perp} = \frac{m}{2n_0} \int \mathrm{d}^3v \, v_\perp^2 \, f_1^{(pc)} - T_0 \frac{n_1}{n_0} \tag{5.6}$$

where f_1^{pc} is the *fluctuating* part of the particle distribution function, $T_{1\perp}$ and n_1 respectively denote the first-order perpendicular temperature perturbation and density, and n_0 is the background density. Then, $T_{1\perp}$ is averaged over the y and z directions, so that a temperature profile along the radial direction is obtained:

$$T_\perp(x,t) := \left\langle T_{1\perp}(x,y,z,t) \right\rangle_{y,z} \tag{5.7}$$

To remain consistent with the notation commonly adopted in the system identification literature, the Fourier transform of $T_\perp(x,t)$ will be denoted by $Y(x,\omega)$ in the following chapters.

The input signal $u(t)$ is given by

$$u(t) = u_A \, \sin\left(\omega_0(t - t_0)\right), \tag{5.8}$$

where $\omega_0 = 2\pi f_0$ is the ECRH modulation angular frequency and u_A is obtained taking the spatial profile $S_{EC}(x,y,z)$ from Eq. (4.22) and integrating it over x, y, z leads to

$$u_A = p_{EC} \tag{5.9}$$

This also coincides with the total injected power.

The LTI assumption serves as an approximation that allows us to focus on the system response occurring mainly at the same frequency as the deposition ω_0, and the FRF at this frequency therefore contains the plasma's linear dynamic response to the modulated heating.

In the analyses presented in this work, the signals are restricted to time windows that contain an integer number of modulation periods. This choice ensures the spectral content

of the signals is concentrated at the modulation frequency, without spurious contributions due to cutting the signal mid–cycle.

To obtain accurate estimates of the Fourier coefficients at the ECRH modulation frequency (and, where required, at its higher harmonics), the *Local Polynomial Method* (LPM) [43] is employed.

Within the LPM framework, the measured spectrum in a neighbourhood of the frequency of interest ω_0 is modelled as the sum of (i) a smooth contribution associated with transients and slow trends in the signal, and (ii) discrete spectral lines associated with the periodic excitation, plus stochastic noise. The smooth contribution is locally approximated by a complex-valued polynomial in frequency, whose coefficients are obtained by a weighted least-squares fit on a set of neighbouring frequency bins. Evaluating this polynomial at ω_0 yields an estimate of the transient contribution at that frequency, which is then subtracted from the raw spectrum. The result is an essentially unbiased estimate of the complex Fourier coefficient associated with the periodic part of the signal at ω_0. In addition, this method also allows estimating the variance directly from the residuals of the local polynomial fit.

In this work, the LPM is applied to the output signal $T_\perp(x,t)$ at each radial position x, yielding Fourier coefficients $Y_{\mathrm{LPM}}(x,\omega_0)$ and variances $\hat{\sigma}^2_{Y,\mathrm{LPM}}(x,\omega_0)$ at the modulation frequency. The estimated frequency response function is then defined as [44]

$$\hat{G}(x,\omega_0) \;=\; \frac{Y_{\mathrm{LPM}}(x,\omega_0)}{U(\omega_0)}. \tag{5.10}$$

Its (complex) variance can be approximated by

$$\hat{\sigma}^2_{\hat{G}}(x,\omega_0) \;\approx\; \frac{\hat{\sigma}^2_{Y,\mathrm{LPM}}(x,\omega_0)}{\left|U(\omega_0)\right|^2}. \tag{5.11}$$

This variance quantifies the uncertainty of the complex estimator $\hat{G}$ and can be used to construct, for instance, 2σ confidence bounds on the amplitude and phase of the FRF, under the assumption that the residual noise on $Y(x,\omega_0)$ after the LPM correction is zero–mean circular complex Gaussian.

5.1.2 Magnitude–Squared Coherence

In order to identify spatial regions where the local plasma response is well described by a linear relation between the ECRH drive and the temperature perturbation, it is useful to quantify how strongly the input signal $u(t)$ and the output $T_\perp(x,t)$ are linearly correlated at a given frequency. For this purpose the *magnitude–squared coherence* (MSC), which measures, at each frequency, the fraction of the output power that can be attributed to a linear time–invariant response to the input, is used. Consider the $u(t)$ and $T_\perp(x,t)$ signals. Their auto– and cross–correlation functions can be computed as [45]

$$R_{uu}(\tau) = \left\langle\, u(t)\, u(t-\tau)\,\right\rangle_t, \tag{5.12}$$

$$R_{T_\perp T_\perp}(x;\tau) = \left\langle\, T_\perp(x,t)\, T_\perp(x,t-\tau)\,\right\rangle_t, \tag{5.13}$$

$$R_{T_\perp u}(x;\tau) = \left\langle\, T_\perp(x,t)\, u(t-\tau)\,\right\rangle_t. \tag{5.14}$$

The corresponding spectral densities are defined as Fourier transforms of these correlation functions,

$$S_{uu}(\omega_0) = \mathcal{F}_\tau\{R_{uu}(\tau)\}(\omega_0), \tag{5.15}$$
$$S_{T_\perp T_\perp}(x;\omega_0) = \mathcal{F}_\tau\{R_{T_\perp T_\perp}(x;\tau)\}(\omega_0), \tag{5.16}$$
$$S_{T_\perp u}(x;\omega_0) = \mathcal{F}_\tau\{R_{T_\perp u}(x;\tau)\}(\omega_0), \tag{5.17}$$

where $\mathcal{F}_\tau\{\cdot\}$ denotes the Fourier transform with respect to the time lag τ.

The magnitude–squared coherence between $u(t)$ and $T_\perp(x,t)$ is then defined, for each position x at the modulation frequency ω_0, as

$$\gamma^2(x;\omega_0) \;=\; \frac{\left|S_{T_\perp u}(x;\omega_0)\right|^2}{S_{T_\perp T_\perp}(x;\omega_0)\, S_{uu}(\omega_0)}\,, \tag{5.18}$$

with $0 \le \gamma^2(x;\omega_0) \le 1$. By construction, $\gamma^2(x;\omega_0)$ represents the fraction of the output power spectral density $S_{T_\perp T_\perp}(x;\omega_0)$ that is *coherent*, i.e. linearly explainable, through a deterministic response to the input at frequency ω_0.

Values of γ^2 close to unity indicate that the local plasma response at the drive frequency is almost entirely described by a linear time–invariant model driven by the modulation signal, whereas a rapid decrease of $\gamma^2(x;\omega_0)$ marks regions where the output is dominated by components that are not linearly correlated with the input (such as turbulent fluctuations).

For the analysis of the simulation data, the longest contiguous spatial interval $[x_L^{\mathrm{coh}},\, x_R^{\mathrm{coh}}]$ is identified such that $\gamma^2(x;\omega_0)$ remains above a prescribed threshold. This interval will be referred to as the *high–coherence region*.

5.2 Linear Approach To Heat Transport Coefficients Estimation

This section presents a linear model for estimating the electron heat advection–diffusion (AD) transport coefficients, following the formulation in [46]. For notational convenience, in the following sections the electron perpendicular temperature $T_\perp$ is denoted by T, and the electron density by n.

In magnetically confined plasmas, parallel transport along the field lines is much faster than perpendicular transport. This, together with toroidal symmetry, implies that variations along the magnetic field lines are weak compared to those across magnetic flux surfaces: the fast parallel dynamics acts to homogenise quantities on each flux surface on very short time scales, so that the relevant heat transport is the radial one, dominated by radial gradients. As a result, on transport timescales the system can be modelled as an effectively one-dimensional process in the radial coordinate within a cylindrical geometry. The standard 1D cylindrical transport PDE with spatially dependent coefficients is [47]:

$$\frac{\partial}{\partial t}(\,nT) = \frac{1}{\rho}\frac{\partial}{\partial \rho}\Big(\rho\, n\chi(\rho)\,\frac{\partial T}{\partial \rho} + \rho\, nV(\rho)\,T\Big) \;+\; S_h, \tag{5.19}$$

where ρ is the radial coordinate, V collects effective advective contributions and S_h contains the power sources and sinks (e.g., ECRH deposition, ohmic heating power and bremsstrahlung radiation loss). In the context of the present analysis, the ECRH power deposition is modulated at frequencies that approach the characteristic turbulent time scales, that we can characterise looking at the temperature correlation time τ_c as shown in Sec. 6.1. These timescales are of the order of microseconds. In contrast, the characteristic time scale of macroscopic transport, identified with the (energy) confinement time τ_E, is of the order of seconds. Owing to this strong separation of time scales, the damping term τ^{-1} that is commonly included in transport models [46], is consistently omitted here.

For the same reason, it is also assumed that the periodically modulated electron heating $P_{\mathrm{mod}}(t)$ provides the dominant time dependence of the total heat source S_h. All other source and sink terms are taken to vary only slowly on the time scale of the modulation period and are therefore absorbed into the stationary background contribution [46].

For the following perturbative analysis we adopt these standard simplifications [46]: (i) focus on steady periodic response (transients neglected); (ii) analyse a source-excluded window where $P_{\mathrm{mod}} = 0$; (iii) take coefficients time and space independent across the analysis window; (iv) assume constant density over space and time ($\partial_\rho n = 0$, $\partial_t n = 0$). Under these hypotheses (5.19) reduces to

$$\frac{\partial T}{\partial t} = \chi \frac{1}{\rho}\frac{\partial}{\partial \rho}\Big(\rho \frac{\partial T}{\partial \rho}\Big) + V \frac{1}{\rho}\frac{\partial}{\partial \rho}\Big(\rho\, T\Big) \tag{5.20}$$

5.2.1 Slab Representation

A convenient working approximation — consistent with the local nature of the $\hat{s}$-α flux-tube model — is the slab formulation, in which the radial coordinate is treated as locally Cartesian.

$$\frac{\partial T}{\partial t} = \chi \frac{\partial^2 T}{\partial \rho^2} + V_s \frac{\partial T}{\partial \rho} \tag{5.21}$$

V_s is related to its cylindrical counterpart through the identity:

$$V_s \equiv V + \frac{\chi}{\rho}$$

so that over narrow windows (like in a flux-tube) where ρ^{-1} terms are negligible, $V_s \approx V$, while the diffusive term is unchanged by geometry. From now on, x will be used in place of ρ for clarity within the slab geometry framework.
Now, applying the Laplace transform to the previous energy balance PDE, it reduces to an ODE with respect to the space coordinate x:

$$\chi \frac{d^2\Theta(x,s)}{dx^2} + V \frac{d\Theta(x,s)}{dx} - s\,\Theta(x) = 0. \tag{5.22}$$

where $\Theta(x,s)$ is the Laplace transform of the temperature $T(x,t)$ and $s = i\omega$ [46]. The general solution of Eq. (5.22) is [48]:

$$\Theta(x,s) = C_1(s)e^{\lambda_1 x} + C_2(s)e^{\lambda_2 x} \tag{5.23}$$

with

$$\lambda_{1,2}(x,s) = -\frac{V}{2\chi} \mp \sqrt{\left(\frac{V}{2\chi}\right)^2 + \frac{s}{\chi}}. \tag{5.24}$$

Following a common procedure in the literature [47], we adopt the hypothesis of a semi-infinite radial [2] ($x \to \infty \Rightarrow \Theta \to 0$). This removes one boundary condition and collapses the spatial eigenstructure to a single decaying mode. Indeed, in slab geometry, the two eigenfunctions satisfy $|e^{\lambda_1 x}| \to 0$ and $|e^{\lambda_2 x}| \to \infty$ as $x \to \infty$, so the growing contribution must vanish ($C_2(s) = 0$). Thus, we have:

$$\Theta(x,s) = C_1(s) e^{\lambda_1 x}. \tag{5.25}$$

The subscript "1" will be omitted in the following for brevity. In principle, the constant multiplying the exponential would be determined from a boundary condition. However, by taking the logarithmic temperature derivative [46]—that is, applying the natural logarithm to Eq. (5.25) and differentiating with respect to x—this requirement can be bypassed in the subsequent analysis:

$$\frac{\Theta'}{\Theta} = \lambda \tag{5.26}$$

where $\Theta'(x,s) = \frac{d\Theta(x,s)}{dx}$.

On the other hand, writing Θ in polar form: $\Theta(x,s) = \mathcal{A}(x,s)e^{i\phi(x,s)}$, and substituting above, yields

$$\lambda = \frac{\mathcal{A}'}{\mathcal{A}} + i\,\phi' = \alpha + i\beta \tag{5.27}$$

where $\alpha(x,s) = \mathcal{A}'(x,s)/\mathcal{A}(x,s)$, $\beta = \phi'(x,s)$ are the spatial derivatives of the logarithmic amplitude and phase.

By substituting (5.25) into (5.22), one obtains the algebraic relation

$$\chi\,\lambda^2 + V\,\lambda - s = 0, \tag{5.28}$$

then, inserting (5.27) into this expression yields an equation that can be separated into its real and imaginary parts:

$$\begin{aligned} \chi(\alpha^2 - \beta^2) + V\,\alpha &= 0, \\ 2\chi\alpha\beta + V\,\beta &= \omega. \end{aligned}$$

Solving for χ and V gives

$$\chi = \frac{\omega\,\alpha}{\beta\,(\alpha^2 + \beta^2)} \tag{5.29}$$

[2] In flux–tube simulations, the domain is finite; the semi-infinite assumption is therefore understood as a local approximation within the source-excluded, high-coherence window, sufficiently far from the numerical boundaries.

$$V = \frac{\omega\ (\beta^2 - \alpha^2)}{\beta\,(\alpha^2 + \beta^2)}. \tag{5.30}$$

These are the closed-form expressions for χ and V, that can be obtained from a single-frequency modulation analysis [46].

As just shown, the estimation of the two transport coefficients requires first determining α and β, which can be computed from the FRF. To this end, the FRF is expressed as

$$G(x, \omega_0) = A(x, \omega_0)\, \mathrm{e}^{i\phi(x)}.$$

where $A(x) = |G(x)|$ and $\phi(x)$ denote, respectively, the amplitude and phase of the response at position x. In practice, α and β are estimated in two ways:

(i) the *two–point* transfer–function approach, using only two spatial locations;

(ii) the *weighted least–squares* (WLS) approach, which combines multiple spatial samples and uses the variances provided by the LPM as weighting factors.

The estimation is confined to a suitable spatial window, defined by selecting a high–coherence region using a magnitude-squared coherence threshold that balances preserving a sufficiently strong linear relation between $u(t)$ and $T_\perp(x, t)$ with maintaining a spatial window that contains enough grid points to ensure a more stable outcome. Additionally, within this region the logarithmic amplitude and the phase must exhibit an approximately linear behaviour so as to remain compatible with the assumption of spatially constant coefficients.

5.2.2 Two-Point Estimate

The first strategy consists in evaluating the transfer function at two points [46] within the high–coherence region. Two positions

$$x_A < x_B,$$

are selected, and the corresponding complex responses

$$G_A = A_A\, \mathrm{e}^{i\phi_A}, \qquad G_B = A_B\, \mathrm{e}^{i\phi_B},$$

are then considered. The α and β terms are then estimated by:

$$\alpha_{2-\mathrm{pt}} = \frac{\ln\left(\frac{A_B}{A_A}\right)}{\Delta x}, \qquad \beta_{2-\mathrm{pt}} = \frac{\phi_B - \phi_A}{\Delta x}. \tag{5.31}$$

With this approach, the two selected points are treated as representative of the entire window, under the assumption that the FRF is sufficiently regular and free of spikes—a condition that can, in principle, be achieved with a sufficiently large number of modulation periods. The two–point transport coefficients are then obtained by inserting (5.31) into (5.29)–(5.30):

$$\chi_{2-\mathrm{pt}} = \chi(\alpha_{2-\mathrm{pt}}, \beta_{2-\mathrm{pt}}), \qquad V_{2-\mathrm{pt}} = V(\alpha_{2-\mathrm{pt}}, \beta_{2-\mathrm{pt}}). \tag{5.32}$$

5.2.3 Weighted Least-Squares Estimate

The second strategy exploits all available spatial samples in the chosen high–coherence window away from the source and incorporates the statistical information provided by the LPM. For a set of positions $\{x_j\}_{j=1}^{N}$ in the window, the LPM yields estimates A_j, ϕ_j, together with their respective variances $\sigma_{A,j}^2, \sigma_{\phi,j}^2$. For small relative amplitude errors, the variance of the logarithmic amplitude is approximated as

$$\sigma_{\ln A,j}^2 \;\approx\; \left(\frac{\sigma_{A,j}}{A_j}\right)^2. \tag{5.33}$$

Thus, under the assumption that the logarithmic amplitude and the phase vary approximately linearly over the analysis window, the following linear models can be applied [49, 50]

$$\ln A_j \approx c_A + \alpha_{\mathrm{WLS}}\, x_j, \tag{5.34}$$

$$\phi_j \approx c_\phi + \beta_{\mathrm{WLS}}\, x_j, \tag{5.35}$$

where (c_A, c_ϕ) are intercepts and $(\alpha_{\mathrm{WLS}}, \beta_{\mathrm{WLS}})$ are the desired slopes in the window.

These models are fitted by weighted least-squares, using the LPM variances to define the weights:

$$w_{A,j} = \frac{1}{\sigma_{\ln A,j}^2}, \qquad w_{\phi,j} = \frac{1}{\sigma_{\phi,j}^2}. \tag{5.36}$$

For a generic weighted linear regression

$$y_j \approx a + b\, x_j, \qquad j = 1, \ldots, N,$$

with intercept a, slope b, and weights w_j, the WLS estimator can be written in compact form as

$$\begin{bmatrix} a \\ b \end{bmatrix} = \left(X^\top W X\right)^{-1} X^\top W\, y, \qquad X = \begin{bmatrix} 1 & x_1 \\ \vdots & \vdots \\ 1 & x_N \end{bmatrix}, \quad W = \mathrm{diag}(w_1, \ldots, w_N),$$

where $y = (y_1, \ldots, y_N)^\top$. The weighted residuals are

$$r_j = y_j - (a + b\, x_j),$$

and the weighted residual variance is estimated as

$$\hat{\sigma}_{\mathrm{res}}^2 = \frac{1}{N-2} \sum_{j=1}^{N} w_j\, r_j^2.$$

The covariance matrix for $(a, b)^\top$ is then

$$\mathrm{Cov} \begin{bmatrix} a \\ b \end{bmatrix} = \hat{\sigma}_{\mathrm{res}}^2 \left(X^\top W X\right)^{-1}.$$

Applied to Eqs. (5.34)–(5.35), with $(y_j, w_j) = (\ln A_j, w_{A,j})$ for the amplitude fit and $(y_j, w_j) = (\phi_j, w_{\phi,j})$ for the phase fit, this framework yields the estimates α_{WLS} and β_{WLS}, together with their regression variances $\sigma^2_{\alpha,\mathrm{WLS}} = \mathrm{Var}(\alpha_{\mathrm{WLS}})$ and $\sigma^2_{\beta,\mathrm{WLS}} = \mathrm{Var}(\beta_{\mathrm{WLS}})$, which are obtained from the (2,2) entry of the respective covariance matrices. Once $(\alpha_{\mathrm{WLS}}, \beta_{\mathrm{WLS}})$ have been obtained, the corresponding transport coefficients are computed as

$$\chi_{\mathrm{WLS}} = \chi(\alpha_{\mathrm{WLS}}, \beta_{\mathrm{WLS}}), \qquad V_{\mathrm{WLS}} = V(\alpha_{\mathrm{WLS}}, \beta_{\mathrm{WLS}}), \tag{5.37}$$

using Eqs. (5.29)–(5.30). The uncertainties $\sigma_{\chi,\mathrm{WLS}}$ and $\sigma_{V,\mathrm{WLS}}$ follow from first–order error propagation:

$$\sigma^2_{\chi,\mathrm{WLS}} \approx \left(\frac{\partial \chi}{\partial \alpha}\right)^2 \sigma^2_{\alpha,\mathrm{WLS}} + \left(\frac{\partial \chi}{\partial \beta}\right)^2 \sigma^2_{\beta,\mathrm{WLS}}, \tag{5.38}$$

$$\sigma^2_{V,\mathrm{WLS}} \approx \left(\frac{\partial V}{\partial \alpha}\right)^2 \sigma^2_{\alpha,\mathrm{WLS}} + \left(\frac{\partial V}{\partial \beta}\right)^2 \sigma^2_{\beta,\mathrm{WLS}}. \tag{5.39}$$

In summary, both methods extract $\lambda = \alpha + i\beta$ from the FRF and map it to (χ, V) through the advection–diffusion closure. The two–point method relies on two representative locations, whereas the WLS method uses all available spatial samples and provides confidence intervals.

Chapter 6

Simulation Setup and Results

In this chapter the main results obtained from the gyrokinetic simulations and the consequent signal analysis are presented. Building on the physical model and numerical framework introduced in the previous chapters, the focus is on a temperature–gradient–driven trapped–electron–mode regime and on its response to time–modulated ECRH source. The analysis has two goals: to clarify how turbulence spreads the injected heat signals, and to test the underlying assumptions of an advection–diffusion (AD) closure, identifying parameter regimes and spatial regions where such a closure may cease to be valid.

The chapter is organised as follows. First, the general simulation setup is described together with the reference turbulence regime in the absence of ECRH deposition, including basic linear properties and nonlinear saturation characteristics. The modulated ECRH deposition is then introduced and the spatial structure of the temperature response is analysed by computing the frequency–response function (FRF) at the ECRH modulation frequency for each point along the radial direction. On this basis, effective diffusion and advection coefficients are determined for a reference case. Subsequently, the way in which both the coherence between the diagnosed temperature signal and the imposed power–deposition signal and the inferred transport coefficients change as key control parameters of the simulations (such as the modulation frequency) are varied is examined.

6.1 Setup and Base ∇T-TEM Turbulence Scenario

The setup is based on that presented in [51], in a local flux-tube geometry based on the standard $\hat{s}$-α model [21]. The magnetic configuration is characterised by a safety factor and a magnetic shear given respectively by

$$q_0 = 1.4, \qquad \hat{s} := \frac{x}{q}\frac{\mathrm{d}q}{\mathrm{d}x} = 0.8,$$

and an inverse aspect ratio $\epsilon_{\mathrm{t}} = r/R_0 = 0.16$, with major radius R_0. The simulations are near-electrostatic, with normalised electron pressure $\beta = 10^{-3}$, while the Shafranov shift α is set equal to zero (technically inconsistent with non-zero β).

The radial coordinate x and binormal coordinate y are normalised to the ion-sound gyroradius ρ_{s}.

The kinetic species are singly charged ions and electrons. Quasi-neutrality is imposed with $n_{e0} = n_{i0} = n_0$, the electron-to-ion temperature ratio is $T_{e0}/T_{i0} = 2$, and the electron-to-ion mass ratio is $m_e/m_i \approx 1/1836$.

The normalised background density and temperature gradients are chosen as

$$\omega_{T,\{i,e\}} = \{0,\, 4.5\}, \qquad \omega_{n,\{i,e\}} = 3.$$

The perpendicular box size is chosen as

$$L_x = 5\, L_{x,\min} = \frac{5}{k_{y,\min}\,\hat{s}} = 125\,\rho_s, \qquad L_y = \frac{2\pi}{k_{y,\min}} \approx 125.7\,\rho_s,$$

where $k_{y,\min} = 0.05$ is the minimum binormal wavenumber resolved in the y direction, and

$$\rho_s = \frac{c_s}{\Omega_{ci}} = \frac{\sqrt{T_{e0} m_i}}{eB_0},$$

with $c_s = \sqrt{T_{e0}/m_i}$ the ion-sound speed. Perpendicular wavenumbers are therefore naturally expressed in the dimensionless form $k_y \rho_s$. The width $L_{x,\min}$ represents the minimum radial extent required by the parallel boundary conditions at $k_{y,\min}$. Choosing $L_x = 5\, L_{x,\min}$ ensures that the radial domain is wide enough to capture the turbulent TEM streamers as determined by convergence analysis according to M.J. Pueschel (personal communication, October 2025).

The computational grid resolves the five-dimensional phase space with

$$(N_x,\, N_y,\, N_z,\, N_{v_\parallel},\, N_\mu) = (128,\, 64,\, 24,\, 50,\, 8).$$

Time advancement is performed using a fourth-order Runge–Kutta scheme with adaptive time-stepping.

With this setup, the system is evolved up to $t_{\max} = 300\, R_0/c_s$, ensuring the development of fully saturated ∇T-TEM turbulence [52, 51].

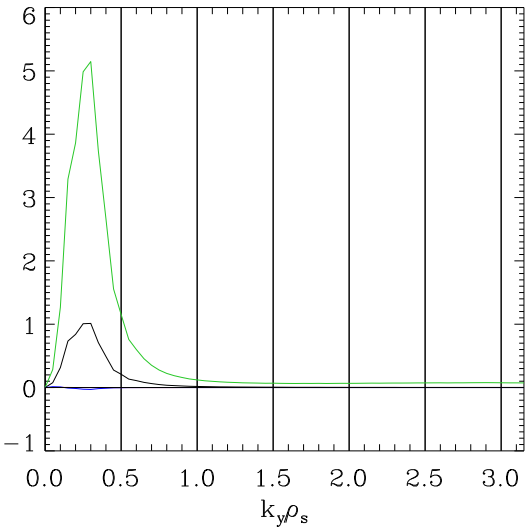

Figure 6.1: Time-averaged spectral distribution of the electron fluxes as a function of k_y. The time-averaging window is $t \in [100,300]$. The green line represents the electrostatic heat flux $Q_{\rm es}/(c_{\rm s}\,\rho_{\rm s}^2\,n_0 T_{\rm e0}/R_0^2)$, the black line the electrostatic particle flux $\Gamma_{\rm es}/(c_{\rm s}\,\rho_{\rm s}^2\,n_0/R_0^2)$, and the blue line the electromagnetic heat flux $Q_{\rm em}/(c_{\rm s}\,\rho_{\rm s}^2\,n_0 T_{\rm e0}/R_0^2)$. Heat transport is dominated by large-scale, but not system-size, modes, while contributions from the highest-k_y (near-ETG-scale) modes are comparatively small— Base ∇T-TEM turbulence scenario.

Figure 6.1 shows that the majority of the electron heat flux is concentrated in the large scale range $0.05 \lesssim k_y \lesssim 0.5$, with smaller contributions from near-ETG scales.
The nonlinear evolution of the system is illustrated in Fig. 6.2, which displays the temporal evolution of volume-averaged squared fluctuating quantities — the perpendicular temperature $\langle|T_\perp|^2\rangle$, the parallel temperature $\langle|T_\parallel|^2\rangle$, the density $\langle|n|^2\rangle$, and the parallel velocity $\langle|u_\parallel|^2\rangle$. Figure 6.3 shows the time evolution of the volume-averaged electrostatic electron heat flux $Q_{\rm es}$ and particle flux $\Gamma_{\rm es}$. After an initial exponential growth phase dominated by the linear TEM instability, all quantities saturate at $t \approx 50$. Beyond this point, they fluctuate around mean values, indicating the establishment of a statistically steady turbulent state. The absence of persistent growth and the presence of finite-amplitude oscillations reflect a balance between the drive from the background electron temperature gradient and the nonlinear energy transfer to damped modes. In this regime, ion flux contributions remain much smaller than their electron counterparts. The time window for computing the time-averaged values of the observables such as the flux spectra is taken as $t \in [100,300]$.

Remark 1. In absence of external heating modulation, the temperature gradient naturally develops persistent peaks that remain localized at the rational surfaces. As shown in Sec. 6.2, the ECRH modulation operates on time scales much shorter than those characterizing the evolution of these corrugations. They can therefore be regarded as a quasi-static background upon which the driven perturbation is superimposed. As a result, the FRF

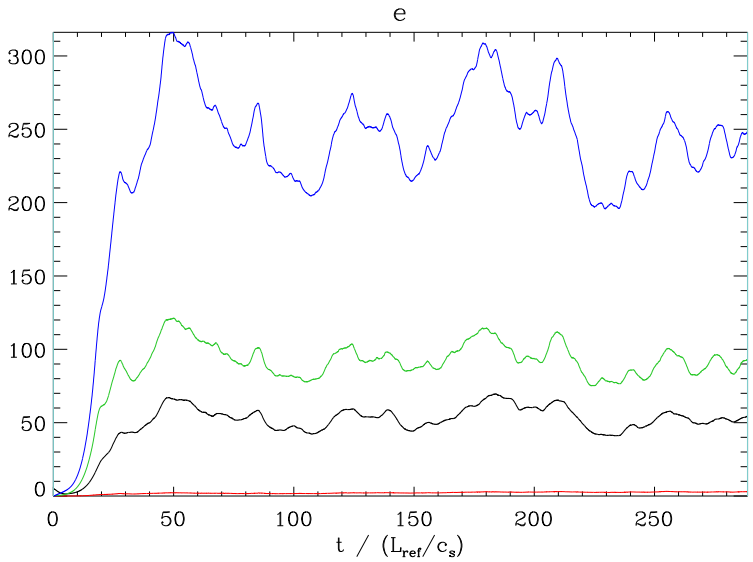

Figure 6.2: Time evolution of the volume-averaged squared electron fluctuation amplitudes. The blue line shows the perpendicular temperature fluctuations $\langle|T_\perp|^2\rangle/(T_{e0}^2\rho_s^2/R_0^2)$, the green line the parallel temperature fluctuations $\langle|T_\parallel|^2\rangle/(T_{e0}^2\rho_s^2/R_0^2)$, the black line the density fluctuations $\langle|n|^2\rangle/(n_0^2\rho_s^2/R_0^2)$, and the red line the parallel velocity fluctuations $\langle|u_\parallel|^2\rangle/(v_{Te}^2\rho_s^2/R_0^2)$ — Base ∇T-TEM turbulence scenario.

will be affected by this behaviour, and consequently, the transport coefficients χ and V are expected to exhibit a pronounced radial dependence. This implies that a simple advection–diffusion model that assumes a constant background gradient and ignores the presence of local oscillations may become inadequate.

Figure 6.4 shows the time-averaged radial profile of the normalised local electron-temperature gradient $\tilde{\omega}_{T_e}(x)$, as a function of radial position. It exhibits a sequence of sharp, regularly spaced spikes in x, with five dominant peaks across the domain. These peaks are located at $x \in \{-50, -25, 0, 25, 50\}$, in correspondence with the rational surfaces of the flux tube. Figure 6.5 displays the spatio–temporal evolution of $\tilde{\omega}_{T_e}(x,t)$. The same structures appear as nearly vertical stripes, demonstrating that they are long-lived and essentially stationary rather than transient, random fluctuations.

This behaviour arises from the topology of the magnetic field lines. On a rational surface, the safety factor $q(x)$ assumes a rational value $q = m/n$, so that a magnetic field line closes on itself after m toroidal and n poloidal turns, instead of sampling the entire flux surface ergodically. Thus, at rational surfaces the parallel dynamics is effectively periodic: a particle or perturbation following such a field line repeatedly samples the same locations, rather than uniformly exploring the whole flux surface.

Trapped-electron-mode turbulence is sensitive to this periodicity. Temperature corrugations tend to lock to rational surfaces because the closed field-line geometry facilitates

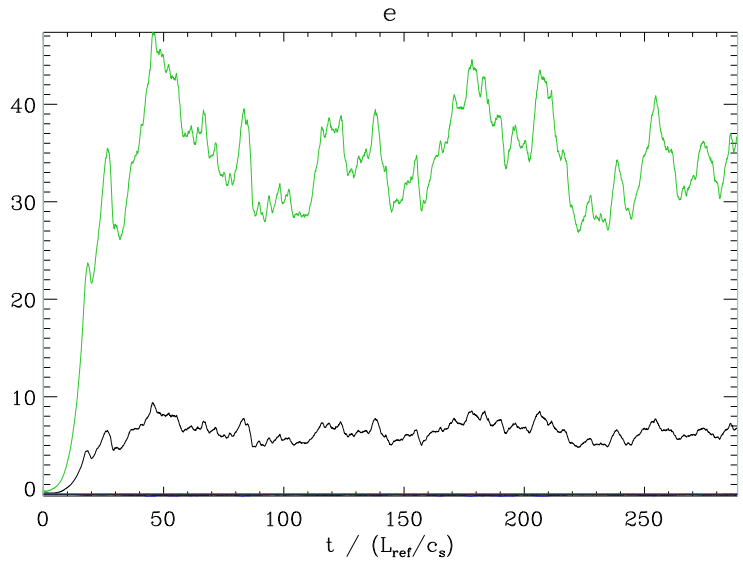

Figure 6.3: Time evolution of the volume-averaged electron heat and particle fluxes. The green line shows the electrostatic heat flux $\langle Q_{\mathrm{es}}\rangle/(c_{\mathrm{s}}\,\rho_{\mathrm{s}}^2\,n_0 T_{\mathrm{e}0}/R_0^2)$, the black line the electrostatic particle flux $\langle \Gamma_{\mathrm{es}}\rangle/(c_{\mathrm{s}}\,\rho_{\mathrm{s}}^2\,n_0/R_0^2)$, and the blue line the electromagnetic heat flux $Q_{\mathrm{em}}/(c_{\mathrm{s}}\,\rho_{\mathrm{s}}^2\,n_0 T_{\mathrm{e}0}/R_0^2)$ — Base ∇T-TEM turbulence scenario.

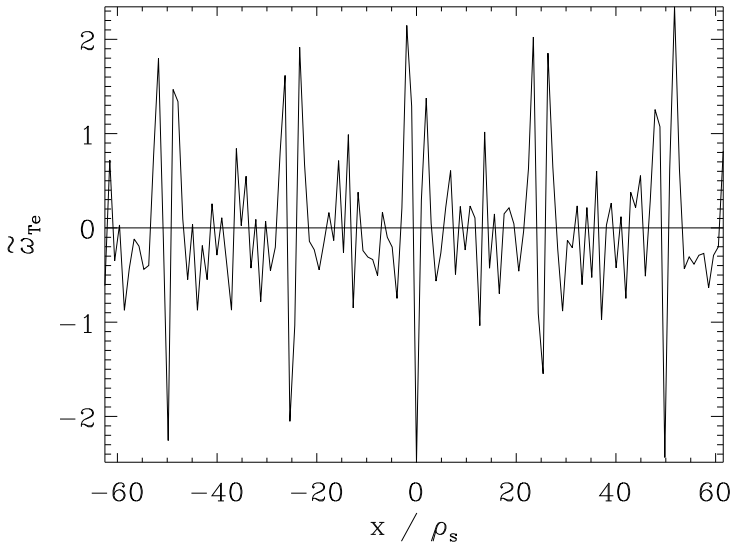

Figure 6.4: Time-averaged profile of the perturbed normalised electron-temperature gradient $\tilde{\omega}_{T_e}(x)$. The time-averaging window is $t \in [100{,}300]$ — Base ∇T-TEM turbulence scenario.

the maintenance of coherent patterns at those locations. Stated another way, the background electron-temperature profile becomes radially corrugated: the local gradient is flattened or steepened in narrow radial bands centred on the rational surfaces. This is precisely what is observed in Figs. 6.4 and 6.5: the narrow, robust spikes in the fluctuation of the normalised temperature gradient appear at the radii of rational surfaces and can be interpreted as the signatures of turbulence-generated "hills and wells" in the gradient, pinned to the underlying magnetic geometry.

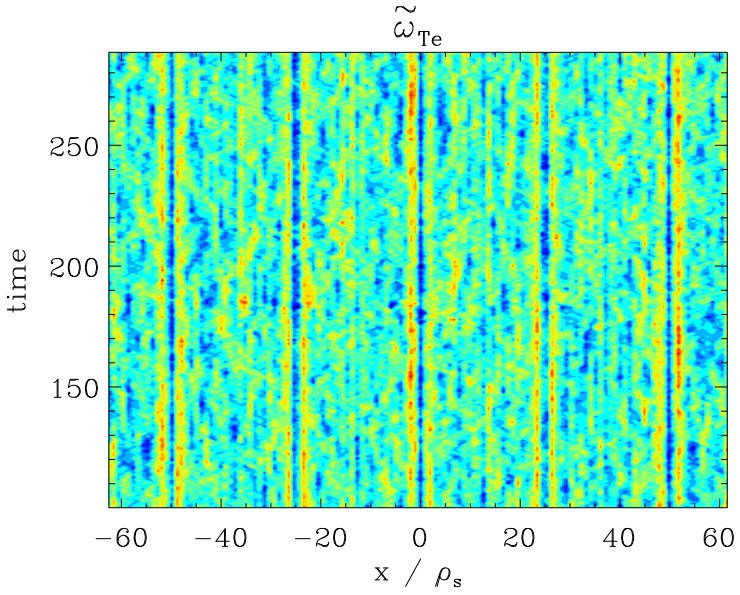

Figure 6.5: Spatio–temporal evolution of $\tilde{\omega}_{T_e}(x,t)$ — Base ∇T-TEM turbulence scenario.

Introducing the normalised autocorrelation function $C(\Delta t)$ of the perpendicular electron temperature fluctuation field $T_\perp(x,y,z,t)$, it is possible to estimate a characteristic turbulence time scale. Denoting by $\langle\cdot\rangle_V$ a volume average and by $\langle\cdot\rangle_t$ a time average, the normalised autocorrelation can be written as

$$C(\Delta t) = \frac{\big\langle \big\langle T_\perp(x,y,z,t)\, T_\perp(x,y,z,t+\Delta t)\big\rangle_t \big\rangle_V}{\big\langle \big\langle T_\perp(x,y,z,t)^2\big\rangle_t \big\rangle_V}, \qquad C(0)=1.$$

The correlation time τ_c is taken as the lag at which $C(\Delta t)$ decays to $1/e$ of its zero-lag value, i.e. $C(\tau_c) = 1/e$. This quantity provides a characteristic turbulence decorrelation time scale. For the base ∇T–TEM setup, one finds $\tau_c \approx 1.5\, R_0/c_s$ which is on the order of microseconds.

Finally, Fig. 6.6 shows a snapshot of the contour plot of the perpendicular electron temperature fluctuations, from which the spatial structure of the turbulence in the base ∇T-TEM state can be observed.

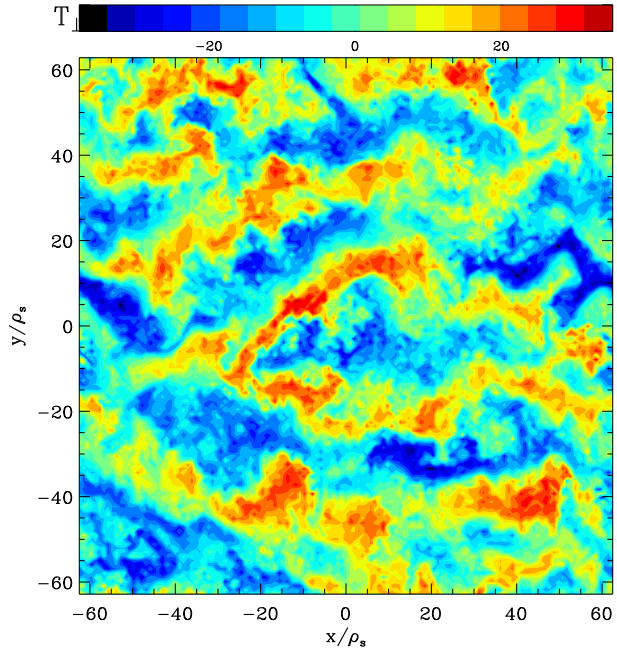

Figure 6.6: Contour plot of electron perpendicular temperature ($T_\perp/(T_{e0}\rho_s/R_0)$) at $t = 250.13\, R_0/c_s$ — Base ∇T-TEM turbulence scenario.

6.2 Modulated Electron Cyclotron Deposition Scenario

The implementation of the ECRH source in GENE requires the specification of several parameters characterising the energy deposition [19]. The main parameters are the spectral width in parallel velocity $\Delta v_\parallel$, the resonant parallel velocity $v_{\parallel,\mathrm{res}}$, the deposition peak power density p_{EC}, the deposition half width W, the modulation frequency $\omega_0 = 2\pi f_0 = \frac{2\pi}{T}$, and the deposition center location x_{dep}.

Following [38], a representative value for the resonant velocity is $v_{\parallel,\mathrm{res}} \approx 2v_{T_e}$, assuming the electrons to have a speed on the order of 10^7 m/s in typical fusion-plasma conditions. The spectral width is chosen as $\Delta v_\parallel = 0.3$ — small enough to preserve the resonant character of the interaction but large enough to ensure physical consistency [19]. For the Gaussian spatial profile, it is assumed that $\sigma_x = \sigma_y =: \sigma_\perp$ (isotropic source in the perpendicular plane), and $\sigma_z = 1$. It can now be defined a baseline set of deposition parameters (used for all simulations unless explicitly stated otherwise). In this baseline configuration, the peak deposited power density is $p_{\mathrm{EC}} = 0.002\, p_{\mathrm{ref}}$, the perpendicular half-width of the source profile is taken as $W = 3\sigma_\perp = 4.5\, \rho_s$, and the deposition is centred at $x_{\mathrm{dep}} = -20$. With this setup, several modulation frequencies are tested, one at time: $f_0 \in \{1/3, 1/9, 1/15, 1/21, 1/27, 1/45\}$. For all simulations, the analysis is performed over an integer number of modulation periods. Typically, between 10 and 25 periods are used, providing a sufficiently long time series to reduce statistical fluctuations

and improve the accuracy of the inferred quantities.

For brevity, each simulation will be referred to by the labels listed in Table 6.1.

Modulation frequency f_0:	1/3	1/9	1/15	1/21	1/27	1/45
Label:	p3bb	p9bb	p15bb	p21bb	p27bb	p45bb

Table 6.1: Modulation frequencies and corresponding run labels.

The simulation setup also includes a current–drive component; however, since the subsequent analysis focuses on heat deposition and the resulting temperature response, the term ECRH is used throughout for clarity. An assessment of how v_{res} influences the system's response is deferred to future investigations.

6.2.1 ECRH Modulation Reference Case

In the following, a reference case is defined by $p_{\mathrm{EC}} = 0.002\, p_{\mathrm{ref}}$, $W = 4.5$, and $f_0 = (1/15)\, c_{\mathrm{s}}/R_0$, hereafter referred to as p15bb, which will serve as the basis for the subsequent analysis. The discussion on this reference case follows the same structure as in the previous section, in order to illustrate how the modulated power deposition interacts with the turbulence and background corrugations identified in the previous case. The analysis will then proceed with the system's temperature response analysis.

In general, simulations with modulated ECRH deposition exhibit an initial transient phase before reaching an equilibrated frequency response regime suitable for analysis. The duration of this transient depends mainly on the modulation amplitude and frequency. In this case, after ≈ 705 time units this regime is reached. All the time-averaged quantities are computed considering 23 modulation periods, in a time window $t \in [705{,}1050]$. From Fig. 6.7, no clear shifts in spectral contributions to the flux are observed with respect to the base case without ECRH deposition.

Figure 6.8 shows that for this case the oscillation of $T_\perp$ exhibits a coherent temporal structure, with amplitude values reaching up to 10^3 . From Fig. 6.9, on the other hand, it can be observed that the electrostatic heat flux is approximately $\approx 14\%$ lower compared to the case without ECRH. This is an important feature, as one does not aim—at least in principle—for the modulated ECRH deposition to strongly affect the background turbulence or the system itself.

However, finding the right balance is nontrivial: the system must be perturbed sufficiently to allow its response to be measurable, yet not so strongly as to modify its dynamics. As can be seen in this case, compared to the reference run, a finite electromagnetic heat flux appears, indicating some degree of interaction induced by the deposition. Nevertheless, this contribution is small and thus is neglected in the present analysis.

Figure 6.10, illustrates the effect of the modulated ECRH deposition on the turbulence–induced corrugations of electron temperature, with its time evolution shown in Fig. 6.11 .

When the modulated power source is applied at $x_{\mathrm{dep}} = -20$, the pre–existing corrugations are still visible in the background, but a new, much stronger feature appears

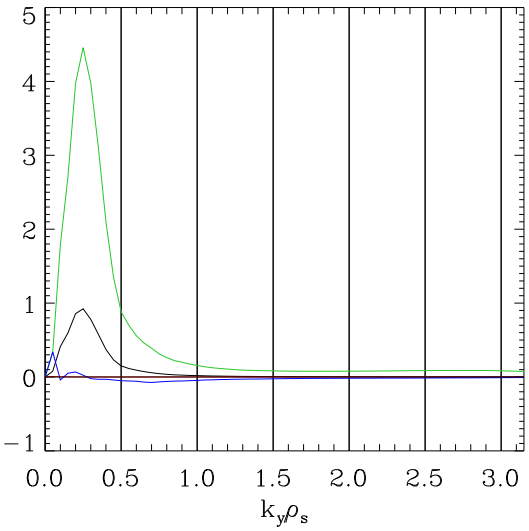

Figure 6.7: Time-averaged spectral distribution of the electron fluxes as a function of k_y. The time-averaging window is $t \in [705,1050]$. The green line represents the electrostatic heat flux $Q_{\rm es}/(c_{\rm s}\,\rho_{\rm s}^2\,n_0 T_{\rm e0}/R_0^2)$, the black line the electrostatic particle flux $\Gamma_{\rm es}/(c_{\rm s}\,\rho_{\rm s}^2\,n_0/R_0^2)$, and the blue line the electromagnetic heat flux $Q_{\rm em}/(c_{\rm s}\,\rho_{\rm s}^2\,n_0 T_{\rm e0}/R_0^2)$. Also in this case, heat transport is dominated by turbulence induced by large-scale instabilities — ECRH deposition case p15bb.

around the deposition radius. In Fig. 6.10 this shows up as a pronounced negative excursion of $\tilde{\omega}_{T_e}$, with an amplitude several times as large as the surrounding spikes and localized within a narrow region around $x_{\rm dep}$. Superimposed on this large excursion, one can still identify a narrow spike whose position coincides with the nearby rational surface at $x = -25$, indicating that the rational–surface corrugation survives as a small-scale imprint inside the driven perturbation.

From the spatio-temporal plot in Fig. 6.11, we observe that the modulation produces a clear periodic pattern in time, with a frequency matching that of the applied ECRH drive.

Overall, these plots demonstrate that the modulated ECRH drive locally and periodically modifies the temperature gradient in the vicinity of the deposition point, superimposed on the turbulence–induced corrugated background that remains essentially unchanged away from $x_{\rm dep}$.

Figures 6.12 show the electron perpendicular temperature contour plot evolution along an entire modulation period for the reference modulation case. Finally, Fig. 6.13 shows the evolution of the squared electron perpendicular temperature profile in space and time for the same run. This representation highlights both the localization of the modulated heat source and the subsequent radial propagation of the temperature perturbation. A clear left–right asymmetry around the deposition point can also be observed.

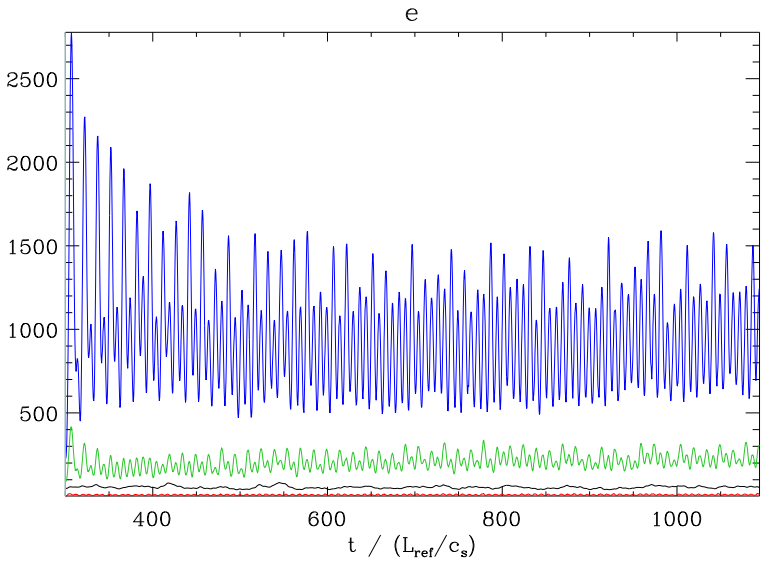

Figure 6.8: Time evolution of the volume-averaged squared electron fluctuation amplitudes. The blue line shows the perpendicular temperature fluctuations $\langle|T_\perp|^2\rangle/(T_{e0}^2\rho_s^2/R_0^2)$, the green line the parallel temperature fluctuations $\langle|T_\parallel|^2\rangle/(T_{e0}^2\rho_s^2/R_0^2)$, the black line the density fluctuations $\langle|n|^2\rangle/(n_0^2\rho_s^2/R_0^2)$, and the red line the parallel velocity fluctuations $\langle|u_\parallel|^2\rangle/(v_{Te}^2\rho_s^2/R_0^2)$ — ECRH deposition case p15bb.

6.2.2 Signal Analysis for the Reference Case

In this section the system's response for the reference case p15bb is analysed by post-processing the temperature signal. From the time series are extracted (i) the complex frequency response function $G(x, f_0)$ at the fundamental modulation frequency $f_0 = \omega_0/2\pi$, separated into its amplitude $|G(x, f_0)|$ and phase $\phi(x)$ (Fig. 6.14), and (ii) the amplitudes of the first three harmonics of the temperature response $|Y(x, f_k)|$ (Fig. 6.15). The sharp localised spike associated with the presence of a rational surface at $x = -25\rho_s$, observed in the previous analyses, affects the FRF in both phase and amplitude, making them asymmetric.

It is worth noting that, as expected from the discussion in Chapter 5, a decrease in amplitude corresponds to an increase in phase uncertainty.

As anticipated in the theoretical discussion, the transport coefficients will be calculated only in a region that lies outside the source itself and, at the same time, retains sufficiently high signal quality. For this reason, in Figures 6.14, 6.15 and 6.16 the radial extent of the ECRH deposition region will be marked with blue dashed vertical lines, and the interval where the magnitude-squared coherence (MSC) between input and output remains above 0.75 with black dashed lines. We refer to the latter as the high-coherence region. Outside this range the signal becomes too noisy, and is therefore discarded. The threshold is set to 0.75 according to Sec.5.2, as a compromise between maintaining a reasonably strong linear relation between the deposition signal and the temperature signal, and ensuring a sufficiently large spatial window with enough grid points.

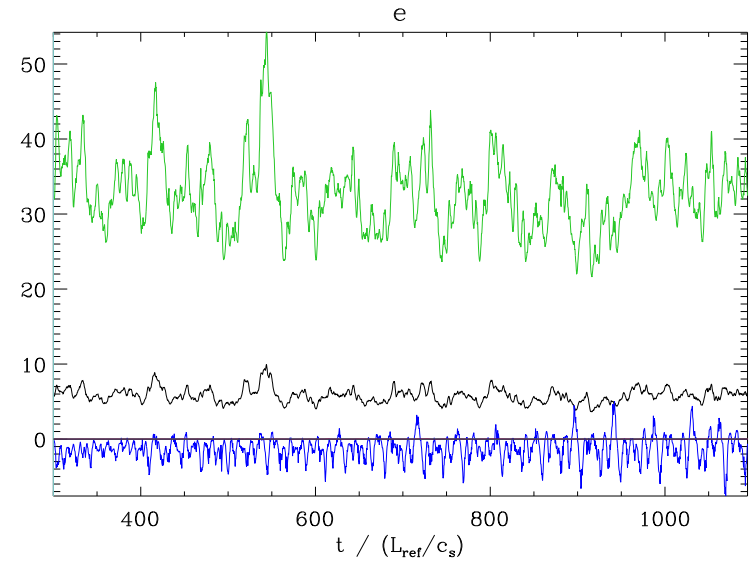

Figure 6.9: Time evolution of the volume-averaged electron heat and particle fluxes. The green line shows the electrostatic heat flux $\langle Q_{\mathrm{es}}\rangle/(c_{\mathrm{s}}\,\rho_{\mathrm{s}}^2\,n_0 T_{\mathrm{e}0}/R_0^2)$, the black line the electrostatic particle flux $\langle \Gamma_{\mathrm{es}}\rangle/(c_{\mathrm{s}}\,\rho_{\mathrm{s}}^2\,n_0/R_0^2)$, and the blue line the electromagnetic heat flux $Q_{\mathrm{em}}/(c_{\mathrm{s}}\,\rho_{\mathrm{s}}^2\,n_0 T_{\mathrm{e}0}/R_0^2)$ — ECRH deposition case p15bb.

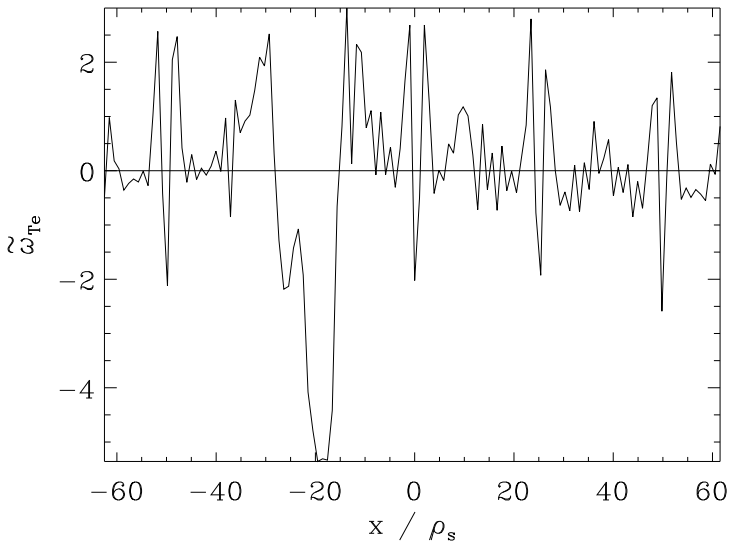

Figure 6.10: Time-averaged profile of the perturbed normalised electron-temperature gradient $\tilde{\omega}_{T_e}(x)$. The time-averaging window is $t \in [705{,}1050]$. — ECRH deposition case p15bb.

Within the two remaining windows — one on the left and one on the right of the deposition point — that will be considered for the analyses, it is further required that

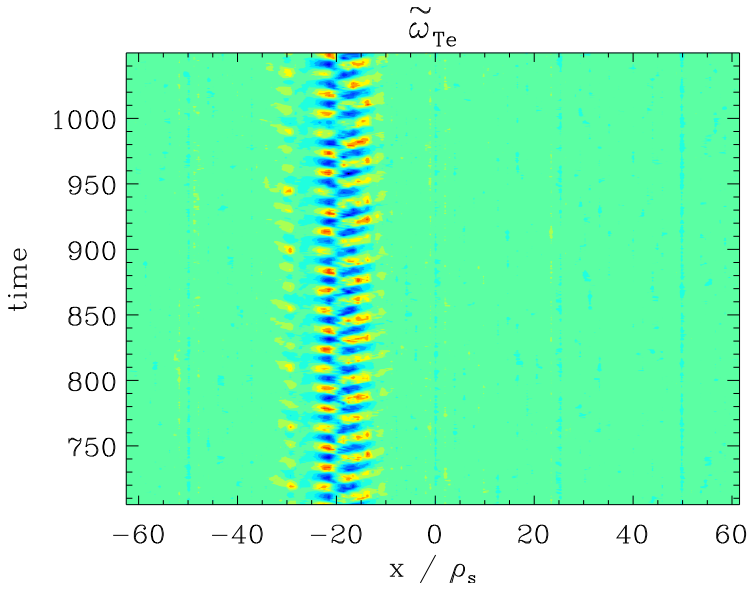

Figure 6.11: Spatio-temporal evolution of the normalised local electron-temperature gradient $\tilde{\omega}_{T_e}(x,t)$ — ECRH deposition case p15bb.

the spatial behaviour of the transfer function be consistent with the assumptions of the advection–diffusion model. In particular, the phase $\phi(x)$ and the logarithm of the amplitude $\log A(x)$ with $A(x) = |G(x, f_0)|$, must in principle be linear in x, so that $\phi'(x)$ and $A'(x)/A(x)$ are constant. As it can be seen from Fig. 6.14, these conditions break down in the vicinity of the spike associated with the rational surface, where the spatial dependence of both $\log A(x)$ and $\phi(x)$ becomes strongly non linear. In this interval it is therefore not meaningful to represent the response in terms of a single pair of constant transport coefficients (χ, V), since any such estimate would be strongly dependent on the chosen fitting window. This behaviour highlights a severe limitation of constant-coefficient transport models.

For this reason, although in this particular case the high-coherence region is wider in the left window, the estimation of the transport coefficients will be restricted to the one in the right side. For the p15bb setup, the high-coherence region is located in the range $x \in [-31.9881, -10.3346]$, while the deposition region is within $x \in [-24.5,\ -15.5]$. The selected region for the analysis will therefore be $x \in [-15.2559,\ -10.3346]$, which contains six grid points.

From Fig. 6.15, it can be observed that the amplitude of the fundamental harmonic is consistently much larger than that of the higher-order ones. This indicates that nonlinear effects of the system on the temperature signal are moderately pronounced in this case. A quantitative measure of these effects can be expressed through the total harmonic distortion (THD), which quantifies the relative contribution of all harmonic components with respect to the fundamental response. Denoting by $Y(x, f_0)$ the complex amplitude of the fundamental at frequency f_0, and by $Y(x, f_k)$ the amplitudes at the harmonic

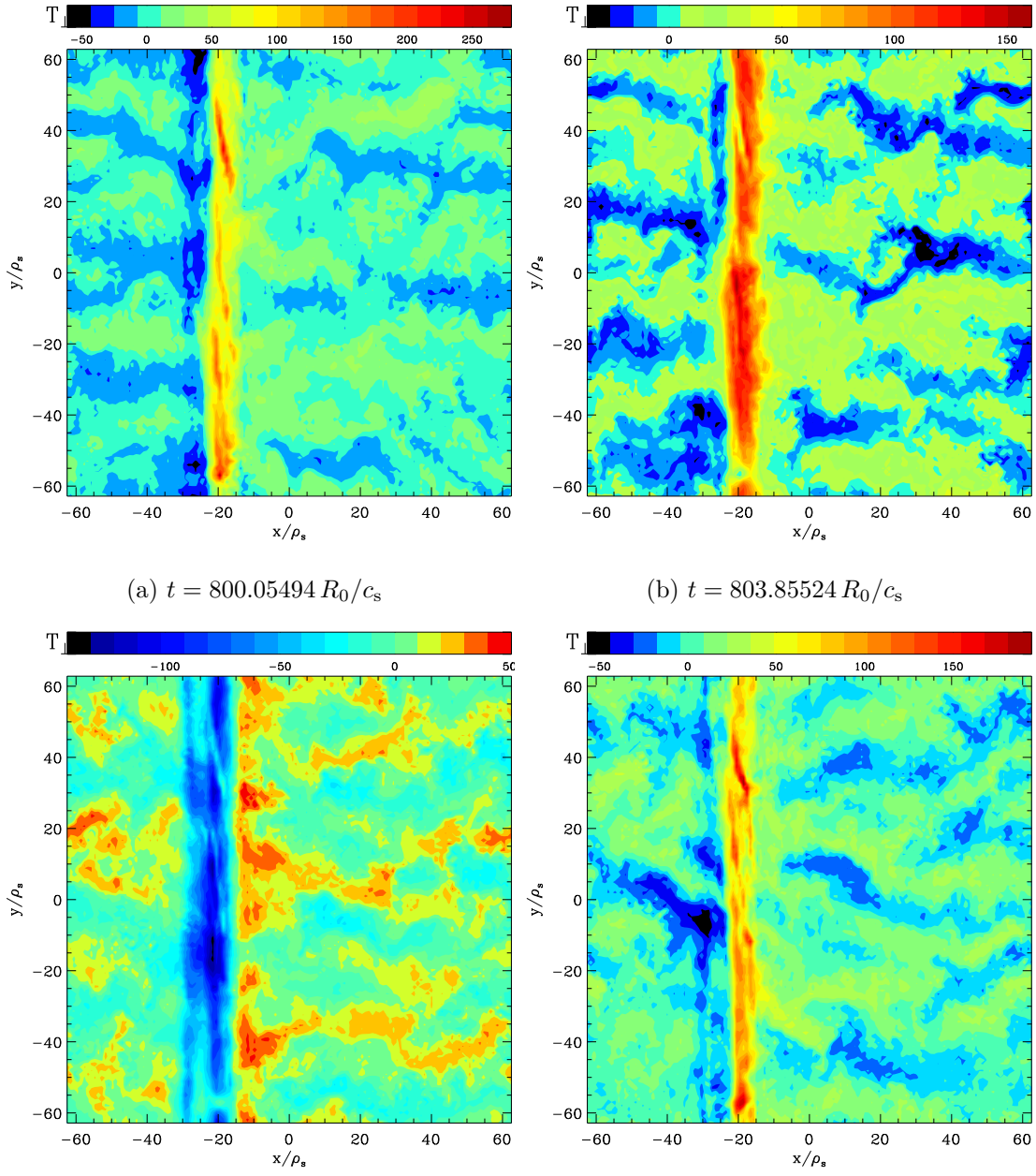

(a) $t = 800.05494\, R_0/c_\mathrm{s}$

(b) $t = 803.85524\, R_0/c_\mathrm{s}$

(c) $t = 811.38509\, R_0/c_\mathrm{s}$

(d) $t = 814.89891\, R_0/c_\mathrm{s}$

Figure 6.12: Contour plots of electron perpendicular temperature ($T_\perp/(T_{\mathrm{e}0}\rho_\mathrm{s}/R_0)$) during a deposition period — ECRH deposition case p15bb.

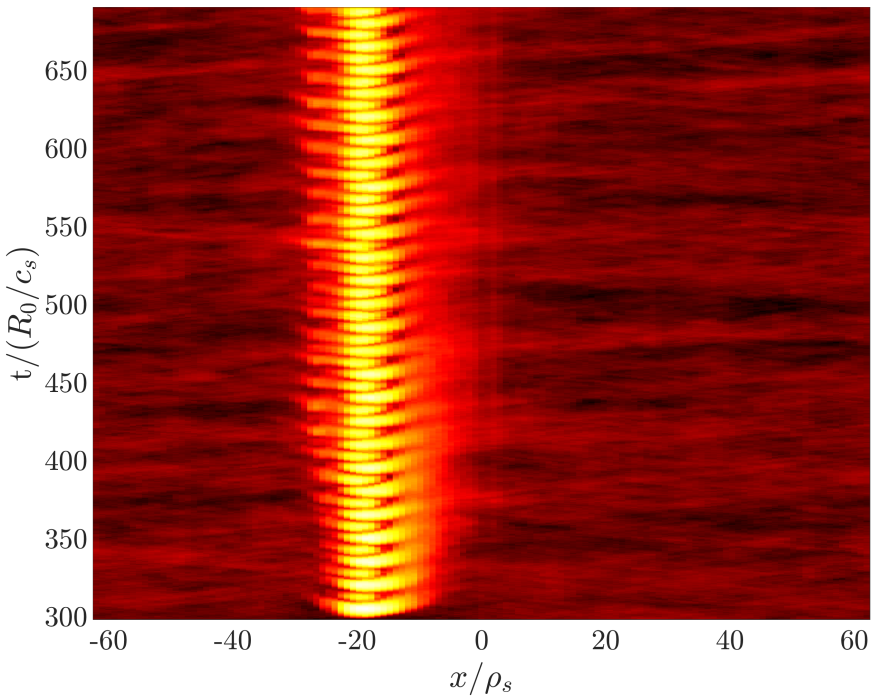

Figure 6.13: Evolution of the squared electron perpendicular temperature in space and time for the reference modulated ECRH case p15bb. It can be noticed the localisation of the heat source together with the left–right asymmetric spreading of the temperature perturbation around the deposition point.

frequencies $f_k = kf_0$ with $k \geq 2$, the THD at position x is defined as

$$\mathrm{THD}(x) = 100 \times \frac{\sqrt{\sum_{k\geq 2} |Y(x, f_k)|^2}}{|Y(x, f_0)|} \,. \tag{6.1}$$

In Fig. 6.16, it is shown that within most of the high-coherence region the THD remains at relatively low values — below 10% — and reaches values up to about 15% within the analysis window, resulting in an average value of 12.16% in the high-coherence region. In the rightmost part of the domain, the THD exhibits a sharp rise as the amplitudes of all harmonics become comparable. This increase stems from the original signal being masked by the (noise-like) turbulence, and highlights the reduced spatial spreading of the temperature signal in this setup. Since the analysis of higher harmonics is motivated by the need to characterise the nonlinear scaling of transport, and the measured response at these harmonics inevitably incorporates part of the turbulent spectrum, it may be worthwhile to examine whether—and to what extent—the ratio between higher-order and fundamental harmonic amplitudes depends on the applied deposition amplitude. An investigation of this dependence may provide a meaningful direction for future work.

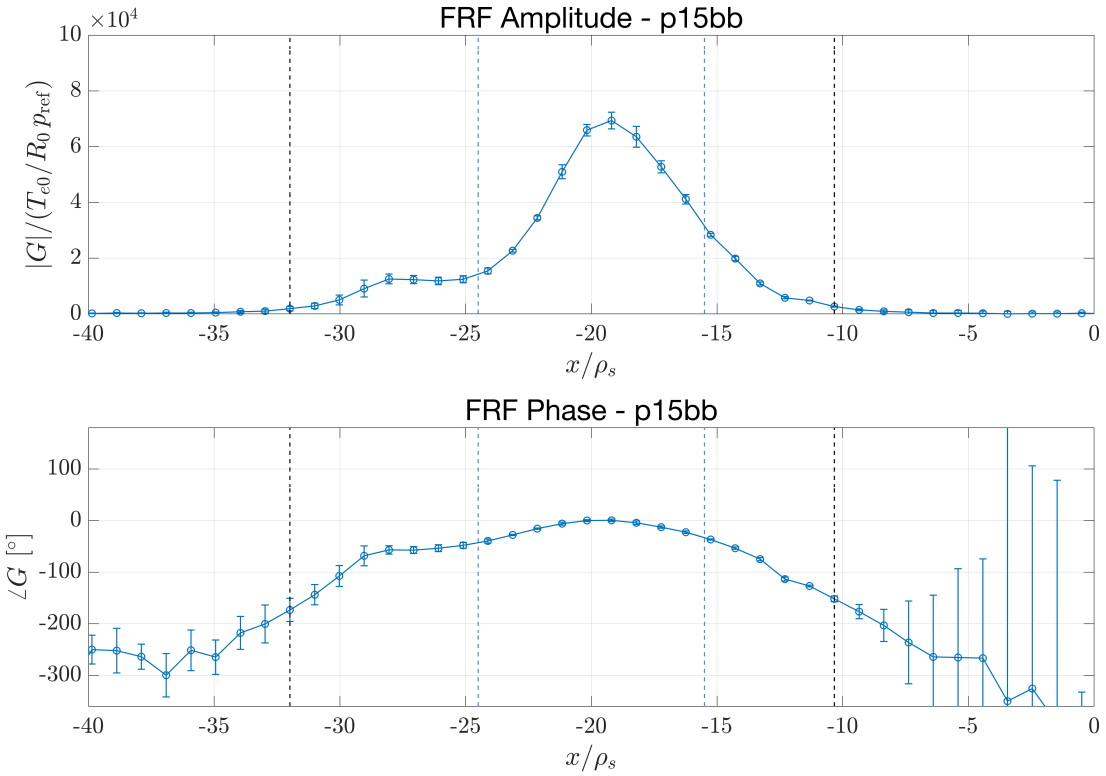

Figure 6.14: The top panel shows the FRF amplitude, while the bottom the FRF phase, for each spatial point — ECRH deposition case p15bb.

6.2.3 Transport Coefficient Estimation for the Reference Case

The analysis now turns to the transport coefficients inferred from the linear model. It should be recalled that the deposition is modulated at a single frequency. Furthermore, as discussed in Sec. 5.2, the solution of the Laplace-transformed transport model at the modulation frequency f_0 — under the assumptions of slab geometry, semi-infinite domain[1], spatially constant transport coefficients, and an analysis region free of sources — takes the form:

$$\Theta(x) = C_1 \exp\,(\lambda x),$$

with the complex spatial eigenvalue $\lambda = \alpha + i\beta = \frac{d}{dx}\ln[A(x)] + i\phi'(x)$.

To find α and β, and thus the complex exponent, two fitting strategies can be applied:

(i) *two–point method*: two positions x_1 and x_2 are selected within the analysis window, and the λ components are estimated as [46]: $\alpha_{2\text{-pt}} = \ln[A(x_2)/A(x_1)]/(x_2 - x_1)$ and

[1] In flux–tube simulations, the domain is finite; the semi-infinite assumption is therefore understood as a local approximation within the source-excluded, high-coherence window, sufficiently far from the numerical boundaries.

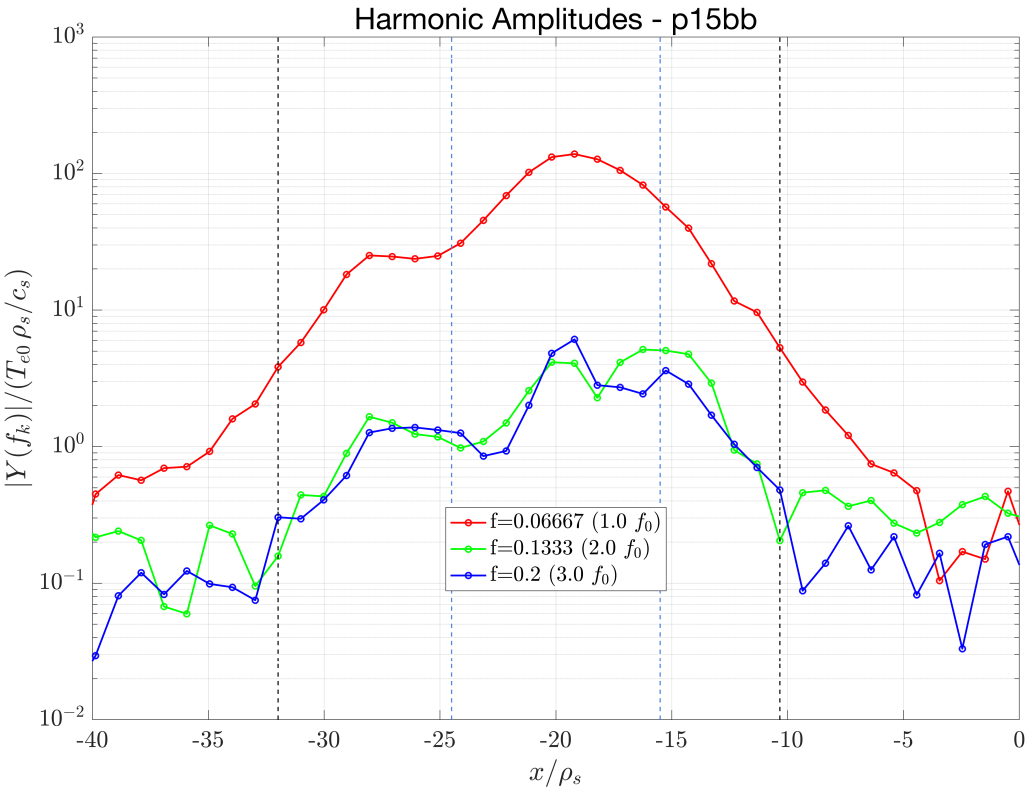

Figure 6.15: Spatial profiles of the fundamental (f_0), second ($f_2 = 2f_0$), and third ($f_3 = 3f_0$) harmonic amplitudes — ECRH deposition case p15bb .

$\beta_{\text{2-pt}} = (\phi(x_2) - \phi(x_1))/(x_2 - x_1)$ respectively. These estimates are then mapped to $\chi_{\text{2-pt}}$ and $V_{\text{2-pt}}$ using the analytic relations between λ and the transport coefficients.

(ii) *weighted least–squares* (WLS): all available points in the window are used to fit a complex exponential to $A(x)$ and $\phi(x)$ via weighted least squares, with weights given by the estimated variances of amplitude and phase at each x given by the Local Polynomial Method (LPM). This yields WLS estimates α_{WLS} and β_{WLS}, together with their uncertainties, which are again converted into χ_{WLS} and V_{WLS}.

For the reference setup p15bb, the resulting transport coefficients are:

$$\chi_{\text{WLS}} = (1.27 \pm 0.10)\,\frac{c_s\rho_s^2}{R_0}, \qquad \chi_{\text{2-pt}} = 1.24\,\frac{c_s\rho_s^2}{R_0}, \tag{6.2}$$

$$V_{\text{WLS}} = (0.14 \pm 0.06)\,\frac{c_s\rho_s}{R_0}, \qquad V_{\text{2-pt}} = 0.17\,\frac{c_s\rho_s}{R_0}. \tag{6.3}$$

From the fitted coefficients the spatial profiles of the amplitude and phase of the temperature response at the modulation frequency can be reconstructed, and it is possible to quantify the reconstruction error, assessing the quality of the advection-diffusion model.

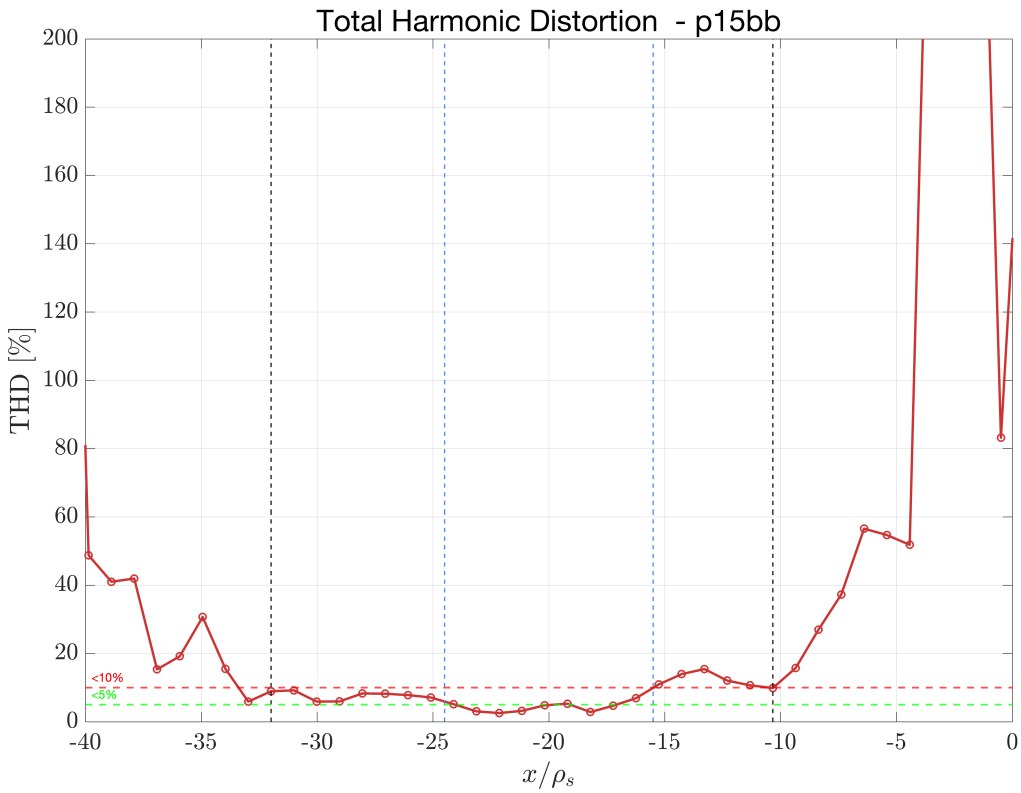

Figure 6.16: Total harmonic distortion — ECRH deposition case p15bb.

Figure 6.17 displays the response $Y(x, f_0)$ obtained from the simulation, together with the model prediction $\propto \exp[\lambda(x - x_0)]$ constructed from the two estimates, $\lambda(\chi_{\mathrm{WLS}}, V_{\mathrm{WLS}})$ and $\lambda(\chi_{\text{2-pt}}, V_{\text{2-pt}})$. The mean relative error on the amplitude is $\approx 6.8\%$ for the two-point fit and $\approx 8.8\%$ for the WLS fit, while the mean absolute phase error is about $4°$ for both approaches.

In the WLS method, each spatial datapoint is weighted by the inverse of the variance estimated by the LPM at that location; points with large variance (for instance where only a few modulation periods are available) therefore contribute less to the fit. This can occasionally lead to a larger local discrepancy between the reconstructed and measured fundamental harmonic at those positions. Nevertheless, for the present case the two fitting strategies produce very similar reconstructed profiles.

The origin of the discrepancies between the model and the measured signal can be examined by looking at the local slopes A'/A and ϕ', computed from finite differences between neighbouring radial points within the fitting window, as shown in Fig. 6.18. For an exact complex exponential these quantities should be constant. In practice, the pointwise estimates exhibit a remarkable spread due to the noise that causes the system's response to deviate from the ideal complex–exponential form of the analytical solution.

In light of this, the WLS and two-point reconstructions should be interpreted as providing effective, spatially averaged values of A'/A and ϕ' over the window, rather than

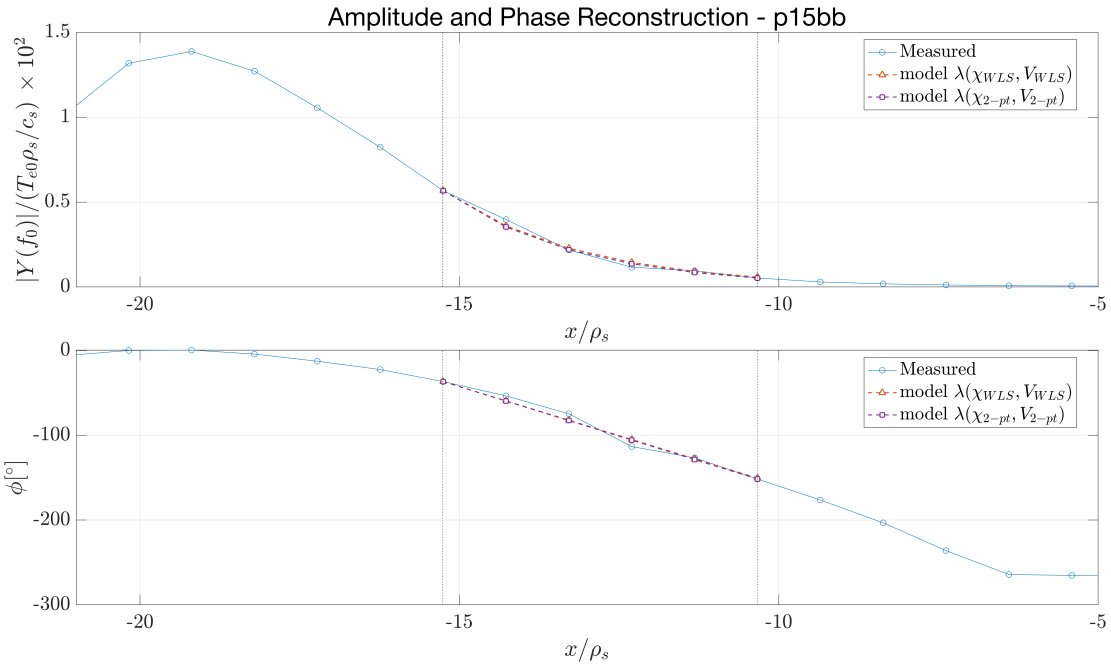

Figure 6.17: Temperature signal reconstruction in frequency space from estimated transport coefficients — ECRH deposition case p15bb .

pointwise-valid estimates of the corresponding gradients. Nevertheless, the reconstructions indicate that, for the reference case and within the selected spatial interval, the temperature response at the modulation frequency is reasonably well described by a single exponential characterized by the coefficients χ and V. This is, however, not sufficient to conclude that the model can accurately describe the transport physics of the system. An additional check is required: we must assess the dependence of these coefficients on the modulation frequency, as we do in the following section.

6.2.4 Frequency Scan of the Modulated ECRH Deposition

To better understand how the system responds to different ECRH modulation frequencies, and to assess whether the inferred transport coefficients depend on the drive frequency, a frequency scan is performed in which the deposition amplitude and width are kept fixed, thus isolating the effect of the drive timescale. The corresponding simulations are listed in Table 6.1. First, the amplitude and phase of the temperature response at the modulation frequency dependence on the modulation period T is examined. These quantities are shown in Figs. 6.19 and 6.20. Figure 6.19 displays the radial dependence of the amplitude of the fundamental (solid lines) together with the second and third harmonics (dashed and dotted lines, respectively) for all modulation periods.

We observe that the amplitude of the fundamental harmonic increases markedly with T: the high-frequency case (p3bb) shows the smallest response, while the lowest-frequency case (p45bb) exhibits the largest. Within the analysis window the higher harmonics remain

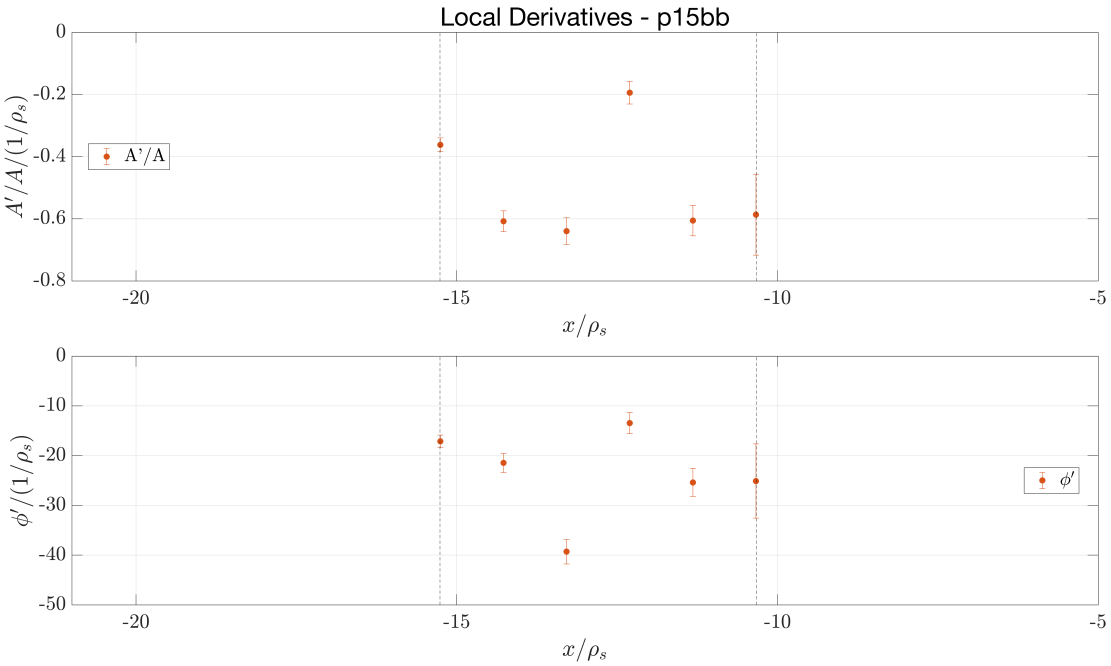

Figure 6.18: Local values of α and β computed with finite differences — ECRH deposition case p15bb .

at much lower amplitudes than the corresponding fundamental in all cases. Conversely, away from this region, their amplitudes become comparable to the fundamental, reflecting a lower signal-to-noise ratio.

Figure 6.20 shows the phase profiles: moving away from the source, the phase decreases on both sides, indicating an increasing lag of the temperature response with respect to the drive. At a fixed radial position, the phase lag is larger for the shorter periods (higher frequencies): the p3bb case exhibits the steepest phase variation, while p45bb shows the shallowest.

Figure 6.21 shows the total harmonic distortion (THD) of the temperature signal as a function of T, computed in the analysis window. The THD is largest for the shortest period ($\approx$ 21% at $T = 3$) and decreases monotonically to $\approx$ 8.5% at $T = 45$. This behaviour directly mirrors the relative importance of the higher harmonics in Fig. 6.19: at high frequency the fundamental is weak and nonlinearly generated harmonics have a significant relative amplitude, while at low frequency the fundamental dominates and the response is correspondingly more linear.

As shown in Figure 6.22, the extent to which the driven perturbation propagates radially is summarised by plotting, as a function of T, the ratio of the high-coherence-region half-width ($\|x_{b,R} - x_{\text{dep}}\|$, where $x_{b,R}$ is the high-coherence region right boundary w.r.t. the deposition point) to half the deposition width. This ratio increases from ≈ 1.4 at $T = 9$ to ≈ 3.3 at $T = 45$, confirming that at higher frequencies the coherent response is confined to a small region close to the source itself, whereas at low frequency the

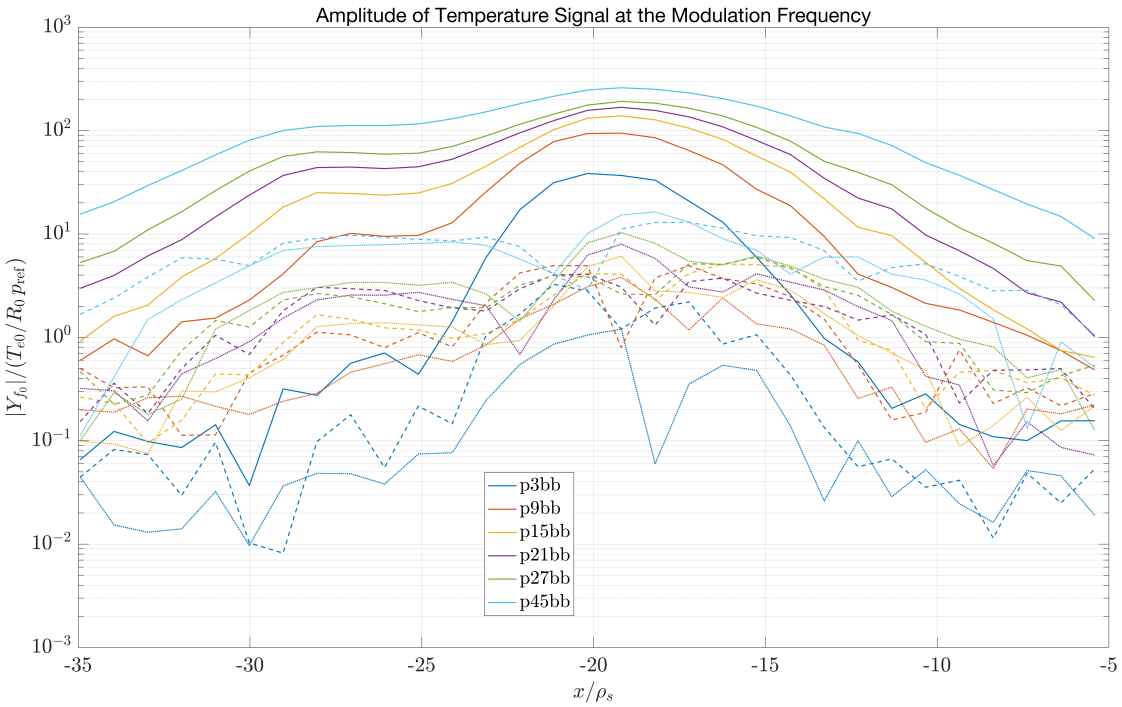

Figure 6.19: Radial dependence of the amplitude of the temperature signal at the modulation frequency (solid lines) and of the second ($2f_0$) and third ($3f_0$) harmonics (dashed and dotted lines, respectively) for all modulation periods p3bb–p45bb.

modulated heat wave extends over several times the deposition width, reflecting that the system's response is broader in space in this case.

Thus, while slow modulations produce a broader spreading of the signal, at higher frequencies it becomes strongly damped, and the response becomes more local and noisy, thereby setting an upper limit to the modulation frequency that can be effectively exploited in this type of analysis. In our simulations, this limit is reached in the p3bb case, where the high-coherence region becomes, for the first time, smaller than the deposition region, preventing any meaningful analysis outside the source. It is worth noting that this occurs as the modulation period ($T = 3$) becomes comparable to the temperature autocorrelation timescale of the TEM scenario discussed in Sec. 6.1, where we found $\tau_e/(R_0/c_s) = 1.4502$.

The analysis now proceeds with the estimation of the transport coefficients. Since the estimation of these coefficients appears to be strongly affected by the selected spatial region, comparing results obtained at different modulation frequencies requires adopting a consistent criterion for choosing this region. The safest approach is to fix a common spatial observation window for all estimates — one in which the MSC remains sufficiently high and where the behaviour of α and β is as close as possible to spatially constant. The best compromise identified is therefore to use the same analysis window employed for the

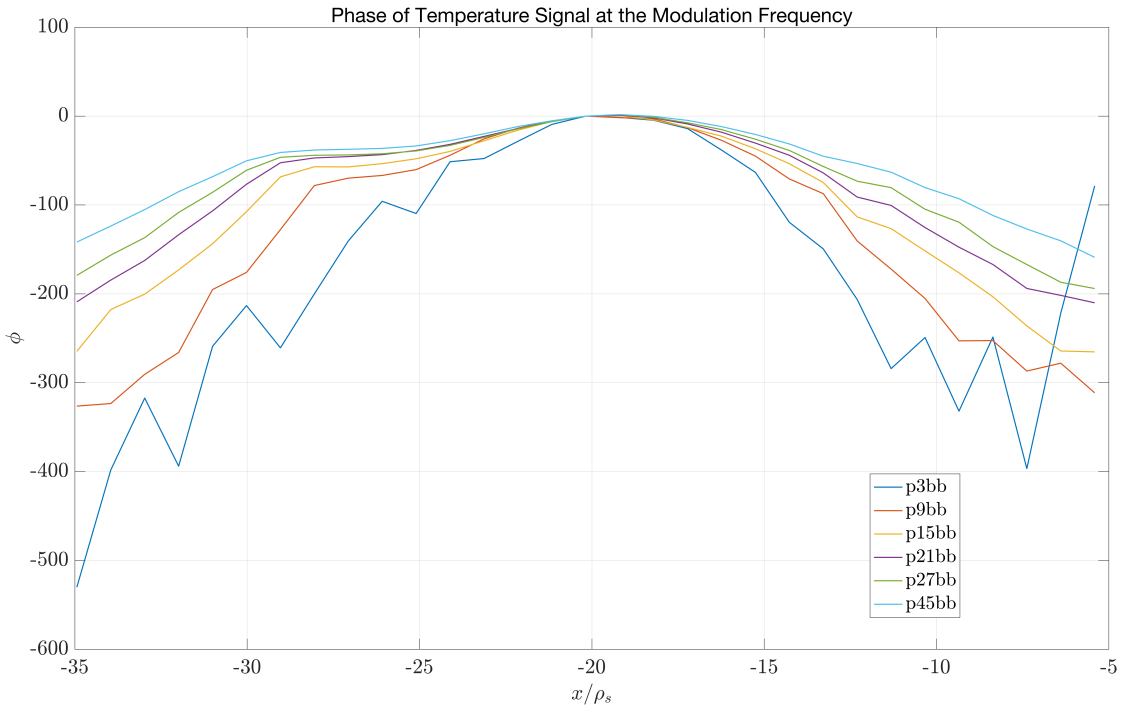

Figure 6.20: Radial profiles of the phase of the temperature signal for all modulation periods.

reference case p15bb, $x \in [-15.2559, -10.3346]$.[2]

The trends observed in amplitude and phase diagrams are reflected in the transport coefficients inferred from the FRF. Figures 6.23 and 6.24 show, respectively, the diffusion and advection coefficients as a function of T (i.e. $1/f_0$). For each run, two estimates are plotted: the two–point estimate ($\chi_{\text{2-pt}}$, $V_{\text{2-pt}}$) and the WLS estimate (χ_{WLS}, V_{WLS}), with error bars corresponding to the standard error of the WLS fit. The diffusion coefficient exhibits a clear pattern (Fig. 6.23): both $\chi_{\text{2-pt}}$ and χ_{WLS} increase monotonically as the modulation period is lengthened from $T = 9$ to $T = 45$. The two estimation methods are consistent within the quoted uncertainties; the WLS values are slightly higher and exhibit substantially large error bars.

The behaviour of the advection coefficient is somewhat different (see Fig. 6.24). At the highest frequency ($T = 9$), the inferred V is small. As T is increased, both $V_{\text{2-pt}}$ and V_{WLS} grow, reaching a maximum around $T = 21$, before decreasing again for the longest period $T = 45$. This suggests that the convective contribution is most pronounced at intermediate frequencies, while at very high and very low frequencies the response is

[2]There are two limiting cases in this scan: p3bb and p9bb. The former is problematic because the high-coherence region lies entirely within the source region, preventing any estimation of the transport coefficients. The latter is challenging because the analysis window is still too narrow, containing only a few grid points, so that the coefficients can only be estimated at the cost of large uncertainties.

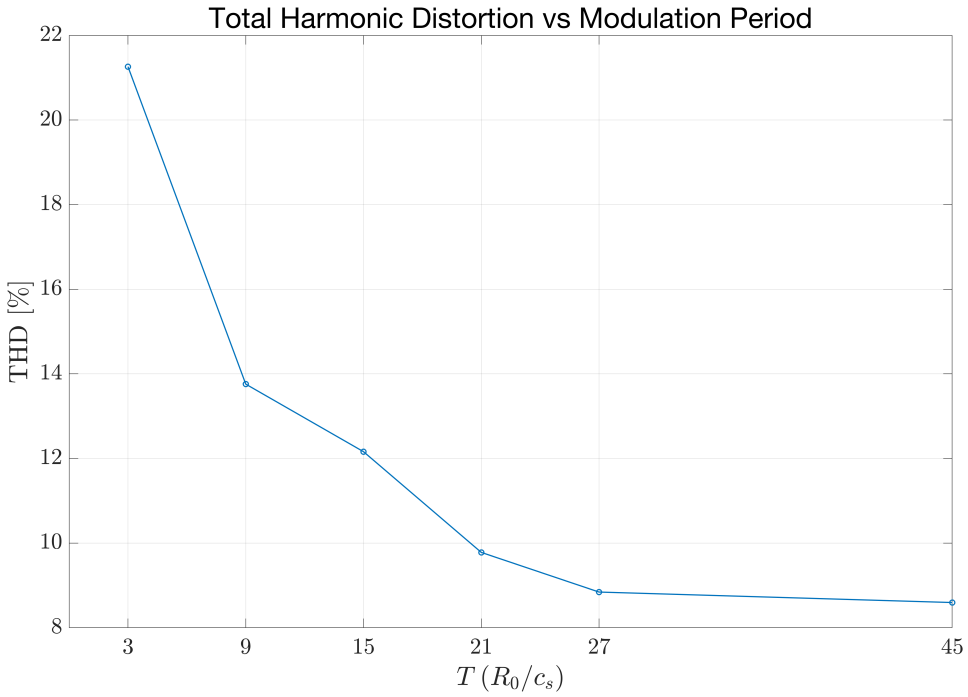

Figure 6.21: THD of the temperature signal as a function of the modulation period.

dominated by the diffusive part. The relatively large error bars caution against over-interpreting the precise shape of this curve, but the presence of a non-zero convective component is clearly indicated.

Finally, Figure 6.25 compares the mean amplitude reconstruction relative errors and the mean phase reconstruction absolute error of the WLS and two–point methods as a function of the modulation period T. The larger error observed for the two-point method at $T = 45$ instead indicates that, for this run, a longer simulation is likely required in order to reduce the uncertainty.

Taken together, these results show that the plasma response to a modulated ECRH drive is indeed frequency-dependent for deposition at frequencies approaching the inverse turbulent correlation time. At lower modulation frequencies, the response becomes more coherent and quasi–linear: the temperature signal propagates further from the source, and the inferred transport coefficients are closer to diffusive. Nevertheless, the systematic dependence of χ on T highlights the limitations of the transport model [53]. At higher frequencies, by contrast, the perturbation remains localized, the fundamental harmonic is weaker and the inferred coefficients are noisier and less clearly diffusive, revealing an intrinsic limitation of a simple advection–diffusion closure with constant transport coefficients on these timescales. Further work is needed to elucidate the plasma response at even larger modulation timescales.

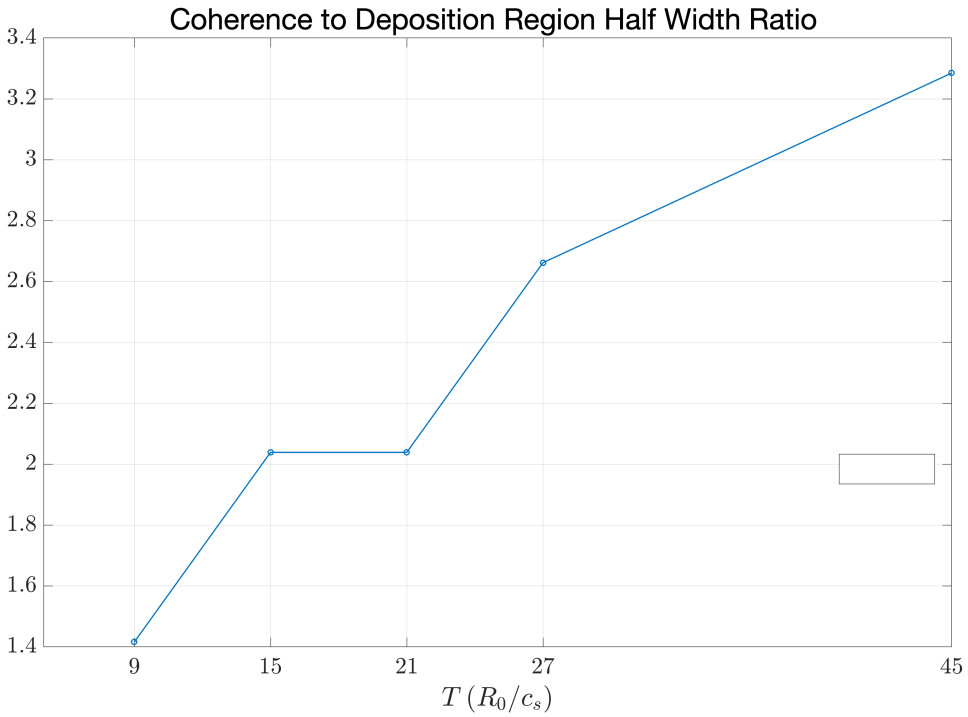

Figure 6.22: Ratio of the high-coherence region half width to half the deposition width as a function of the modulation period.

6.2.5 Impact of the Deposition Profile Width

Finally, the impact of the deposition region width is analysed by taking the reference case p15bb and reducing the deposition half-width to $W = 2.25$. The deposition interval thus becomes $x \in [-22.25, -17.75]$, while the total injected power remains constant. We refer to this case as p15bc. From the MSC analysis, we find that the high-coherence region is now restricted to $x \in [-26.0826, -13.2874]$. Computing the ratio between the half-width of the high-coherence region and the deposition half-width yields a value of ≈ 2.98, larger than in the reference case (≈ 2.05). This is already an important indication: if the high-coherence region changes, the inferred coefficients may be affected, because a different spatial analysis window will be required. The average THD is now $\approx 12.43\%$, and the coefficient estimates are:

$$\chi_{\mathrm{WLS}} = (3.53 \pm 0.63)\,\frac{c_{\mathrm{s}}\rho_{\mathrm{s}}^2}{R_0}, \qquad \chi_{\text{2-pt}} = 3.17\,\frac{c_{\mathrm{s}}\rho_{\mathrm{s}}^2}{R_0}, \tag{6.4}$$

$$V_{\mathrm{WLS}} = (0.68 \pm 0.28)\,\frac{c_{\mathrm{s}}\rho_{\mathrm{s}}}{R_0}, \qquad V_{\text{2-pt}} = 0.64\,\frac{c_{\mathrm{s}}\rho_{\mathrm{s}}}{R_0}. \tag{6.5}$$

These estimates differ significantly from the reference scenario. Moreover, if we use them to reconstruct the amplitude and phase profiles, we obtain the result shown in Fig. 6.26. It is evident that the fit quality has deteriorated: the average amplitude relative error is 8.1% for WLS and 8.5% for the two-point method, while the average absolute phase

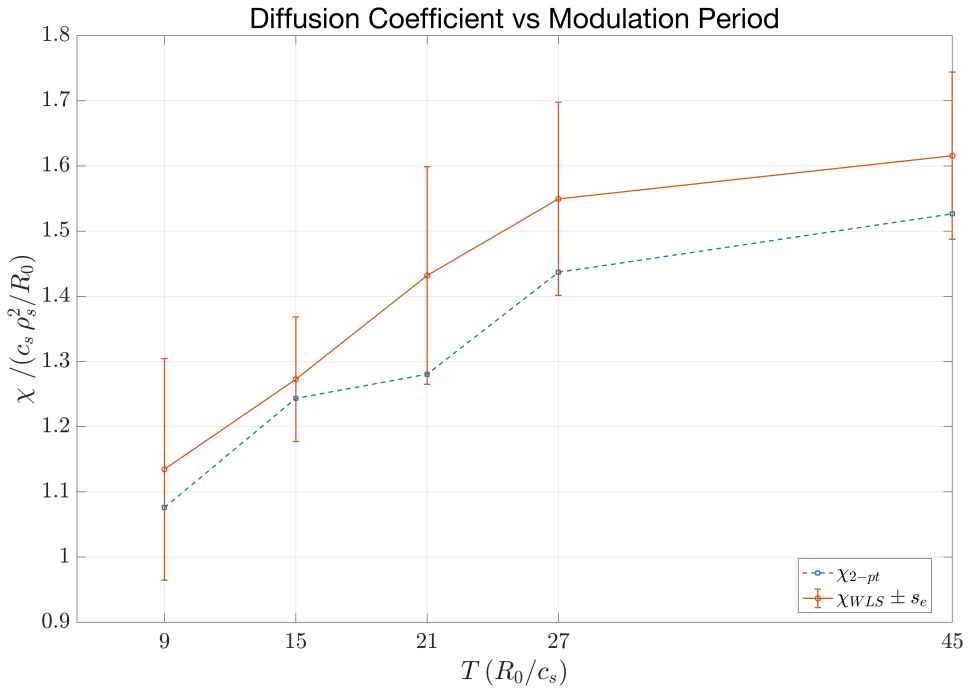

Figure 6.23: Dependence of diffusion coefficient on the modulation period.

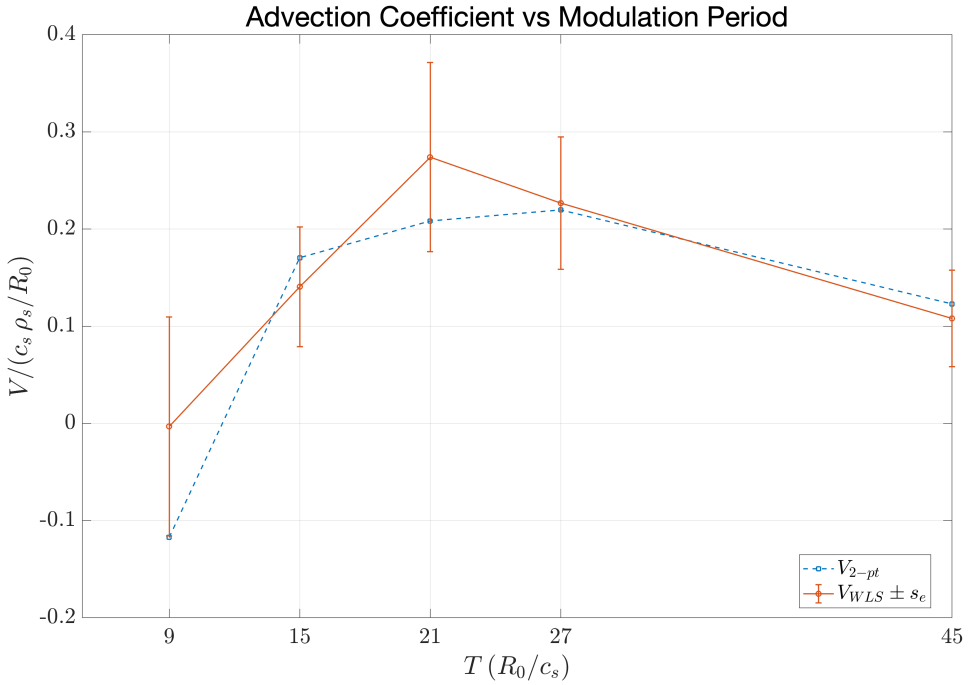

Figure 6.24: Dependence of advection coefficient on the modulation period.

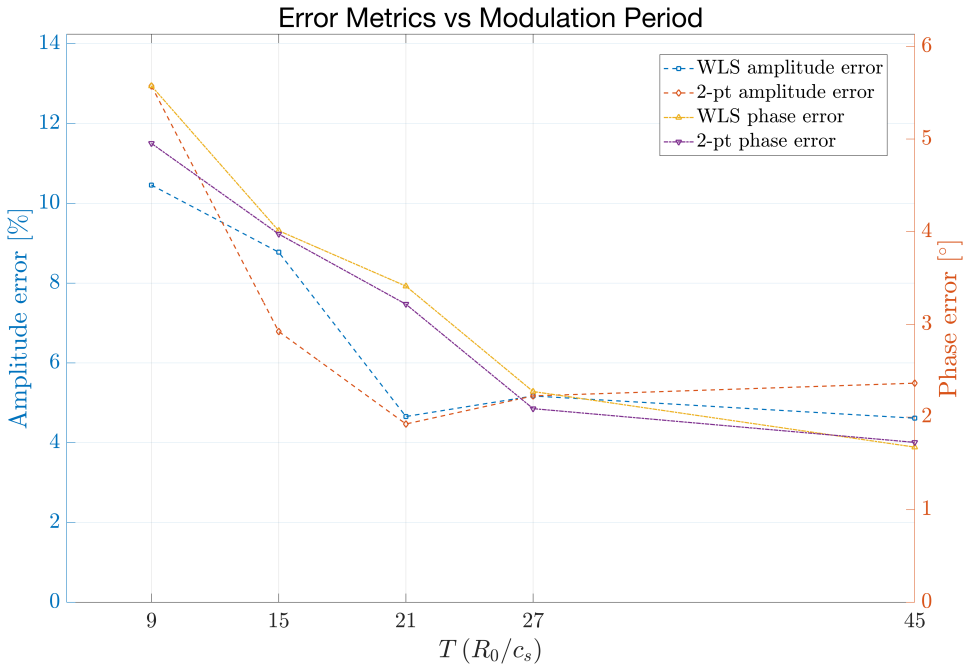

Figure 6.25: Amplitude and phase reconstruction errors of the WLS and two-point methods as a function of the modulation period T.

error is 3.8° for WLS and 4° for the two-point method.

Looking at the local slopes A'/A and ϕ' (Fig. 6.27), we now observe a clear systematic trend rather than purely scattered fluctuations, indicating a deterioration of the conditions under which the previous fitting procedure was made.

Overall, the system's response seems to be sensitive also on the deposition profile: a narrower and steeper profile reduces the high-coherence region width and degrades the estimation accuracy, as evidenced by the reconstruction plot. Consequently, the single complex exponential fitting does not seem to perform reliably for this deposition shape.

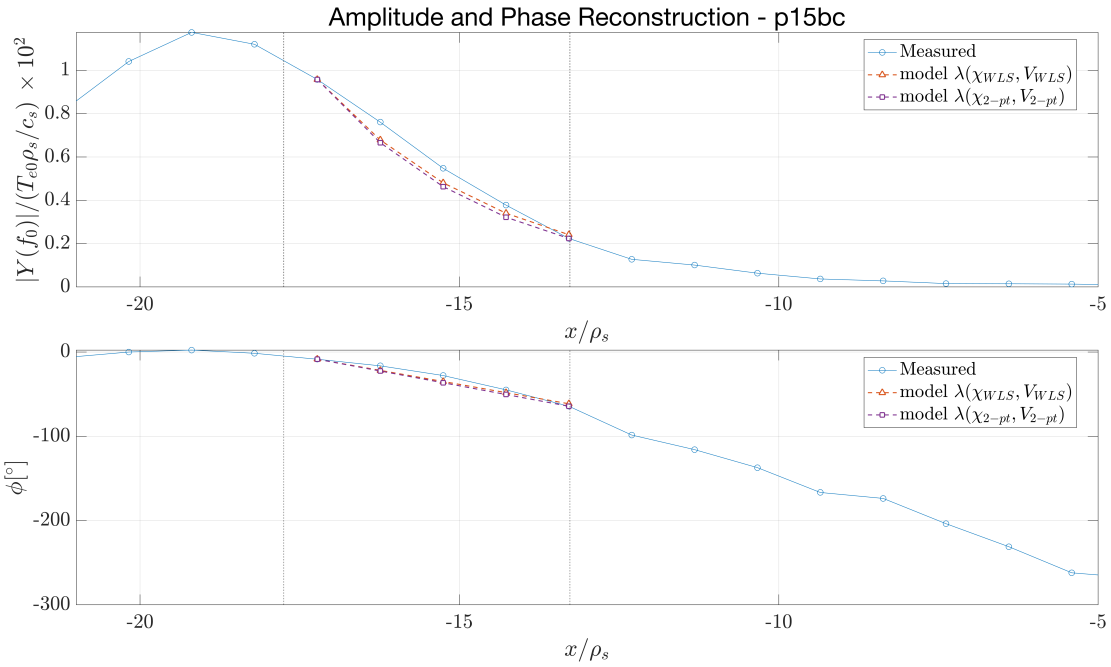

Figure 6.26: Reconstruction in frequency space of the temperature response from the estimated transport coefficients — ECRH deposition case p15bc.

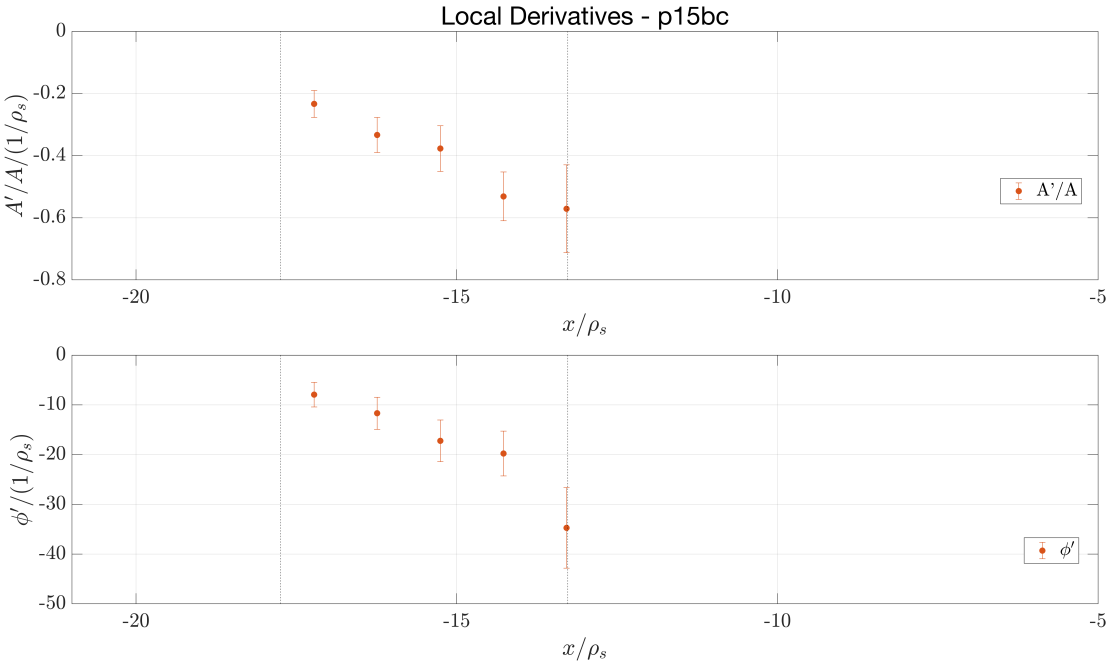

Figure 6.27: Local values of α and β computed with finite differences — ECRH deposition case p15bc.

Chapter 7

Conclusions

This work has investigated turbulent electron heat transport in a temperature–gradient trapped–electron–mode (∇T–TEM) regime, focusing on the response to a periodically modulated Electron Cyclotron Resonance Heating (ECRH) source. Nonlinear gyrokinetic simulations have been carried out with the GENE code in a local $\hat{s}$–α flux–tube geometry, employing a time–dependent EC power–deposition module. This setup defines a controlled scenario in which the plasma is driven by a prescribed heat source, and its response is examined directly in the frequency domain.

The overarching goal has been to establish a framework for developing and validating transport models through a perturbative approach supported by high-fidelity simulations. Within this framework, an advection–diffusion model with constant coefficients has been tested, thereby identifying conditions where this closure begins to break down.

Summary of main results

When the modulated ECRH source is applied close to a rational surface, the imposed heating locally steepens the temperature gradient around the deposition radius, while the turbulence–induced corrugations leave a small–scale imprint even inside the driven perturbation. The resulting temperature response is left–right asymmetric and carries the signature of the rational surface closest to the source in both the frequency response function (FRF) amplitude and phase. This illustrates an intrinsic limitation of simple advection-diffusion (AD) closures with spatially constant coefficients: on radial scales comparable to the spacing of rational surfaces, transport is strongly inhomogeneous, and constant transport coefficients cannot capture this effect.

A scan of the modulation period $T \in \{3, 9, 15, 21, 27, 45\}$, at fixed deposition amplitude and width, has been performed to assess how the response depends on the modulation frequency as it approaches the inverse turbulence correlation timescale ($1/\tau_c$). For the shortest periods, the high–coherence region shrinks to within the source, the temperature perturbation remains strongly localised, and the fundamental harmonic of the temperature signal at the drive frequency is relatively weak compared to the turbulence–induced background. In this regime, where the drive period approaches τ_c, the assumptions of a

linear AD closure are clearly strained.

As the modulation period is increased ($T \geq 15$), the fundamental harmonic becomes dominant, the high–coherence region broadens, and the temperature signal propagates further away from the deposition radius. In this frequency range, the FRF in a suitably chosen analysis window appears to be reasonably well fitted by the AD model with a single complex eigenmode. However, the estimated diffusion and advection coefficients vary with the modulation period T when evaluated in a common spatial window, showing that constant time-independent χ and V cannot provide a simple or universal description of the turbulent transport, as different drive timescales lead to different estimations. Finally, varying the perpendicular width of the deposition profile—while keeping the total deposited power fixed—modifies the extent of the high-coherence region, with the consequence that the inferred coefficients result sensitive to the spatial extent of the source.

Outlook

The present study opens several promising avenues for future research, both on the physics side and in terms of methodological development.

A natural next step is to extend the analysis to account for different values of the resonant parallel velocity $v_{\parallel,\mathrm{res}}$, in order to determine if, and to what extent, it influences the system dynamics and the propagation of the temperature signal.

Further exploration of parameter scans is also warranted. In particular, varying the modulation amplitude would make it possible to assess how the ratio between the fundamental and higher harmonics in the temperature response depends on the injected power. Such analyses could help determine to what extent the higher-harmonic content reflects genuinely nonlinear transport.

The investigation of AD models can be pushed further by refining the analysis to account for spatially dependent coefficients [54] and by including the source region within the analysis window, exploiting the fact that the spatio–temporal structure of the heat source is known exactly.

In addition to single–frequency modulation, another interesting possibility is to implement a multi–frequency modulation scheme. Driving the system simultaneously at several distinct frequencies would enable the development and validation of more sophisticated transport models[53].

Finally, the present analysis has been restricted to a local flux–tube geometry. Extending the same perturbative framework to global gyrokinetic simulations would make it possible to investigate how large–scale effects influence the propagation of temperature perturbations driven by modulated heat pulses.

Bibliography

[1] Intergovernmental Panel on Climate Change (IPCC). Summary for policymakers. in: *Climate Change 2023: Synthesis Report. Contribution of Working Groups I, II and III to the Sixth Assessment Report of the Intergovernmental Panel on Climate Change*, 2023. URL https://www.ipcc.ch/report/ar6/syr/downloads/report/IPCC_AR6_SYR_SPM.pdf.

[2] J. Davidson, A.˙ The role of nuclear energy in the global energy transition. Technical Report ET14, Oxford Institute for Energy Studies, August 2022. URL https://www.oxfordenergy.org/wpcms/wp-content/uploads/2022/08/The-Role-of-Nuclear-Energy-in-the-Global-Energy-Transition-ET14.pdf. OIES Paper.

[3] P.J. Heitzenroeder, A.W. Brooks, J.H. Chrzanowski, F. Dahlgren, R. Hawryluk, G.D. Loesser, C. Neumeyer, C. Mansfield, Jean-Jacques Cordier, David Campbell, G.A. Johnson, A. Martin, P.H. Rebut, J.O. Tao, J.P. Smith, Michael Schaffer, D.A. Humphreys, P.J. Fogarty, B. Nelson, and R.P. Reed. An overview of the iter in-vessel coil systems. pages 1 – 4, 07 2009. doi: 10.1109/FUSION.2009.5226519.

[4] J. P. Freidberg. *Plasma Physics and Fusion Energy*. Cambridge University Press, February 2007. doi: 10.1017/CBO9780511755705. URL https://doi.org/10.1017/CBO9780511755705.

[5] J. D. Lawson. Some criteria for a power producing thermonuclear reactor. *Proceedings of the Physical Society. Section B*, 70(1):6–10, January 1957. doi: 10.1088/0370-1301/70/1/303. URL https://doi.org/10.1088/0370-1301/70/1/303.

[6] International Atomic Energy Agency. Fusion energy: Overview and prospects. https://www.iaea.org/sites/default/files/2025-09/fusionenergy_0.pdf.

[7] A. J. Brizard and T. S. Hahm. Foundations of nonlinear gyrokinetic theory. *Rev. Mod. Phys.*, 79:421–468, Apr 2007. doi: 10.1103/RevModPhys.79.421. URL https://link.aps.org/doi/10.1103/RevModPhys.79.421.

[8] Josef Proll. *Trapped-Particle Instabilities in Quasi-Isodynamic Stellarators*. PhD thesis, Max Planck Institute for Plasma Physics / Technische Universität München, 2014. URL https://pure.mpg.de/pubman/faces/ViewItemOverviewPage.jsp?itemId=item_2034974.

[9] T. Dannert and F. Jenko. Gyrokinetic simulation of collisionless trapped-electron mode turbulence. *Physics of Plasmas*, 12(7):072309, 2005. doi: 10.1063/1.1949607.

[10] Robert J. Goldston and Paul H. Rutherford. *Introduction to Plasma Physics*. Institute of Physics Publishing, Bristol and Philadelphia, 1995. ISBN 978-0750301831.

[11] Leon Ottink. The impact of currents on microinstabilities in fusion plasmas. Master's thesis, Eindhoven University of Technology, 2025. URL https://research.tue.nl/nl/studentTheses/the-impact-of-currents-on-microinstabilities-in-fusion-plasmas/.

[12] L. Morren, Maikel C.˙ The influence of collisions on trapped-electron modes in fusion plasmas. Master's thesis, Eindhoven University of Technology, June 2022. URL https://research.tue.nl/en/studentTheses/the-influence-of-collisions-on-trapped-electron-modes-in-fusion-p/. Master's thesis.

[13] M. J. Pueschel and Sven Wiesen. Master class on turbulence and transport in fusion plasmas. Lecture slides, course 3MF507, 2025.

[14] A. G. Peeters and D. Strintzi. The fokker-planck equation, and its application in plasma physics. *Annalen der Physik*, Vol.17(No.2-3):142–157, February 2008. ISSN 0003-3804. doi: 10.1002/andp.200710279. URL http://dx.doi.org/10.1002/andp.200710279.

[15] Robert G. Littlejohn. Hamiltonian perturbation theory in noncanonical coordinates. *Journal of Mathematical Physics*, 23(5):742–747, 05 1982. ISSN 0022-2488. doi: 10.1063/1.525429. URL https://doi.org/10.1063/1.525429.

[16] Robert G. Littlejohn. A guiding center hamiltonian: A new approach. *Journal of Mathematical Physics*, 20(12):2445–2458, 12 1979. ISSN 0022-2488. doi: 10.1063/1.524053. URL https://doi.org/10.1063/1.524053.

[17] E. A. Frieman and Liu Chen. Nonlinear gyrokinetic equations for low-frequency electromagnetic waves in general plasma equilibria. *The Physics of Fluids*, 25(3):502–508, 03 1982. ISSN 0031-9171. doi: 10.1063/1.863762. URL https://doi.org/10.1063/1.863762.

[18] Daniel H. E. Dubin, John A. Krommes, C. Oberman, and W. W. Lee. Nonlinear gyrokinetic equations. *The Physics of Fluids*, 26(12):3524–3535, 12 1983. ISSN 0031-9171. doi: 10.1063/1.864113. URL https://doi.org/10.1063/1.864113.

[19] Michail M. Skyllas. On the impact of electron cyclotron current drive on plasma turbulence. Master's thesis, Eindhoven University of Technology (TU/e), Eindhoven, The Netherlands, November 2023. URL https://pure.tue.nl/ws/portalfiles/portal/316911664/1747452_-_Skyllas_M.M._-_MSc_thesis_Thesis_-_NF.pdf. M.Sc. thesis; work carried out at DIFFER.

[20] H. J. de Blank. Guiding center motion. *Fusion Science and Technology*, 2012. doi: 10.13182/FST12-A13493. URL https://www.ans.org/pubs/journals/fst/article-13493/.

[21] Florian Merz. *Gyrokinetic Simulation of Multimode Plasma Turbulence*. PhD thesis, University of Münster, Münster, Germany, 2008. URL https://genecode.org/PAPERS_1/merz.pdf. Ph.D. thesis.

[22] M. A. Beer. *Gyrofluid Models of Turbulent Transport in Tokamaks*. PhD thesis, Princeton University, 1995.

[23] X. Lapillonne, S. Brunner, T. Dannert, S. Jolliet, A. Marinoni, L. Villard, T. Görler, F. Jenko, and F. Merz. Clarifications to the limitations of the $\hat{s} - \alpha$ equilibrium model for gyrokinetic computations of turbulence. *Physics of Plasmas*, 2009. doi: 10.1063/1.3096710. URL https://doi.org/10.1063/1.3096710.

[24] R. J. La Haye, S. Günter, D. A. Humphreys, J. Lohr, T. C. Luce, M. E. Maraschek, C. C. Petty, R. Prater, J. T. Scoville, and E. J. Strait. Control of neoclassical tearing modes in diii–d. *Physics of Plasmas*, 9(5):2051–2060, 05 2002. ISSN 1070-664X. doi: 10.1063/1.1456066. URL https://doi.org/10.1063/1.1456066.

[25] H. Zohm, G. Gantenbein, F. Leuterer, A. Manini, M. Maraschek, Q. Yu, and the ASDEX Upgrade Team. Control of mhd instabilities by eccd: Asdex upgrade results and implications for iter. *Nuclear Fusion*, 47(3):228, mar 2007. doi: 10.1088/0029-5515/47/3/010. URL https://doi.org/10.1088/0029-5515/47/3/010.

[26] Peter L. van de Giessen. Analysis of the electron cyclotron heating and current drive system in the st-f1 spherical tokamak. Master's thesis, Eindhoven University of Technology (TU/e), Eindhoven, The Netherlands, March 2021. URL https://research.tue.nl/en/studentTheses/analysis-of-the-electron-cyclotron-heating-and-current-drive-syst. M.Sc. thesis.

[27] Thomas H. Stix. *Waves in Plasmas*. Springer Science & Business Media / American Institute of Physics, New York, 1992.

[28] Donald Gary Swanson. *Plasma Waves*. Series in Plasma Physics. CRC Press, 2003. ISBN 9780750309271.

[29] Donald Gary Swanson. *Plasma Kinetic Theory*. Series in Plasma Physics. CRC Press, 2008. ISBN 9781420075809.

[30] Egbert Westerhof. Electron cyclotron waves. *Fusion Science and Technology*, 61(2T): 304–311, 2012. doi: 10.13182/FST12-A13517. URL https://doi.org/10.13182/FST12-A13517.

[31] R. Prater. Heating and current drive by electron cyclotron waves. *Physics of Plasmas*, 11(5):2349–2376, 05 2004. ISSN 1070-664X. doi: 10.1063/1.1690762. URL https://doi.org/10.1063/1.1690762.

[32] C. F. Kennel and F. Engelmann. Velocity space diffusion from weak plasma turbulence in a magnetic field. *The Physics of Fluids*, 9(12):2377–2388, 12 1966. ISSN 0031-9171. doi: 10.1063/1.1761629. URL https://doi.org/10.1063/1.1761629.

[33] N. J. Fisch and A. H. Boozer. Creating an asymmetric plasma resistivity with waves. *Phys. Rev. Lett.*, 45:720–722, Sep 1980. doi: 10.1103/PhysRevLett.45.720. URL https://link.aps.org/doi/10.1103/PhysRevLett.45.720.

[34] T. Ohkawa. Steady-state operation of tokamaks by r-f heating. Technical Report GA-A13847, General Atomics, 1976. URL https://library.psfc.mit.edu/catalog/online_pubs/tech_reports/GA-A13847.pdf.

[35] Tobias Görler. *Multiscale Effects in Plasma Microturbulence*. PhD thesis, Max Planck Institute for Plasma Physics / University of Ulm, Garching, Germany, 2013. URL https://genecode.org/PAPERS_1/goerler.pdf. Ph.D. thesis.

[36] Jose E. Roman, Matthias Kammerer, Florian Merz, and Frank Jenko. Fast eigenvalue calculations in a massively parallel plasma turbulence code. *Parallel Computing*, 36(5):339–358, 2010. ISSN 0167-8191. doi: https://doi.org/10.1016/j.parco.2009.12.001. URL https://www.sciencedirect.com/science/article/pii/S0167819109001239. Parallel Matrix Algorithms and Applications.

[37] Kevin C. F. Koolen. Plasma microturbulence suppression based on electron cyclotron resonant heating. Master's thesis, Eindhoven University of Technology (TU/e), Eindhoven, The Netherlands, 2025. URL https://research.tue.nl/files/358669023/1229904_-_Koolen_K.C.F._-_MSc_thesis_Thesis_-_NF.pdf. M.Sc. thesis.

[38] E. Westerhof and J. Pratt. Closure of the single fluid magnetohydrodynamic equations in presence of electron cyclotron current drive. *Physics of Plasmas*, 21(10):102516, 10 2014. ISSN 1070-664X. doi: 10.1063/1.4900871. URL https://doi.org/10.1063/1.4900871.

[39] Charles F.F. Karney. Fokker-planck and quasilinear codes. *Computer Physics Reports*, 4(3):183–244, 1986. ISSN 0167-7977. doi: https://doi.org/10.1016/0167-7977(86)90029-8. URL https://www.sciencedirect.com/science/article/pii/0167797786900298.

[40] A. Zee. *Quantum field theory in a nutshell*. Princeton University Press, second edition edition, 2010.

[41] Alan V. Oppenheim, Alan S. Willsky, and S. Hamid Nawab. *Signals & systems (2nd ed.)*. Prentice-Hall, Inc., USA, 1996. ISBN 0138147574.

[42] GENE Development Team. *The Gyrokinetic Plasma Turbulence Code GENE: User Manual*. Max Planck Institute for Plasma Physics (IPP), Garching, Germany, August 2024. Available at https://genecode.org/.

[43] Rik Pintelon and Johan Schoukens. *System Identification: A Frequency Domain Approach*. Wiley–IEEE Press, Hoboken, NJ, USA, 2nd edition, 2012. ISBN 978-1-118-01867-0. doi: 10.1002/9781118287466. URL https://books.google.com/books?id=3lGJWtjGDzsC.

[44] M van Berkel, R J R van Kampen, G Vandersteen, T Kobayashi, T Ravensbergen, H Igami, J T Lammers, G W Oosterwegel, C Galperti, F Felici, M R de Baar, the LHD Experiment Group, and the TCV Team. Correcting for non-periodic behaviour in perturbative experiments: application to heat pulse propagation and modulated gas-puff experiments. *Plasma Physics and Controlled Fusion*, 62(9):094001, jul 2020. doi: 10.1088/1361-6587/ab9eaa. URL https://doi.org/10.1088/1361-6587/ab9eaa.

[45] Julius S. Bendat and Allan G. Piersol. *Random Data: Analysis and Measurement Procedures*. Wiley Series in Probability and Statistics. Wiley, 4 edition, 2010. ISBN 978-0-470-24877-5. doi: 10.1002/9781118032428.

[46] Matthijs van Berkel. *Estimation of Heat Transport Coefficients in Fusion Plasmas*. Eindhoven, The Netherlands, 2015. ISBN 978-90-386-3868-3. URL https://research.tue.nl/files/3837576/794807.pdf.

[47] N. J. L. Cardozo. Perturbative transport studies in fusion plasmas. *Plasma Physics and Controlled Fusion*, 37(8):799–852, Aug 1995. doi: 10.1088/0741-3335/37/8/001.

[48] Andrei D. Polyanin and Valentin F. Zaitsev. *Handbook of Exact Solutions for Ordinary Differential Equations*. Chapman & Hall/CRC, London, 2003. ISBN 9781584882978.

[49] Tilo Strutz. *Data Fitting and Uncertainty (A practical introduction to weighted least squares and beyond)*. ISBN 3834810223.

[50] Harry Smith Norman R. Draper. *Applied Regression Analysis*. John Wiley & Sons, 1998. ISBN 9781118625590. doi: https://doi.org/10.1002/9781118625590. URL https://onlinelibrary.wiley.com/doi/abs/10.1002/9781118625590.

[51] F. Merz and F. Jenko. Nonlinear interplay of tem and itg turbulence and its effect on transport. *Nuclear Fusion*, 50(5):054005, apr 2010. doi: 10.1088/0029-5515/50/5/054005. URL https://doi.org/10.1088/0029-5515/50/5/054005.

[52] D. R. Ernst, P. T. Bonoli, P. J. Catto, W. Dorland, C. L. Fiore, R. S. Granetz, M. Greenwald, A. E. Hubbard, M. Porkolab, M. H. Redi, J. E. Rice, K. Zhurovich, and Alcator C-Mod Group. Role of trapped electron mode turbulence in internal transport barrier control in the alcator c-mod tokamak. *Physics of Plasmas*, 11 (5):2637–2648, 05 2004. ISSN 1070-664X. doi: 10.1063/1.1705653. URL https://doi.org/10.1063/1.1705653.

[53] M. van Berkel, T. Kobayashi, G. Vandersteen, H.J. Zwart, H. Igami, S. Kubo, N. Tamura, H. Tsuchiya, M.R. de Baar, and The LHD Experiment Group. Heat flux reconstruction and effective diffusion estimation from perturbative experiments using advanced filtering and confidence analysis. *Nuclear Fusion*, 58(9):

096036, jul 2018. doi: 10.1088/1741-4326/aad13e. URL https://doi.org/10.1088/1741-4326/aad13e.

[54] Ricky van Kampen. *Frequency domain estimation of spatially varying transport coefficients*. Technische Universiteit Eindhoven, apr 2023. ISBN 978-90-386-5703-5. doi: 10.6100/3d7m-na18. URL https://pure.tue.nl/ws/portalfiles/portal/287833135/20230403_Kampen_van_hf.pdf. Proefschrift.